UNIVERSITY OF
LIVERPOOL

Retinal Image Processing for Blood Vessel Segmentation

Thesis submitted in accordance with the requirements of the University of Liverpool for the degree of Doctor of Philosophy

Nancy M. Salem

November 2007

To my beloved grandmother

Declaration

The work in this thesis is based on research carried out at the University of Liverpool. No part of this thesis has been submitted elsewhere for any other degree or qualification and it is all my own work unless referenced to the contrary in the text.

Nancy Salem

Liverpool, United Kingdom.

Abstract

Retinal Image Processing for Blood Vessel Segmentation

by Nancy Salem

The main objective of the work described in this thesis is to segment retinal blood vessels from digital colour fundus images with the ultimate purpose of early detection and diagnosis of many eye diseases. Ocular fundus images, which are acquired by taking photographs of the back of the eye using a fundus camera, are used in this study. In this context, to overcome the non-uniform illumination in retinal images, a pre-processing step is proposed to generate a binary mask and to enhance the retinal image in addition to the proposed segmentation methods.

As a first step, to segment the retinal field of view, differences between standard deviation values of successive regions followed by region growing are used to generate a binary mask. Histogram matching is proposed to enhance the visual appearance of retinal images by utilising the intensity information from red and green channels in order to combine advantages of both channels. The histogram of the red channel is used to modify the histogram of the green channel of the same retinal image. The performance of segmentation methods will be improved as a result of reducing the contrast between abnormalities and the retinal background.

Then, three different methods - supervised, unsupervised, and semi-supervised - for blood vessel segmentation are investigated. These methods are based on classifying/clustering

image pixels into vessels and non-vessels using a feature vector. In the beginning, a feature vector is extracted based on scale-space analysis. Then, the K-nearest neighbour classifier and two novel clustering algorithms, namely, nearest neighbour and radius-based clustering algorithms are applied to segment the retinal blood vessels.

Finally, the segmentation process is achieved using a single parameter unsupervised method based on analysis of the Hessian matrix. A novel vesselness measure that combines information from blood vessels' centrelines and orientations at multiple scales is proposed. Vessel centrelines are extracted from the large eigenvalue of the Hessian matrix, while orientation represented by the direction of the eigenvector corresponding to the small eigenvalue. The only parameter that needs to be set is a scale value which can be chosen reflecting the diameters of blood vessels within the image.

Acknowledgments

During my student life, I have met excellent people who have helped me academically and personally, I wish I could mention all of them by name. First I would like to thank my supervisor, Prof. Asoke K. Nandi for his motivation and guidance through the development of this project. I want to thank present and past members of the SPC group with special thanks to Dr Lindsay Jack for system administrator and helping me at the early stages in my research and to Dr Sonu Punnoose for his work in system administration. Thanks should also go to Liang, Alfonso, Sameh, Luciano, Jenny and Tingting and to the new members - with all my best wishes - Nazmat, Mohamed, Yupan, Sergio, and Obilor.

I am very grateful to the Egyptian Ministry of Higher Education for the financial support for this research. I would like to thank Dr Damian Farnell for the many meetings and discussions about retinal images. Also I would like to thank A. Hoover and Image Science Institute for making the retinal images publicly available (STARE and DRIVE datasets).

For the non-scientific side of my thesis, I owe special thanks to my husband Sameh for his love, patience, and encouragement during the years of my studies. On the other hand, my apologies should go to my children Ahmed and Mohamed for being away for long, I hope they understand one day what I was doing and this was meant to be for them.

Away from the work, I would like to acknowledge the encouragement I have been given by my parents-in-law. I would like to thank my parents, my brother Tamer, and my sisters Sally and Fatty for their hard work of taking care of my little boys during the first 3 years of this research. I owe my parents special gratitude for their unconditional support during my student life. I am sure that my PhD degree will make them proud of me. I want to

dedicate my thesis to my parents, my husband, and my children, but there is a very special grandmother who passed away during my writing up and I would like to dedicate this thesis to her.

Nancy Salem

Liverpool, November 2007.

Contents

List of Figures

List of Tables

Acronyms

AMD	Age-related Macular Degeneration
Az	Area under receiver operating characteristic curve
CT	Computed Tomography
DSA	Digital Subtraction Angiography
FCM	Fuzzy C Means
FN	False Negatives
FOV	Field Of View
FP	False Positives
FPR	False Positive Rates
GGT	Generated Ground Truth
GT	Ground Truth
HMI	Histogram Matched Image
HSI	Hue-Saturation-Intensity
KNN	K-Nearest Neighbour
MFR	Matched Filter Response
MRA	Magnetic Resonance Angiography

NN	Neural Networks
NNCA	Nearest Neighbour Clustering Algorithm
PDF	Probability Density Function
RACAL	RAdius-based Clustering ALgorithm
RGB	Red-Green-Blue
ROC	Receiver Operating Characteristic
SE	Structuring Element
TN	True Negatives
TP	True Positives
TPR	True Positive Rates

Chapter 1

Introduction

1.1 Motivation and Objectives

OUR EYES represent a unique window through which we can see the world around us. Similarly, they are the windows through which many diseases can be detected and diagnosed noninvasively. Eye examination is important in many different fields of medicine. In ophthalmology, it is the first step in detection and diagnosis of local ocular diseases. While in internal medicine, it provides evidence concerning the effect of many systemic diseases, which are associated with ocular manifestations. For example in cardiology, it can provide information about risk of cardiovascular diseases. Many diseases such as hypertension, diabetes, arteriosclerosis, cardiovascular disease, and stroke, may be revealed by the examination of the retinal vasculature [1].

At the early stages of many ocular diseases, the vision is not affected. Consequently, patients do not have their eyes examined which results in the development of diseases with more signs that affect the eyesight. At this stage, when the disease is progressed, the treatment might not be effective. Eye screening programs aim to detect signs of ocular diseases by regular examination of patients. Then, patients with ocular manifestation are referred to a consultant for further treatment. In these programs, many images are taken for the same person at different times. To compare these images, all the images need to be aligned in order to follow the development of existing diseases or detect new signs. This

can be achieved by segmentation of retinal blood vessels to act as landmarks to be used in image registration. For large numbers of images obtained, manual segmentation is a time consuming process and subject to human error. Therefore, it is important to develop reliable, automatic, and computationally effective methods for segmentation.

Automatic processing of retinal images is a challenging research area that aims to provide automated methods to help in the early detection and diagnosis of many eye diseases such as diabetic retinopathy (DR), age-related macular degeneration (AMD), and hypertension. In this area, retinal image pre-processing, segmentation, registration, and analysis are different forms of contribution from digital image processing techniques.

Automated segmentation of retinal blood vessels is an important step in screening programs for DR [2], evaluation of the retinopathy of prematurity [3], registration of retinal images for treatment evaluation [4, 5], generating retinal map for the diagnosis and treatment of AMD [6], or locating other anatomical structures such as the optic disc [7, 8] or the fovea [9].

In this research, the main interest is in the automatic segmentation of blood vessels from colour retinal images. The colour fundus image is the preferred type of image because it is widely used in clinics and suitable for screening programs. Figure 1.1 shows an example of a colour fundus retinal image of a normal human eye. A medical background about different imaging techniques and objects of interest in retinal images will be presented in the next chapter.

1.2 Contributions

The following is a summary of the original contributions of this research in the field of retinal image processing:

- A novel contribution of the red channel in pre-processing of colour fundus images. The red channel is used to generate a binary mask in order to avoid processing the dark region around the retinal field of view. Moreover, the intensity information from the red channel histogram is used to modify the histogram of the green channel

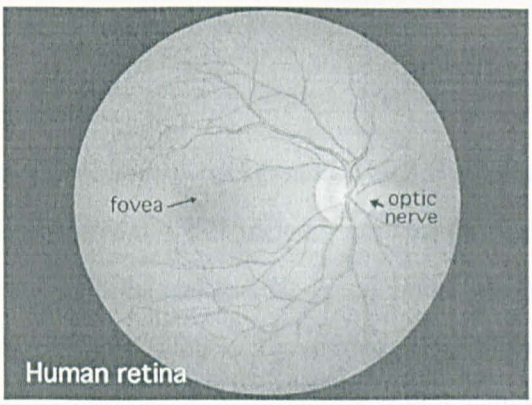

Figure 1.1: Ocular fundus image [taken from http://www.phys.ufl.edu/~avery/course/3400/vision/retina_picture_live.jpg].

image - of the same retinal image - to enhance the visual appearance and to correct the non-uniform illumination of retinal images.

- Proposing a new feature vector, which consists of three features, to segment retinal images in conjunction with supervised and semi-supervised methods. As a result of the small size of this feature vector, the processing time is significantly decreased.
- Modifying an existing semi-supervised radius-based clustering algorithm (*RACAL*) to act as a classifier. In this context, training and testing phases are proposed. The training phase follows the same concept as the original *RACAL* with an additional feature extraction step to extract features for the resultant clusters. The training phase starts by applying *RACAL* to cluster image pixels into different clusters based on a feature vector and a user defined parameter. Then, a feature extraction step is proposed to calculate features for each cluster. In the testing phase, unseen image pixels can be classified to the class of the nearest cluster from the training.
- Using the direction of vessels in retinal blood vessel segmentation, where a new vesselness measure is proposed. This measure is based on vessels' centrelines and the orientation at multiple scales. Vessel centrelines are detected from the large eigenvalue of the Hessian matrix, while the orientation is estimated from the eigenvectors that correspond to the small eigenvalues.

1.3 Outline of the Thesis

This thesis is organised as follows:

Chapter 2 presents the necessary background which is divided into two parts. The first part is the medical background, which includes introduction to the anatomy of the eye, the main retinal image components and feasible contributions of digital image processing in automated processing of retinal images. The second part is a review of supervised and unsupervised segmentation methods in the literature, additionally an introduction about receiver operating curves to evaluate the performance of segmentation methods is given.

Chapter 3 proposes two pre-processing steps applied to retinal images that utilise intensity information from the red channel image. A binary mask is generated using the standard deviation of successive rows and columns in conjunction with a region growing step. Then the retinal image is enhanced by using histogram matching to modify the histogram of the green channel image using the histogram of the red channel image. As a result, the contrast between bright abnormalities and retinal background is reduced and therefore, the performance of blood vessel segmentation is improved.

Chapter 4 investigates segmentation of retinal blood vessels using supervised, unsupervised, and semi-supervised methods. A feature vector of three features is proposed to be used in conjunction with the K-nearest neighbour (*KNN*) classifier, the nearest neighbour clustering algorithm (*NNCA*), and the radius-based clustering algorithm (*RACAL*) with a semi-supervised strategy to classify image pixels into vessel and non-vessel pixels. The use of the proposed feature vector results in a significant reduction in the processing time. Additionally, instead of the use of *RACAL* as a semi-supervised method, a modification is proposed in order to use *RACAL* as a classifier. This is achieved through training and testing phases.

Chapter 5 represents a vesselness measure to be used in a retinal blood vessel segmentation method. The proposed vesselness measure is based on analysis of the Hessian matrix, in which vessel centrelines and orientations at multiple scales are combined to measure the vesselness.

Chapter 6 presents an overview of the work done in this research, conclusions and avenues for future investigations.

1.4 Publications

The following is a list of publications derived from the work described in this thesis.

1.4.1 Journal papers

- N. M. Salem and A. K. Nandi, "Novel and adaptive contribution of the red channel in pre-processing of colour fundus images," *Journal of The Franklin Institute*. Special Issue: Medical Applications of Signal Processing, Part I, vol 344, issues 3-4, pp. 243–256, May-July 2007.

- S. A. Salem, N. M. Salem, and A. K. Nandi, "Segmentation of retinal blood vessels using a novel clustering algorithm RACAL with a partial supervision strategy," *Journal of Medical & Biological Engineering & Computing*, vol 45, pp. 261–273, March 2007.

- S. A. Salem, N. M. Salem, and A. K. Nandi, "Augmentation of a nearest neighbour clustering algorithm with a partial supervision strategy for biomedical data classification," Accepted for publication as Invited Paper in the Special Issue on Advances in Medical Decision Support Systems of *Expert Systems*.

- N. M. Salem, S. A. Salem, and A. K. Nandi, "Unsupervised and single parameter retinal blood vessels segmentation using a vesselness measure," submitted to journal of *Computers in Biology and Medicine*, June 2007.

1.4.2 Conference papers

- N. M. Salem and A. K. Nandi, "Enhancement of colour fundus images using histogram matching," *in Proceedings of the IASTED International Conference, BioMedical Engineering*, February 16-18, 2005, Innsbruck, Austria.

- N. M. Salem and A. K. Nandi, "Novel pre-processing of colour fundus images," in the *IEE Proceedings of Medical Application of Signal Processing*, November 3-4, 2005, London, UK.

- N. M. Salem and A. K. Nandi, "Segmentation of retinal blood vessels using scale-space features and *K*-nearest neighbour classifier," in *Proceedings of the 31st International Conference on Acoustics, Speech, and Signal Processing - ICASSP '06*, vol 2, pp. 1001-1004, May 14-19, 2006, Toulouse, France.

- S. A. Salem, N. M. Salem, and A. K. Nandi, "Segmentation of retinal blood vessels using a novel clustering algorithm," in *Proceedings of the 14th European Signal Processing Conference - EUSIPCO '06, September 4-8, 2006, Florence, Italy.*

- N. M. Salem, S. A. Salem, and A. K. Nandi, "Segmentation of retinal blood vessels based on analysis of the Hessian matrix and clustering algorithm," in *Proceedings of the 15th European Signal Processing Conference - EUSIPCO '07, September 3-7, 2007, Poznań, Poland.*

Chapter 2

Medical Background and Segmentation Methods

2.1 Introduction

THE main focus of this chapter is to give the necessary background about retinal images and to review blood vessel segmentation methods in the literature. The chapter begins with the medical background including the eye anatomy and the different imaging techniques used to capture these images. Contributions of digital image processing techniques to retinal image processing are also discussed, which include detection of DR, AMD, and other ocular diseases. The second part of this chapter reviews supervised and unsupervised methods for retinal blood vessel segmentation.

2.2 Medical Background

2.2.1 Anatomy of the eye

When comparing a camera to the eye, the camera has lens to focus the incoming light, then gather it, and finally transform that light into a picture. In the eye, the incoming light is refracted by lens and cornea onto the retina, then turned into nerve impulses by the photoreceptors acting as transducer cells. These impulses are sent to the brain along the

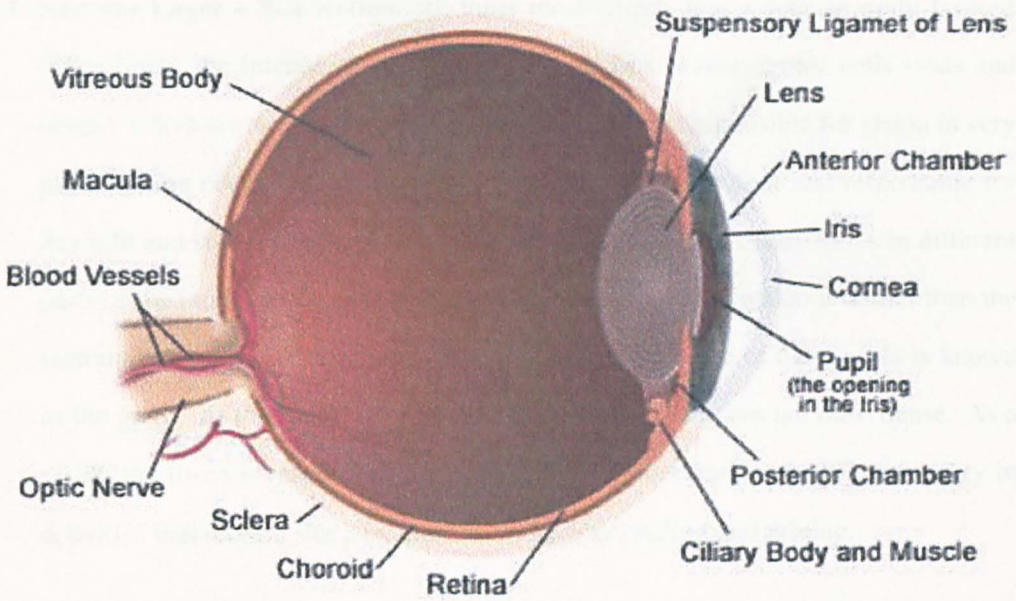

Figure 2.1: Anatomy of the eye [taken from `http://www.health.uab.edu/default.aspx?pid=26471`].

visual path to provide the visual impression [10]. Figure 2.1 shows the anatomy of the eye. The eyeball consists of of three layers which are the *fibrous* layer, the *vascular pigmented* layer, and the *nervous* layer [11]:

1. **Fibrous Layer** (the outer most layer): It is made up of the *sclera* and the *cornea*. The cornea is the clear and transparent part and forms the front 1/6 of this layer. All light must first pass through the cornea when it enters the eye. The posterior 5/6 of the eyeball is the opaque part and called the sclera. It is usually known as the "white of the eye" seen from the front and it maintains the shape of the eye.

2. **Vascular Pigmented Layer** (the middle layer): It consists of the *choroid*, the *ciliary body*, and the *iris*. The choroid is a thin and soft coat lining the inner surface of the sclera. It is extremely vascular and contains the blood vessels that nourish the outer layers of the retina and the anterior regions of the eye. The ciliary body is a muscular area that is attached to the lens, it contracts and relaxes to control the size of the lens for focusing. The iris is the coloured part of the eye, it has two muscles to control the amount of light passing into the eye.

3. **Nervous Layer – The Retina** (the inner most layer): It is a delicate multi-layered tissue lining the interior of the eyeball. It contains photoreceptor cells (rods and cones), which are the transducer cells. Rods are mainly responsible for vision in very poor lighting condition, while cones are adapted to bright light and responsible for daylight and colour vision. The density of the rods and the cones varies in different parts of the retina. In the centre of the retina, is the *macula*, which is darker than the surrounding retina. A depression area present in the centre of the macula is known as the *fovea*. At the fovea, the rods are absent while the cones are most dense. As a result, the fovea is responsible for seeing fine details clearly, which is necessary in activities that require sharp central vision such as reading and driving.

The retina is connected to the brain by the optic nerve, which conducts the electrical impulses from photoreceptor cells to the lateral geniculate nucleus in brain. The optic nerve head is the focus from which retinal arteries enter and retinal veins leave the eye. The optic nerve is comprised of axons from the retinal ganglion cells.

2.2.2 Retinal images

2.2.2.1 Imaging techniques

To determine the health of the eye, the internal structures of the eye, especially the retina, should be examined. The ophthalmoscope is used in the eye examination to detect changes in the eye due to ocular or systemic diseases. To keep a permanent record of the retina, there are two commonly used imaging techniques known as fluorescein angiographs and fundus images. Fluorescein angiography involves an intravenous injection of a fluorescein dye, and then a series of photographs of the fundus are taken using a fundus camera with appropriate filters allowing visualisation of the retinal blood vessels as the dye circulates. Fundus images are acquired by taking photographs of the back of the eye using a fundus camera. This technique is widely used in clinics as it is noninvasive and suitable for screening. Retinal images are used for diagnosis, treatment evaluation, and to follow up patients with ocular pathology [12].

2.2.2.2 Objects of interest

The objects of interest in the ocular fundus are: anatomical structures, lesions, abnormalities of anatomical structures. Figure 2.2 shows the main normal components. These objects can be organised as in [13] into three sub-classes (1-3) of objects and two specific (4-5) objects:

1. curvilinear objects (including blood vessels),
2. blobs brighter than blood vessels,
3. blobs darker than blood vessels,
4. the optic nerve,
5. the fovea.

These objects can be segmented or localised by using characteristics of these objects, such as texture, colour, size, and shape. Problems with retinal image processing are the poor quality and non-uniform illumination associated with these images. Typical retinal images are shown in Figure 2.3 which gives examples of different normal and abnormal images. Figure 2.3 (a) is an example of a normal retinal image, without any sign of ocular diseases, in which retinal blood vessels, optic disc, macula, and the fovea are clearly shown. Examples of abnormal images are shown in Figure 2.3 (b-f). Abnormalities in these figures are shown as a formation of new blood vessels, white or yellow spots, changes in vessel diameter and tortuosity. Figure 2.3 (f) gives an example of a poor quality image, where image components or abnormalities are not clearly shown.

2.2.3 Retinal blood vessels

The earliest representations of the retinal vessels in the human eye were drawn shortly after the advent of the ophthalmoscope in 1850, then the first illustration of the fundus drawn from life was first published in 1853 [14]. As a result of systemic or ocular disease, blood vessels can have measurable abnormalities in diameter, colour, and tortuosity, where

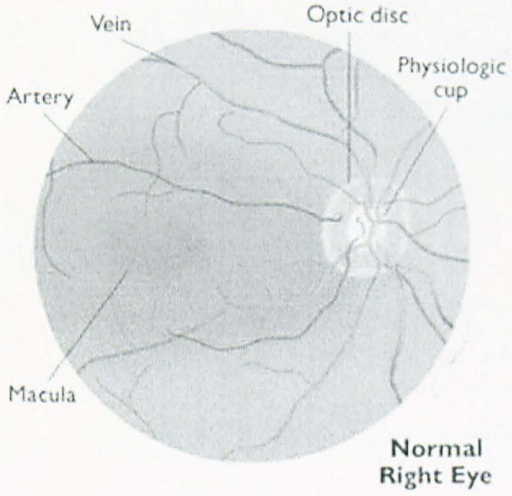

Figure 2.2: Main components of the ocular fundus.

vessels become curved, dilated, and having many turns. Information about blood vessels can be used in automated methods for diagnosis of various ocular diseases, and in image analysis and understanding to relate changes to disease severity. Furthermore, retinal blood vessels can be considered as landmarks in image registration to compare images taken over the years. Convergence of the blood vessel network is used to localise the optic disc as another region of interest in the retinal image.

2.2.4 Contributions of digital image processing

Recently, there has been a strong medical motivation to apply automatic processes in the field of retinal images. Digital image processing techniques can be used in image enhancement, segmentation, registration, analysis and understanding. Enhancement of retinal images can be used either to improve the visual appearance of retinal image in cases of poor quality and non-uniform illumination or as a pre-processing step to help in the detection of different anatomical structures or abnormalities. In image segmentation the main objective is the detection process to divide the image into meaningful regions each representing one object. There are two main areas where image segmentation techniques are applied to retinal images which are detection and localisation of anatomical structures (i.e. blood vessels, optic disc, and fovea) and detection of abnormalities (i.e. microaneurysms, hemorrhages,

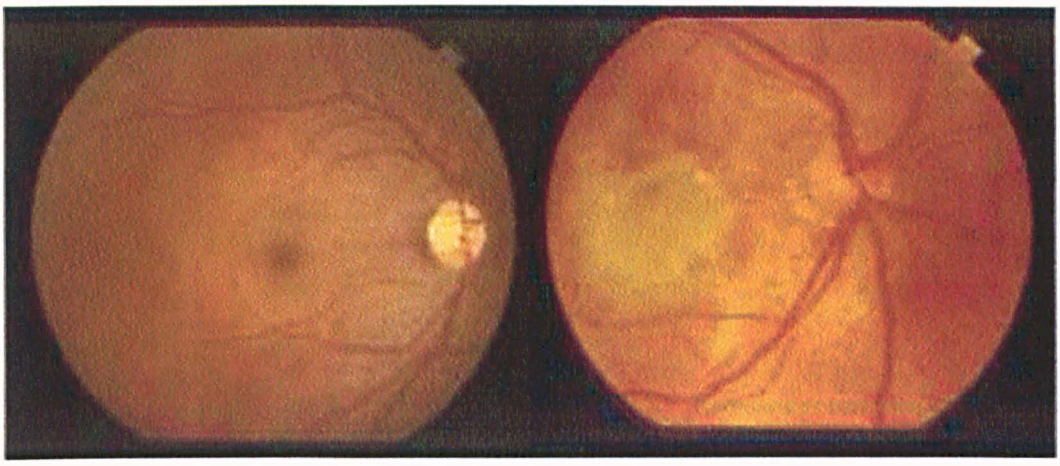

(a) Normal (b) Choroidal Neovascularisation and AMD

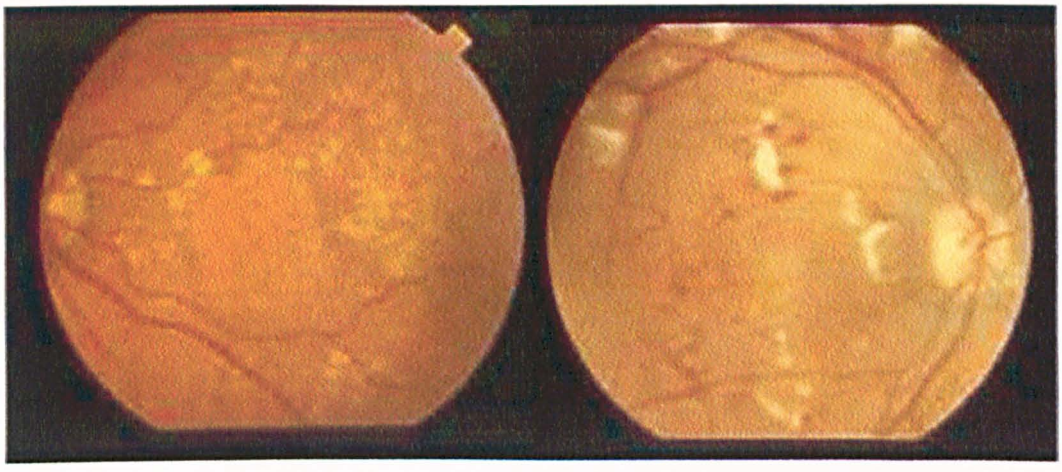

(c) Drusen (d) Hypertensive retinopathy

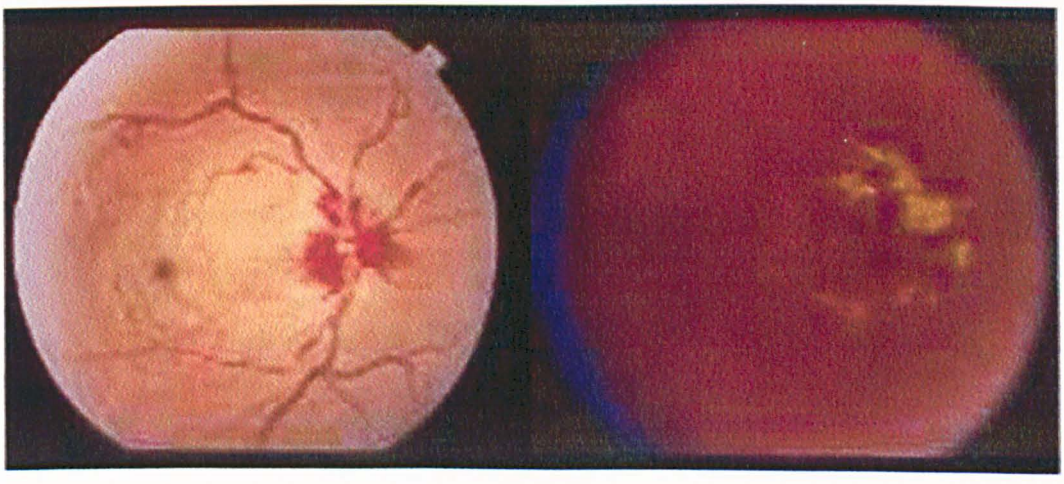

(e) Central retinal vein and artery occlusion (f) poor quality image

Figure 2.3: Typical retinal images [taken from `http://www.parl.clemson.edu/stare/manifestations.html`].

and hard exudates). Image registration is used to align a set of images (or one image to another) before examination, which is helpful when comparing images taken for the same patient at different times. Registration of retinal images is used to follow the evaluation of some lesions over the years or to compare images obtained under different conditions. The focus in image analysis and understanding is on the analysis of image contents to get a relation between the changes of anatomical structures and different diseases and grading disease severity.

2.2.4.1 Automatic retinal image processing

Diabetic retinopathy

Diabetes is a major health problem in industrialised countries and a rapidly emerging problem in urban areas in developing countries [15, 16]. The implications for the provision of eye care are evident as everyone with diabetes will eventually develop DR if they live long enough [15]. Studies have shown that people who suffer from diabetes benefit from regularly attending a screening session [17, 18], where retinas of both eyes are examined by an ophthalmologist and if DR is detected the patient can be treated or monitored further.

DR remains the commonest cause of new blindness in the working age population in the UK [19]. DR meets all the criteria for a disease that warrants screening, it has a long latent period before visual loss and is eminently treatable. As well, screening for retinopathy is noninvasive, cost-effective, highly sensitive and specific [20]. Timely treatment can prevent up to 98% of visual loss from DR [21].

Automated methods for DR detection start with quality assessment of retinal images [22, 23]. In [22], image clarity and field definition are used to define the quality of the image. Macular blood vessel visibility is used as an indicator for image clarity. The full FOV, optic disk, and a visible retinal region around the macula are used to define the field definition. In [23], a set of good quality images are used to train a statistical classifier to distinguish between good and low quality images. Anatomical structures detection is another important step in order to distinguish between responses from anatomical structures

and DR abnormalities. Retinal blood vessels, optic disk and the fovea are the important structures to be detected in DR screening programs [2, 24, 25, 26].

Methods for detection the signs of DR are based on retinal image segmentation, then generating a set of features for candidate regions followed by a classifier to classify these regions into exudates [27, 28, 29], microaneurysms [30], and red lesions [31]. In [27, 29], a fuzzy C-means clustering algorithm is used to segment retinal images into regions. Then neural networks are used to classify these segmented regions into exudates and non-exudates based on colour, size, texture, and edge strength. In [31], a pixel classification method is proposed to segment red lesions and blood vessel pixels from retinal images, followed by removing connected pixels which are considered as vessels. The remaining pixels are considered candidate pixels which are classified as lesions or not by using the *KNN* classifier in conjunction with a set of features (shape features and pixel intensity features).

Age-related macular degeneration

Age-related macular degeneration (AMD) is now the leading cause of blindness in the developed countries [15] and the most common cause of of vision loss in people over 50 years of age [32]. Over the last two decades, there has been continued interest in the use of digital techniques for quantification of macular pathology, particularly drusen. Drusen identification and measurement play a key role in clinical studies of this disease. Current manual methods of drusen measurements are laborious and subjective, and there is a potential for the use of automated techniques [33, 34] for detection and quantification of drusen in retinal images which will help in early detection and treatment of AMD.

Other ocular diseases

As a result of ocular diseases, the optic disc and the fovea can have a measurable abnormalities in size and shape. This also can affect the blood vessels in the form of diameter, colour, and tortuosity. Automated methods to detect these features can be used in computer aided diagnosis systems to give the specialist a second opinion.

In hypertension, commonly referred to as high blood pressure, the blood pressure is chronically elevated. Hypertension may result in focal constriction of retinal arteries in addition to an increase in length diameter ratio and decrease in branching angles [35]. Features such as bifurcation angle, artery-to-vein diameter ratio [36], mean artery and vein diameters are considered when analysing retinal images for hypertension detection [37, 38, 39].

Another common ocular condition is glaucoma, which is a disorder associated with pressure in the eye, and is characterised by damage to the optic nerve, with consequent visual loss. The cup-to-disc ratio is used in the automatic detection of glaucoma [40, 41].

2.2.4.2 Datasets

In this research, two publicly available datasets; STARE [42] and DRIVE [43] datasets are used for performance evaluation. The ground truth (GT) images are provided for all images in both datasets, i.e. retinal blood vessels segmented by human observers. These datasets have been widely used for performance evaluation of many segmentation methods.

STARE dataset

The STARE dataset consists of 20 images (ten images contain pathology and the other ten are normal) which are digitised slides captured by a TopCon TRV-50 fundus camera at 35° FOV. Each slide was digitised to produce a 605 × 700 pixels image, standard RGB, 8 bits per colour channel. Every image has been manually segmented by two observers to produce GT vessels segmentation.

The first observer segmented 615,726 pixels as vessel and 5,293,034 as background (10.4% vessel), the second observer marked 879,695 pixels as vessel and 5,029,065 as background (14.9% vessel). Subsequent review indicated that the first person took a more conservative view of the boundaries of vessels and in the identification of small vessels than the second observer [12]. The manual segmentation by the first observer is chosen as the GT for vessel segmentation verification. Typical images from the STARE dataset are shown in Figure 2.4.

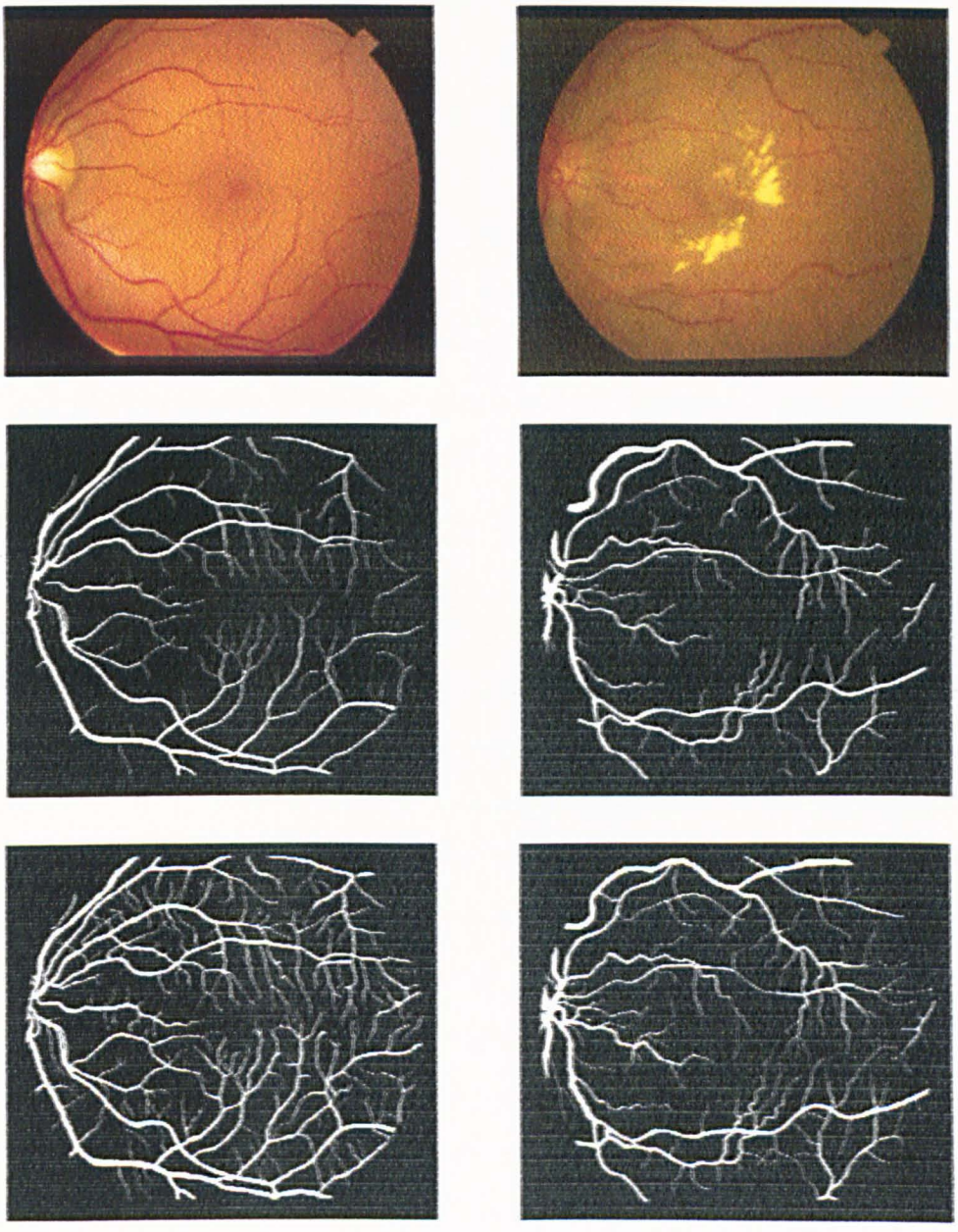

Figure 2.4: Normal (left) and abnormal (right) images from the STARE dataset (a) RGB, (b) first, and (c) second manually segmented images.

DRIVE dataset

The DRIVE database consists of 40 images captured by a Canon CR5 nonmydriatic 3CCD camera at 45° FOV. These images were captured in a digital form of size 584×768 pixels, standard RGB, 8 bits per colour channel. Seven of these images contain pathology while the other 33 are normal. The images are in compressed JPEG format, which is unfortunate for image processing but is commonly used in screening practice [44].

The 40 images have been divided into a training and test set, each containing 20 images (the training set has three images with pathology). They have been manually segmented by three observers trained by an ophthalmologist. The images in the training set were segmented once, while images in the test set were segmented twice, resulting in sets A and B. The observers of set A marked 577,649 pixels as vessel and 3,960,494 as background (12.7% vessel), for set B these numbers are 556,532 and 3,981,611, respectively (12.3% vessel). Performance is measured on the test set using the segmentations of set A as GT. Typical images from the DRIVE dataset are shown in Figure 2.5.

Images from both datasets are available as RGB images, 8 bits per colour channel. The RGB model is used to describe colour objects based on their primary spectral components of red, green, and blue. In this thesis, each component is referred to as a colour channel, i.e. red channel, green channel, and blue channel, with intensity values from 0 to $2^8 - 1$. Another way to describe a colour object is by using hue, saturation, and intensity (HSI) colour model. Hue describes the colour attribute (pure red or green). While saturation measures the degree to which the colour is diluted by white. The intensity describes the intensity of the colour [45]. Figure 2.6 shows the three channels for a normal retinal image using the RGB and HSI colour models. In the RGB, the red channel is the brightest, green channel has the highest contrast, while the blue channel is the darkest channel. The HSI is not suitable for image visualisation, but the intensity channel can be used in other applications.

Field of view (FOV) is the region of interest in the retinal image which contains all anatomical structures. In all retinal images that are available from both datasets, the FOV

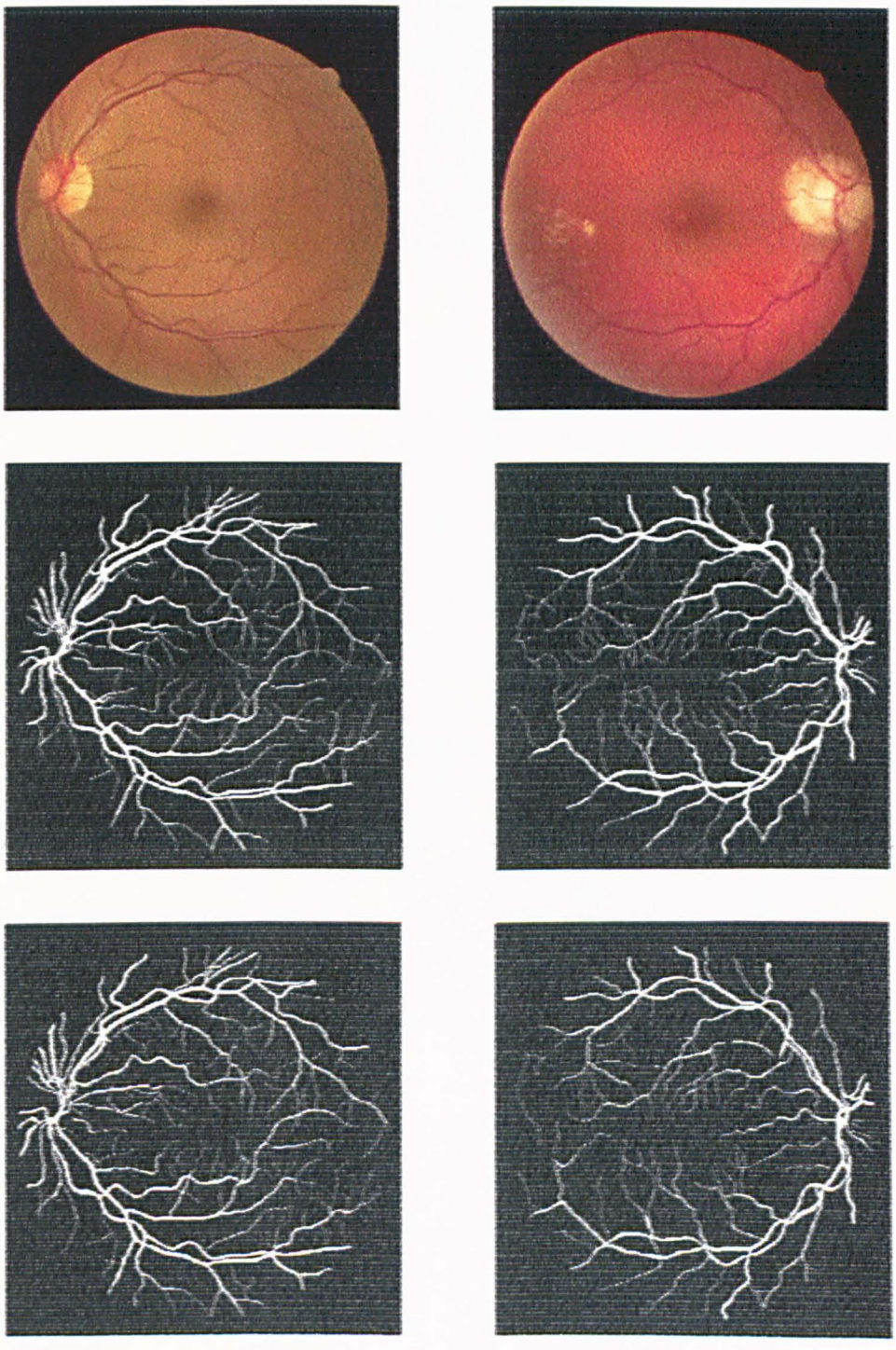

Figure 2.5: Normal (left) and abnormal (right) images from the DRIVE dataset (a) RGB, (b) first, and (c) second manually segmented images.

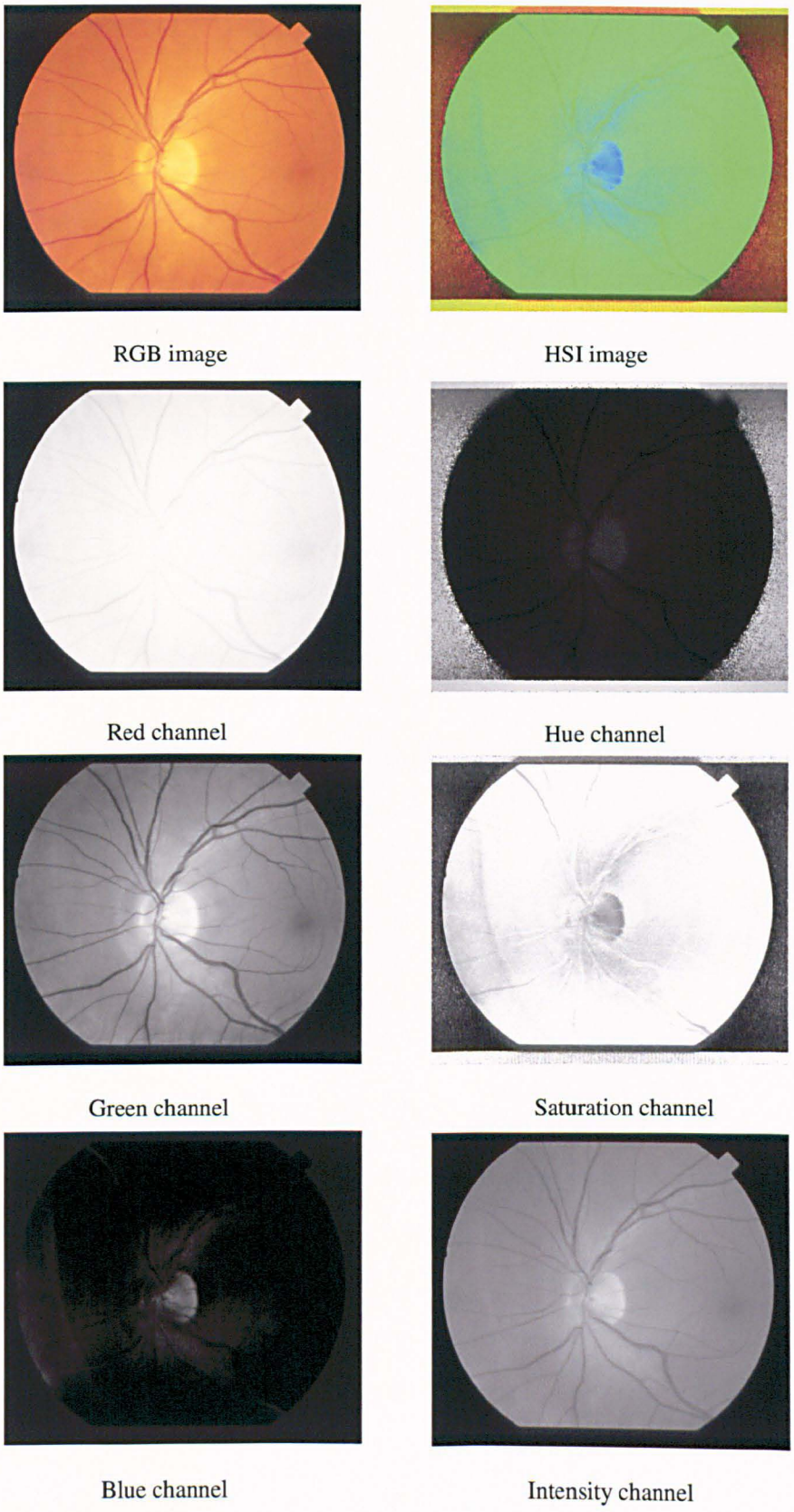

Figure 2.6: RGB and HSI colour models.

is surrounded by a black region, which does not provide any useful information. In retinal image processing, it is required to reduce the processing time, in other words, it is required to segment/extract the retinal FOV. This can be achieved by producing a binary mask for each image, to limit the processing within the FOV. This binary mask can be generated by thresholding the image using a threshold value. This method is very simple, but the threshold value is not constant for all images, which require an automatic selection for the threshold value.

Figure 2.7 illustrates different application of image processing techniques in the field of retinal images, such as illumination equalisation, vessel detection, and drusen detection

Images from these datasets have been used for performance evaluation of vessel segmentation methods [12, 44, 46, 47, 48, 49, 50, 51, 52, 53, 54], centreline detection [53], optic disc localisation and detection [7, 55, 56, 57, 58], and image analysis to obtain a description of the global vascular structure [59]. Some of these given references use only one dataset for performance evaluation, in other cases both datasets were used.

The STARE dataset is used for performance evaluation for proposed blood vessel segmentation methods, as it has ten images with pathology and ten normal images, giving a good opportunity to test proposed methods in both normal and abnormal retinas. The DRIVE dataset, where images are in a compressed JPEG format, is only used for the performance evaluation of the binary mask generation step as it provides the binary masks for each image in the dataset.

2.2.4.3 Performance measure

Receiver Operating Characteristic (ROC) curves are used for performance visualisation and to compare between classifiers based on their performance [60, 61].

For hard classification, when the output of the classifier is either positive (P) or negative (N), there are four possible scenarios as summarised in Table 2.1 (which is known as confusion matrix or contingency table). If a sample is P and is classified as P, then it is counted a true positive (TP), while counted as a false negative (FN) if it is classified as N. On the other hand, if a sample is N and is classified as N, then it is counted as a true

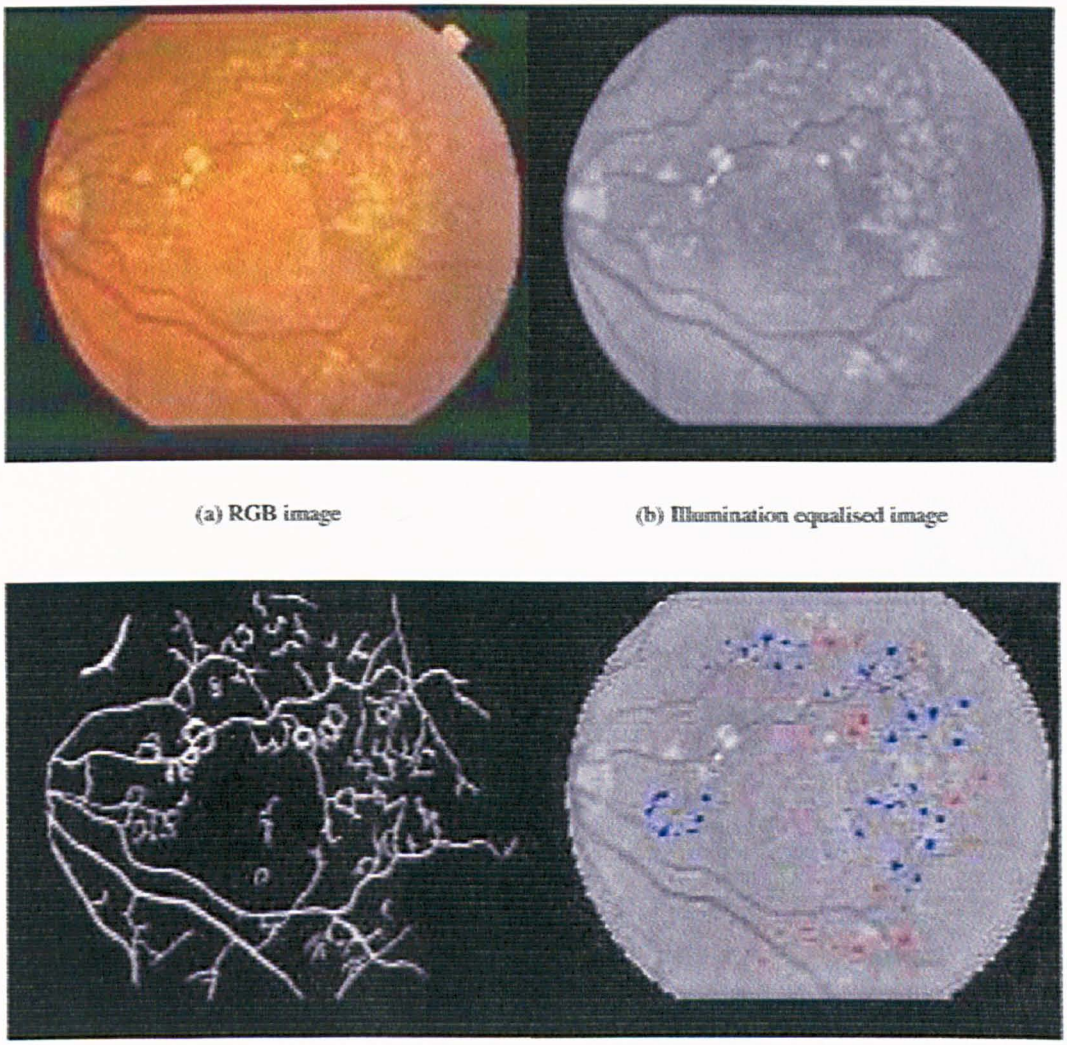

(a) RGB image

(b) Illumination equalised image

(c) Vessel segmentation

(d) Drusen detection

Figure 2.7: Different processed versions of a retinal image from the STARE dataset [taken from `http://www.parl.clemson.edu/stare/images1.htm`].

Table 2.1: Confusion matrix for a two class classifier

		GT	
		P	N
Classifier output	P	TP	FP
	N	FN	TN

negative (TN), while counted as a false positive (FP) if it is classified as P. Accuracy, true positive rate (TPR), and false positive rate (FPR) are three measures that are commonly used in performance evaluation, which are given by:

$$accuracy = \frac{TP+TN}{TP+FP+FN+TN}$$

$$TPR = \frac{TP}{TP+FN}$$

$$FPR = \frac{FP}{FP+TN}$$

The accuracy is the percentage of the correctly classified samples. The TPR or sensitivity is the proportion of the positive GT that classified as positive. The specificity is the proportion of the negative GT that classified as negative which is equal to 1-FPR.

In case of classifiers with soft output, which allow the output to belong to all classes with different degrees of membership, a threshold is needed to produce a binary output. For each threshold value, there will be a different point and tracking these points will result in a curve. An ROC curve plots the false positive rates against the true positive rates as the discrimination threshold is varied. An example of an ROC curve is given in Figure 2.8. The ideal case, when the classification result is 100%, is shown at the point in the top left corner. Random classifiers give a straight line at an angle 45^o (i.e. $x = y$). Some implementation notes are given in Appendix A.1.

In this thesis, the performance of segmentation methods is measured using ROC curves, where TPR and FPR are defined in the same way as in [12]. The true (false) positive is any pixel which was hand-labelled as a vessel (not vessel), whose intensity after segmentation is above a given threshold. The true (false) positive rate is established by dividing the number of true (false) positives by the total number of pixels hand-labelled as vessels (not vessels).

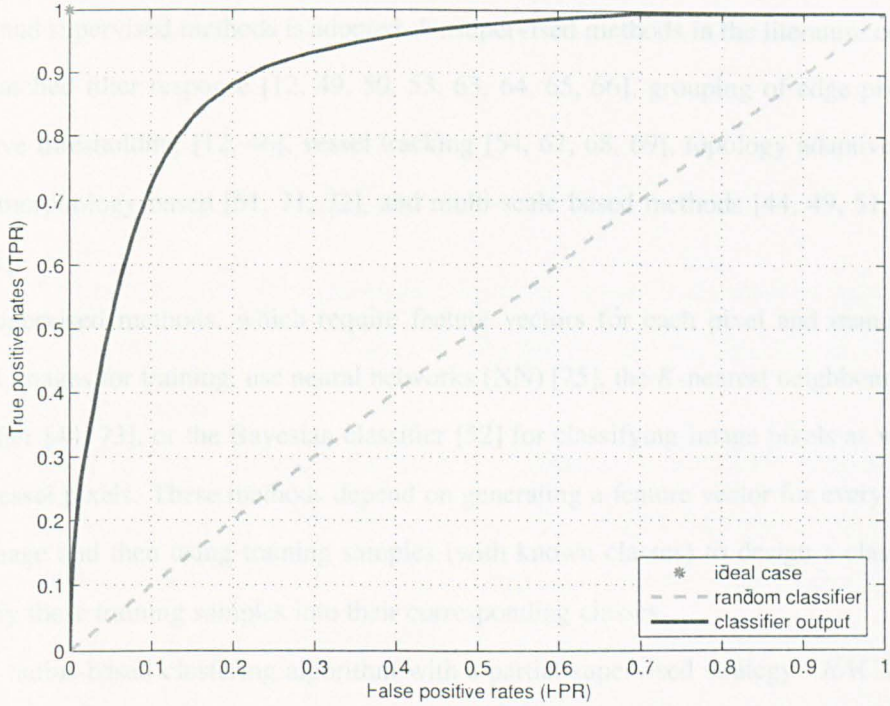

Figure 2.8: ROC curves.

2.3 Vessel Segmentation Methods

Blood vessel segmentation methods can be divided into pattern recognition, model-based, tracking-based, artificial intelligence-based, neural network-based, and tube-like object detection approaches [62]. In the field of retinal images, approaches for segmenting blood vessels can be classified according to different criteria:

- In [12], segmentation methods are divided into three categories: kernel-based, classifier-based, and tracking-based methods,
- In [51], these approaches are classified as pixel processing-based and tracking-based methods,
- In [44], segmentation methods are divided into rule-based and supervised methods.

In this research, the last category for classifying vessel segmentation methods into unsupervised and supervised methods is adopted. Unsupervised methods in the literature comprise the matched filter response [12, 49, 50, 53, 63, 64, 65, 66], grouping of edge pixels [6], adaptive thresholding [12, 46], vessel tracking [54, 67, 68, 69], topology adaptive snakes [70], morphology based [51, 71, 72], and multi-scale based methods [44, 49, 51, 52, 53, 73, 74].

Supervised methods, which require feature vectors for each pixel and manually labelled images for training, use neural networks (NN) [75], the K-nearest neighbour (*KNN*) classifier [44, 73], or the Bayesian classifier [52] for classifying image pixels as vessel or non-vessel pixels. These methods depend on generating a feature vector for every pixel in the image and then using training samples (with known classes) to design a classifier to classify these training samples into their corresponding classes.

A radius-based clustering algorithm with a partial supervised strategy - *RACAL* - was proposed by Salem and Nandi [76] to classify data objects according to a feature vector, using a fraction from the GT. The authors applied *RACAL* to classify breast cancer tumors to either benign or malignant. Similarly, *RACAL* can be applied to segment the retinal blood vessels, where only a fraction of the image pixels are required to be manually labelled (not all the entire image pixels). In Chapter 4, Section 4.5, this algorithm is used to segment blood vessels from colour fundus images and is modified in order to be used as a classifier.

2.3.1 Unsupervised methods

Matched filters based methods

Segmentation methods that are based on matched filters start with convolving the image with a kernel specially designed to extract objects of interest - blood vessels - then followed by other image processing steps to get the final results. Chaudhuri *et al.* [63] proposed a two dimensional matched filter for segmenting retinal blood vessels assuming that a vessel has a Gaussian profile, fixed width, and a fixed piecewise linear orientation. Profile across one row from a retinal images is shown in Figure 2.9 (a), the region defined by the rect-

angle is enlarged in Figure 2.9 (b) where three blood vessels give responses that can by approximated by a Gaussian function. The convolution kernel is mathematically expressed as:

$$K(x,y) = -\mathrm{e}^{-\frac{x^2}{2\sigma^2}} \qquad \text{for } |y| \leq \frac{L}{2} \tag{2.1}$$

where L is the length of the segment for which the vessel is assumed to have a fixed orientation, σ defines the spread of the intensity profile, and the direction of the vessel is assumed to be aligned along the $y-$axis.

As a result of having different orientations, 12 different kernels are used to search for vessel segments along all possible directions over 180°. Figure 2.10 shows two kernels at different angles using $\sigma = 2$ and $L = 9$. Each convolution kernel is modified by subtracting its mean value, so the expected filter output is - ideally - zero in the background. First the green channel is smoothed with 5×5 mean filter to reduce the effect of noise, then convolved with all 12 kernels with the output at each pixel being the maximum for the 12 orientations. Result of applying the matched filter for an abnormal image from the STARE dataset is shown in Figure 2.11. The main advantage of this method is that it results in a good initial estimate of the vessels in the image. On the other hand it gives some responses which do not resemble any blood vessels and vessels of small widths are missed.

Equation 2.1 was used as a first step then followed by thresholding strategies [12, 64, 66] to segment retinal blood vessels. Hart *et al.* [64] described an automated tortuosity measurement technique for blood vessel segments in retinal images. They segmented retinal blood vessels using the 2D matched filter, followed by applying thresholding and thinning processes to get the binary image containing the vessel segments. In the piecewise threshold probing method proposed in [12], the matched filter response (MFR) image, resulting from convolution with matched filter, is probed. During each probing, the threshold of the probed region is determined according to testing a set of criteria, and ultimately it is decided if the area being probed was a blood vessel or not. Figure 2.12 shows results of the piece-wise threshold probing method for two images from the STARE dataset which are

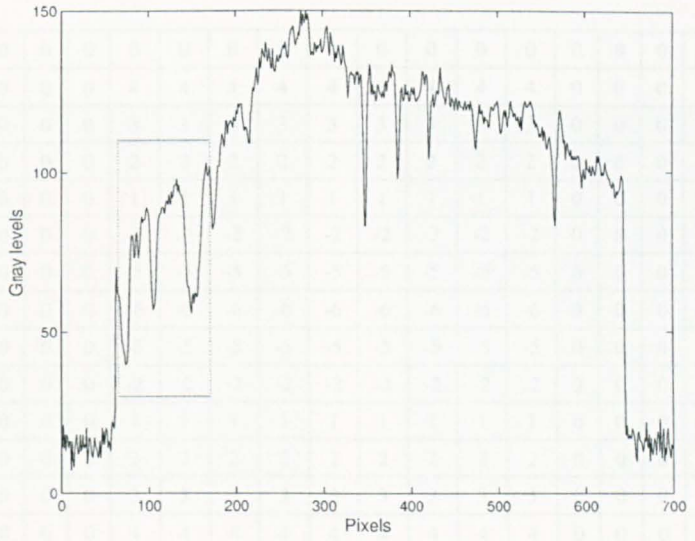

(a)

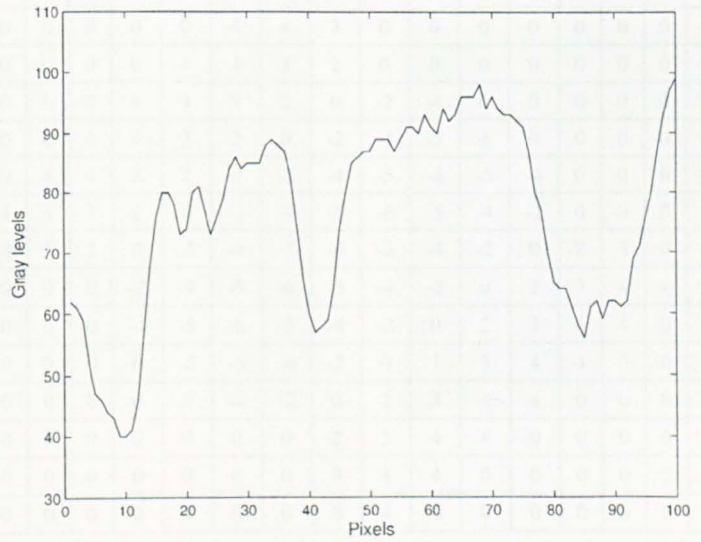

(b)

Figure 2.9: (a) Profile across a horizontal line through one row in an image, and (b) the region defined by the rectangle in (a).

0	0	0	0	0	0	0	0	0	0	0	0	0	0	0	0
0	0	0	4	4	4	4	4	4	4	4	4	0	0	0	0
0	0	0	3	3	3	3	3	3	3	3	3	0	0	0	0
0	0	0	2	2	2	2	2	2	2	2	2	0	0	0	0
0	0	0	1	1	1	1	1	1	1	1	1	0	0	0	0
0	0	0	-2	-2	-2	-2	-2	-2	-2	-2	-2	0	0	0	0
0	0	0	-5	-5	-5	-5	-5	-5	-5	-5	-5	0	0	0	0
0	0	0	-6	-6	-6	-6	-6	-6	-6	-6	-6	0	0	0	0
0	0	0	-5	-5	-5	-5	-5	-5	-5	-5	-5	0	0	0	0
0	0	0	-2	-2	-2	-2	-2	-2	-2	-2	-2	0	0	0	0
0	0	0	1	1	1	1	1	1	1	1	1	0	0	0	0
0	0	0	2	2	2	2	2	2	2	2	2	0	0	0	0
0	0	0	3	3	3	3	3	3	3	3	3	0	0	0	0
0	0	0	4	4	4	4	4	4	4	4	4	0	0	0	0
0	0	0	0	0	0	0	0	0	0	0	0	0	0	0	0

(a)

0	0	0	0	0	0	4	0	0	0	0	0	0	0	0	0
0	0	0	0	0	4	4	3	0	0	0	0	0	0	0	0
0	0	0	0	4	4	3	2	0	0	0	0	0	0	0	0
0	0	0	4	4	3	2	0	-2	-4	0	0	0	0	0	0
0	0	4	4	3	2	0	-2	-4	-5	-6	0	0	0	0	0
0	4	4	3	2	0	-2	-4	-5	-6	-5	-4	0	0	0	0
4	4	3	2	0	-2	-4	-5	-6	-5	-4	-2	0	0	0	0
0	3	2	0	-2	-4	-5	-6	-5	-4	-2	0	2	3	0	0
0	0	0	-2	-4	-5	-6	-5	-4	-2	0	2	3	4	4	0
0	0	0	-4	-5	-6	-5	-4	-2	0	2	3	4	4	0	0
0	0	0	0	-6	-5	-4	-2	0	2	3	4	4	0	0	0
0	0	0	0	0	-4	-2	0	2	3	4	4	0	0	0	0
0	0	0	0	0	0	0	2	3	4	4	0	0	0	0	0
0	0	0	0	0	0	0	3	4	4	0	0	0	0	0	0
0	0	0	0	0	0	0	0	4	0	0	0	0	0	0	0

(b)

Figure 2.10: Two different kernels at (a) $\theta = 0°$, and (b) $\theta = 45°$.

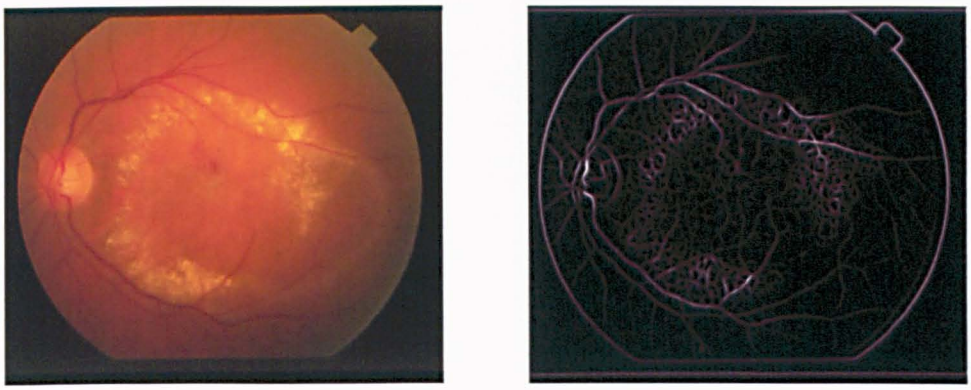

(a) (b)

Figure 2.11: Result from the two dimensional matched filter for an abnormal image (a) RGB image, and (b) MFR image.

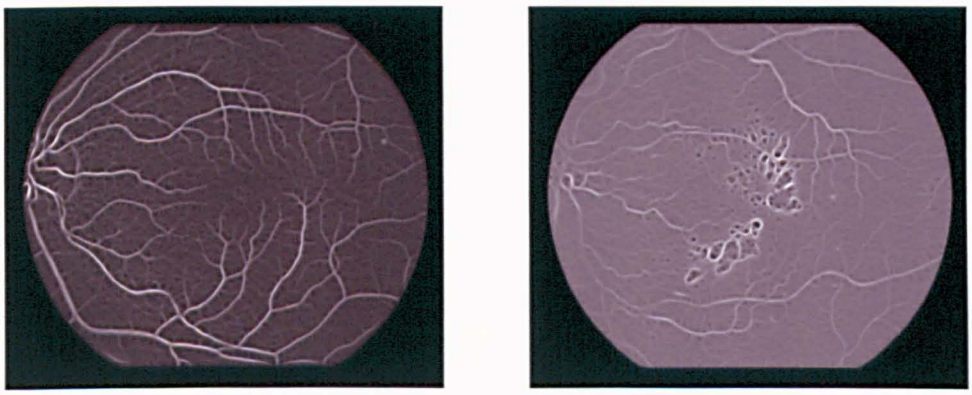

(a) (b)

Figure 2.12: Result from the Hoover method for (a) normal, and (b) abnormal images [taken from `http://www.parl.clemson.edu/stare/probing/`].

available at [42].

To extract anatomical structures from retinal images, the matched filter is used in conjunction with entropy thresholding and connected component analysis in [66].

Equation 2.1 assumes that blood vessels are of constant width and different orientations, so it uses fixed values for parameters which improved in [50], where the parameters for the matched filter are varied and chosen according to an optimisation procedure. While in [49, 53], the MFR is calculated at different scale values to extract vessels of varying widths by introducing a multi-scale matched filter.

Adaptive thresholding based methods

Thresholding is the simplest segmentation method for dividing an image to a set of regions or objects. The only parameter that needs to be set is the threshold value which can be determined from the image histogram. In retinal images, segmentation can not be achieved using the gray-level threshold with a single threshold value. This is because of the non-uniform illumination and poor quality in addition to the sharing of the same gray-level intensities by different objects. Adaptive threshold methods are used to solve this problem, in which different threshold values are applied to different regions in the retinal image.

The method proposed by Hoover *et al.* [12] is one of the adaptive threshold based methods where different image regions were thresholded at different threshold values based on a probing technique. The work in [46] is based on a verification based multi-threshold probing scheme, in which a binary image is obtained at different threshold values and each time vessels were selected based on verification steps.

Tracking based methods

Vessel tracking approaches start from an initial point, detect vessel centrelines or boundaries guided by local information, then analyse the pixels orthogonal to the tracking direction. Zhou *et al.* [67] developed a method to detect and quantify retinopathy in digital retinal angiograms. This algorithm relies on a matched filtering approach coupled with a priori knowledge about retinal vessel properties. The tracking algorithm is an adaptive

iterating procedure and models the vessel profile using Gaussian function. This method requires the user to identify starting and ending search points manually, while junctions are not taken into account.

To overcome the problem of initialisation, the optic nerve in fundus images is detected and used as the starting point in [68, 69]. Tolias *et al.* [69] proposed a fuzzy C-means (FCM) clustering algorithm that is based on the intensity information to track vessels in fundus images. This algorithm is initialised by defining the optic nerve as a very bright region to be the starting point to track image vessels. However, it ignores the possibility of locating abnormalities that have the same properties as the optic nerve. Moreover, vessels of small diameter and low contrast were missed. The scheme proposed by Wu *et al.* [54] is based on adaptive contrast enhancement and feature extraction steps to find candidate points for the tracking algorithm. Tracking of vessels was done via forward detection, bifurcation identification, and backward verification.

Incorrectly identified initial points is the most important issue in tracking algorithms which affects the performance of these algorithms. In addition, vessel-tracking techniques may be confused by vessel crossing and bifurcations. However, it can provide very accurate measurements of vessel width and tortuosity [77]. The ideal vessel tracking algorithm should have the following characteristics [69]:

- automatic initialisation and termination,
- automatic definition of centreline and vessel edges,
- efficient handling of junctions and forks.

Morphology based methods

Linearity and connectivity are two main features of blood vessels' shape that are known a priori and used by morphological image processing. Morphological operators such as dilation and erosion are used to add or subtract a structuring element (SE) of certain intensity to the image. Objects in an image can be separated by opening (erosion followed by

dilation) with certain SE of certain shape, while holes within an image can be filled using closing (dilation followed by erosion).

Morphological filters were proposed by Zana and Klein in [72] to segment vessel-like patterns from retinal images, where vessel was defined as a bright pattern, piece-wise connected, and locally linear. In order to differentiate vessels from analogous background patterns, a cross-curvature evaluation was performed. Another mathematical morphology approach was proposed by Walter and Klein in [71] which uses the top-hat transform calculated from the supremum of openings with large linear SE in different directions.

Mendonça and Campilho [51] combined the centrelines detection with multi-scale morphological reconstruction to segment retinal blood vessels. A modified top-hat transform with variable size SE followed by a binary morphological reconstruction method was used to obtain binary maps of the vessels at different scales. Finally, a region growing step was used to obtain the final segmentation results.

Multi-scale based methods

As blood vessels in retinal images are of different widths, so it is useful to segment these vessels at different scales, i.e. wider vessels are segmented at large scale values, while thin vessels are segmented at smaller values of scales. Segmentation methods that are based on multi-scale analysis interact with other approaches such as matched filters, morphological operators, and region growing. For example, responses of the matched filter [63] are derived at multiple scales in [49, 53], while multi-scale morphological operators are used in [51]. In the work proposed in [74], gradient magnitude and the ridge strength, which are extracted at multiple scales, are combined with a two-stage region growing procedure to segment the blood vessels from red-free images and fluorescein angiographs.

Moreover, features derived at multiple scales are used in conjunction with supervised classifiers to segment retinal blood vessels [52, 73]. The first and second derivatives - of the green channel image, in $x-$ and $y-$ directions [73], or with respect to other image coordinates [44] at different scales - are used as features for every pixel in the retinal image. Other features are extracted from calculations of the Gabor wavelet transformation at

multiple scales [52] as will be explained in the following section.

2.3.2 Supervised methods

Neural networks (NN) were proposed for use in retinal images for blood vessel segmentation by Sinthanayothin *et al.* [75]. Contrast enhancement and intensity normalisation were achieved via a local adaptive contrast enhancement step which applied to the intensity band of the retinal image. Principal component transformation was applied to the colour image to rotate the axes from RGB to three other orthogonal axes (principal axes of correlation). The first principal component was chosen from the three components as values along the first axis exhibited the maximum correlated variation of the data, i.e. contains the main structural features. A feature vector (of size 200 which are the first principal component and its edge strength values from a sub-image of 10 $\times$ 10 pixels) was generated for each pixel and then used as input to the NN. A post-processing step was required to reclassify small isolated regions of pixels that were misclassified as blood vessels.

Niemeijer *et al.* [73] proposed a pixel classification method based on a feature vector, which consists of 31 features (these features are the green channel image intensity, and the filtered image using the Gaussian and its derivatives at different scale values). The *KNN* is then used to classify image pixels into vessel or non-vessel pixels. Staal *et al.* [44] proposed a primitive-based method which is based on extraction of ridges that coincide approximately with vessel centrelines. Ridges were used as primitives for describing line elements, then each pixel was assigned to the nearest line element to form image patches. For every pixel, feature vectors that make use of the properties of the patches and the line elements were computed and then classified using the *KNN* classifier. As there are many features, a feature selection scheme was used to select features which provide the best classification results.

Another supervised method based on Gabor wavelet was proposed by Soares *et al.* [52]. The FOV border was extended in a pre-processing step in order to reduce false detection by the wavelet transform at the borders of the FOV. The two-dimensional Gabor wavelet transform was computed (because of its capability for detecting oriented features) at different

orientations and the maximum modulus over all possible orientations was taken. Feature vectors were composed of the pixel's intensity and the maximum modulus of the wavelet transform over all angles (from 0° to 170° at steps of 10°) for multiple scales. Finally, the segmentation was achieved using a Bayesian classifier in which each class-conditional probability density function was described as a linear combination of Gaussian functions.

2.4 Summary

In this chapter, the necessary medical background about retinal images is introduced and different contributions of digital image processing in the field of retinal image processing are given. The second part of this chapter presents a survey on the main supervised and unsupervised segmentation methods used to extract blood vessels from colour fundus images.

Automatic processing of retinal images is a demanding research area, where many aspects should be considered such as sensitivity, specificity, reliability, and complexity. Supervised methods require generating a feature vector for each pixel in the image, and then training a classifier using a set of manually labeled images. These methods provide high sensitivity and specificity values. Performance of supervised methods depends on the generated set of features and the training set. Complexity of these methods is proportional to the size of the feature vector and the training set. On the other hand, unsupervised methods have the advantage of being more computationally effective and there is no need for manually labeled images or feature extraction. Performance of unsupervised method is lower than that of supervised methods. There is a trade-off between performance and complexity, in addition to the availability of manually labeled images.

In this research, one of the considered issues is the processing time which is reduced by using a binary mask to segment the retinal FOV and generating a feature vector of a small size. Performance is another important issue, where high sensitivity and specificity values are obtained from supervised classification. For this reason supervised and semi-supervised segmentation methods are investigated, and a modification to the *RACAL* is proposed to act

as a classifier. This modification is very important for automated purposes and results in a higher sensitivity and specificity values than those obtained by the *KNN* classifier.

Chapter 3

Pre-processing of Colour Fundus Images

3.1 Introduction

DIGITAL colour fundus images are available as true colour images, i.e. RGB images. In order to segment retinal blood vessels from colour fundus images, only one channel is used from the three colour channels (red, green, and blue). The green channel is widely used in segmentation methods as it has the highest contrast. In general, results from using the green channel to segment retinal blood vessels are better than results obtained when using the red channel. This statement is true for normal images with uniform illumination. For abnormal images, the green channel has a high contrast between abnormalities and the retinal background. Consequently, these abnormalities will give responses similar to those obtained for blood vessels, which results in high rate of false positives. In case of non-uniform illuminated images, the red channel is brighter than the green channel, resulting in better visualisation/segmentation of blood vessels. In addition to the fact that the region of interest in retinal images is the retinal FOV (which is shown in colour fundus images surrounded by a black background). The red channel has the highest contrast between the retinal FOV and the background region, as it is the brightest channel, therefore it is used to segment the FOV.

In this chapter, a novel contribution of the red channel is presented, where two steps for pre-processing colour retinal images are proposed. The first step is to generate a binary mask in order to avoid processing the dark region around the retinal FOV. The second step is to enhance the retinal image by combining intensity information from red and green channels to get advantages from both channels.

Pre-processing of retinal images in the literature is used in reducing the effect of noise [63], the detection of anatomical structures [75, 78] or abnormalities [24], automatic mask generation [79], colour normalisation [27, 80], and visual image quality assessment [81]. Retinal images were smoothed by a 5×5 mean filter to reduce the effect of spurious noise in [63] and transformed using wavelet transform in [78], where the optic nerve head was enhanced by modifying the wavelet coefficients by suppressing the small scale coefficients and enhancing the larger scale coefficients. To detect the main components of the fundus, i.e. the optic disc, fovea, and blood vessels, Sinthanayothin *et al.* [75] presented a pre-processing step to reduce the effect of changing the contrast in different regions of the fundus image and to normalise the mean intensity. This was accomplished by transforming the intensities of the three colour bands to an HSI representation, then enhancing the contrast of the intensity by a locally adaptive transformation.

3.2 Automatic Mask Generation

3.2.1 Introduction

Mask generation aims to avoid processing the black region that surrounds the FOV of retinal images. As the background region around the FOV occupies roughly about 30% of the retinal image, then excluding this dark region will result in decreasing the required processing time. To the best of our knowledge, the only published methods for binary mask generation are reported in [79, 82]. In the work proposed by Gagnon *et al.* [79], statistical measures were used to label the pixels outside the FOV. In [79], statistics were

calculated for each colour channel of the image followed by a 4-sigma thresholding with a free parameter empirically chosen such that pixels with intensity value above that threshold were considered to belong to the FOV. Then, results for all bands were combined through logical operations and region connectivity test in order to identify the largest common mask (due to the difference colour response of the camera, and FOV size is not always the same for each colour channel). No qualitative results were reported.

In [82], a mask generation method is proposed, where the red channel of the colour retinal images is thresholded. Then a median filter is used to remove the artifacts followed by a manual removal of the fundus notch. Finally, an erosion filter is applied to reduce the interior size of the obtained binary mask. This method failed in generating masks for poor quality images, in addition to removing the notch manually. In the automatic processing of retinal images, it is required to generate binary masks for retinal images automatically. In the next Section, an automated method for binary mask generation is proposed.

3.2.2 Method

From the three colour channels (red, green, and blue) of the fundus image, the red channel has the highest brightness which results in high contrast between FOV and the dark surrounding region. For this reason, the binary mask for a colour retinal image is generated from the red channel. This is illustrated in Figure 3.1, when plotting a horizontal line through the three colour channels, at the start (end) point of the FOV there is a considerable variation between gray-level intensities before and after this point which is greater in the red channel than in other channels.

Points of large variations in rows and columns are used to define a rectangle that is tangential to the FOV of the retinal image. Then pixels outside this rectangle are chosen as seeds to be used next in a region growing step. Statistical measures such as mean and standard deviation values are used as criteria for the region growing to find the pixels outside the FOV.

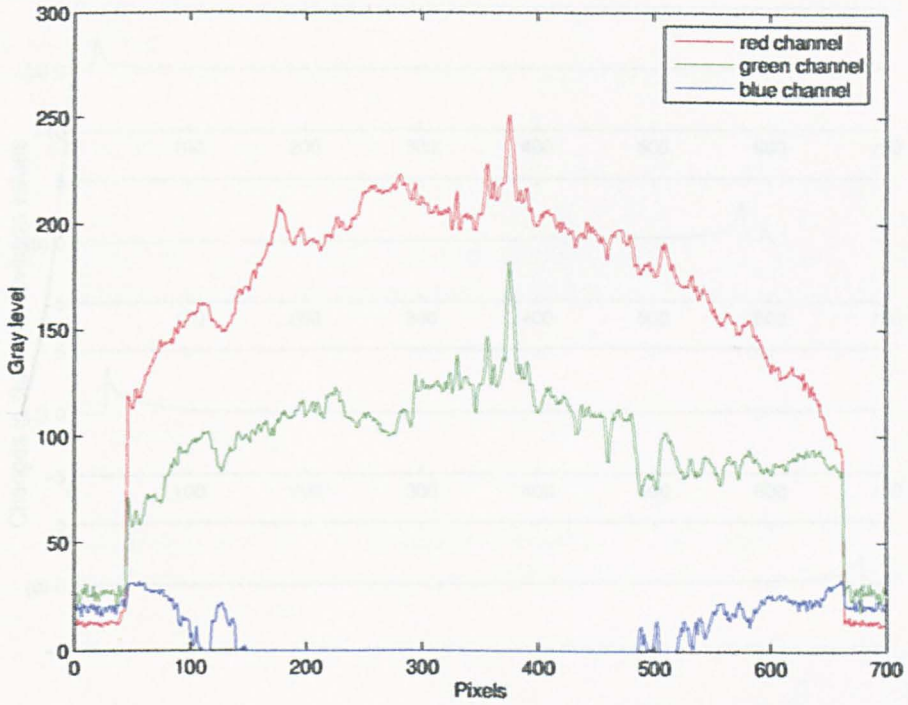

Figure 3.1: Gray-level intensities across one row from the three channels of a colour retinal image.

3.2.2.1 Surrounding rectangle

To determine a rectangle surrounding the FOV, maximum changes in standard deviation values are calculated for successive regions that contain number of rows (columns) from the red channel image. The region that includes the row (column) from where the FOV starts has the highest difference between its standard deviation and the region that contains the previous rows (columns), because at this row (column) values of gray-level intensities start to increase rapidly. The rectangle that surrounds the FOV is defined by rows (r_1 and r_2) and columns (c_1 and c_2).

To find the first row (r_1) from where the FOV starts, i.e. look for the first maximum in the difference between standard deviation values of the region contains the first (i) rows and the region contains the first ($i + 1$) rows as shown in Figure 3.2 (a). To find the last row (r_2) where the FOV ends, i.e. look for the first maximum in the difference between the

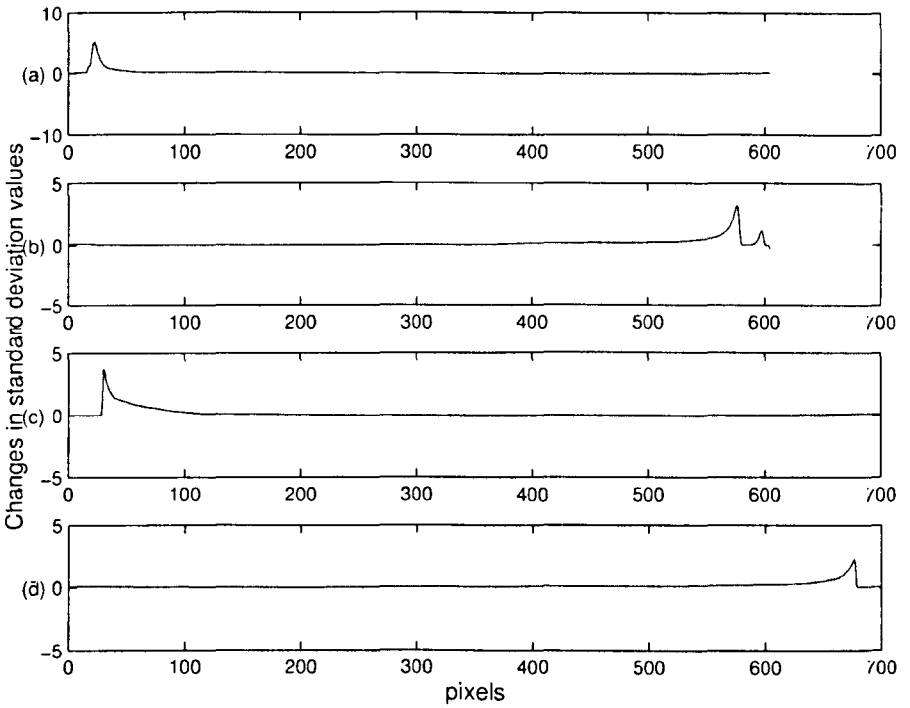

Figure 3.2: Change in standard deviation values between successive regions.

standard deviation values of the region contains the last (i) rows and the region contains the last ($i + 1$) rows as shown in Figure 3.2 (b). Similarly for the columns (c_1 and c_2) as shown in Figure 3.2 (c and d). These procedures are summarised in Figure 3.3.

3.2.2.2 Region growing

In the region growing step, pixels outside the previously defined rectangle are used as seed pixels. Standard deviation and mean values for a pixel's neighbourhood are used as criteria to add new pixels to the background region. There are three parameters: T_{mean}, T_{std}, and $T_{block-size}$. T_{mean} and T_{std} define the mean and standard deviation threshold values for the intensity in the pixel's neighbourhood, and $T_{block-size}$ defines the number of pixels in the neighbourhood. Another parameter that can be added to these parameters is T_{mar} to define a margin in order to select a number of pixels as seeds and not selecting all pixels outside the surrounding rectangle.

Algorithm 1 Rectangle surrounding the FOV

Input: I_r (red channel image)
Outputs: r_1, r_2, c_1, and c_2 (values for rows and columns of the rectangle)

r_s and c_s are number of rows and columns in I_r

For $i = 1 : r_s - 1$
  std_i = standard deviation for region contains the first i rows
  std_{i+1} = standard deviation for region contains the first $i + 1$ rows
  $std_{diff_1}(i) = std_{i+1} - std_i$
EndFor

$std_{diff_1}(r_1) = max(std_{diff_1})$

For $j = r_s : -1 : 2$
  std_j = standard deviation for region contains the last $r_s - j + 1$ rows
  std_{j-1} = standard deviation for region contains the last $r_s - (j-1) + 1$ rows
  $std_{diff_2}(j) = std_{j-1} - std_j$
EndFor

$std_{diff_2}(r_2) = max(std_{diff_2})$

Repeat for c_1, and c_2

Figure 3.3: Algorithm 1 to define a rectangle surrounding the FOV.

The proposed method is summarised as follows:

1. Determine the rectangle that surrounds the FOV.

2. Initialise a queue of seed pixels (by using all pixels outside the surrounding rectangle or use a margin of T_{mar} pixels).

3. For pixel i in the queue $I(r_i, c_i)$; define a region $\Re$ of N pixels, $N = T_{block-size}$, centered at (r_i, c_i).

4. Find mean, N_{mean}, and standard deviation, N_{std}, values for the pixels in the neighbourhood of $I(r_i, c_i)$ as:

$$N_{mean} = \frac{1}{N} \sum_{r,c \in \Re} I(r, c)$$

$$N_{std} = \sqrt{\frac{1}{N-1}\sum_{r,c\in\Re}(I(r,c)-N_{mean})^2}$$

If ($N_{mean} < T_{mean}$ and $N_{std} < T_{std}$)

- add pixels of N to the background region.

5. Calculate C (the number of new added pixels to the background region)

   If $C > 0$

   - update the queue (all new added pixels to the background region).
   - repeat steps 3, 4, and 5.

   Else

   - HALT

3.2.3 Experimental results

The method described in Section 3.2.2 was used to generate the binary mask for 60 images from two datasets [42, 43]. For each image in the STARE dataset, a binary mask was generated manually by using different threshold values and finding the best threshold value that produces the best binary mask. These manually generated masks were used as the GT for performance evaluation. For each image in the DRIVE dataset, a mask image was provided that delineates the FOV which will be used as the GT. Each one of these 60 images was processed using the parameters $T_{mean} = 40$, $T_{std} = 2$, $T_{block-size} = 3\times3$, and $T_{mar} = 5$. These values were selected after some exploratory experiments. The effect of changing these parameters on the performance of the proposed method is also investigated.

3.2.3.1 STARE dataset

Results for mask generation using the STARE dataset images are reported in this section, Figure 3.4 shows the rectangle that surrounds the FOV for one image and its binary mask. Average true and false positive rate values when using different values for $T_{block-size}$ and

Table 3.1: STARE dataset results

$T_{block-size}$	T_{std}	FPR %	TPR %
3 × 3	1	26.8	100
3 × 3	2	**3.41**	**99.99**
3 × 3	3	2.67	99.99
3 × 3	4	2.36	99.99
3 × 3	5	2.16	99.99
5 × 5	1	38.06	100
5 × 5	2	4.52	99.99
5 × 5	3	2.90	99.99
5 × 5	4	2.35	99.99
5 × 5	5	2.07	99.98
7 × 7	1	42.84	100
7 × 7	2	5.88	99.99
7 × 7	3	3.94	99.99
7 × 7	4	3.21	99.98
7 × 7	5	2.75	99.97

T_{std} are summarised in Table 3.1. For all images in the STARE dataset, when using the predefined values for the parameters, average TPR and FPR of 100% and 3.4% respectively are achieved. Out of 20 images, 17 images give TPR of 100% with mean FPR of 2.72%, and one image gives TPR of 99.96% with FPR of 19.7%. For this particular image, the black background region surrounds the FOV can be considered as two regions which results in high FP, also it is characterised with high mean and standard deviation values. The result is enhanced to TPR of 99.6% and FPR of 1.5% when increasing the parameters T_{mean} to 70, T_{std} to 25, use $T_{mar} = 0$ (because this image is tangential to one of the image borders), and keep $T_{block-size} = 3 \times 3$.

3.2.3.2 DRIVE dataset

For the DRIVE dataset images, Figure 3.5 shows a rectangle surrounds the FOV for one image and its binary mask. Average true and false positive rate values when using different values for $T_{block-size}$ and T_{std} are summarised in Table 3.2. Out of 40 images, 39 images give TPR of 100% with mean FPR of 2.88%, and one image gives TPR of 99.99% with FPR of 5.56%, which result in average TPR and FPR of 100% and 2.95% respectively.

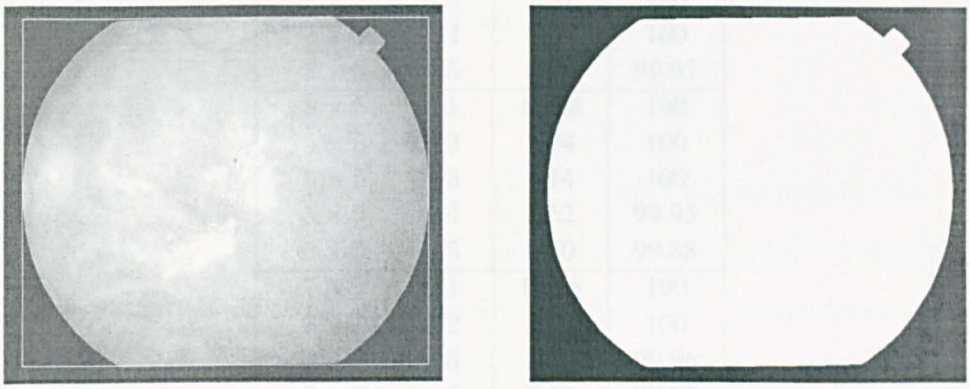

(a) (b)

Figure 3.4: An image from the STARE dataset with: (a) rectangle surrounding the FOV, and (b) binary mask.

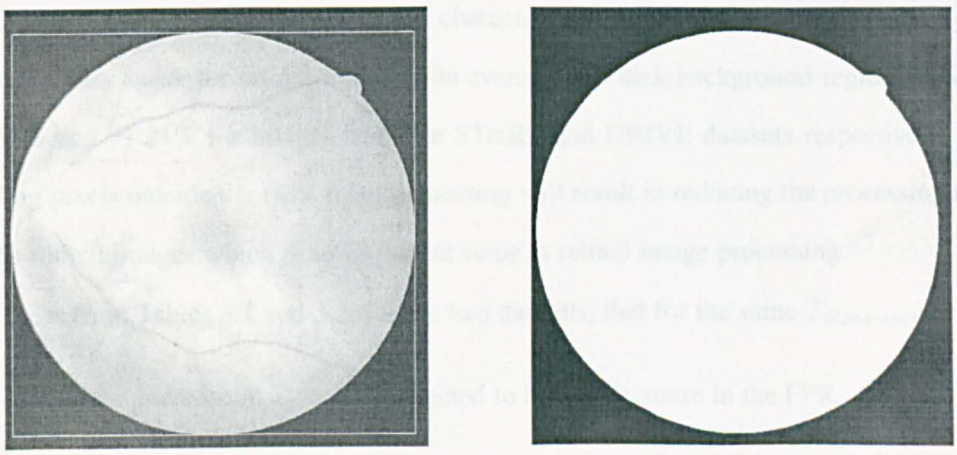

(a) (b)

Figure 3.5: An image from the DRIVE dataset with: (a) rectangle surrounding the FOV, and (b) binary mask.

Table 3.2: DRIVE dataset results

$T_{block-size}$	T_{std}	FPR %	TPR %
3×3	1	10.14	100
3×3	2	**2.95**	**100**
3×3	3	1.51	100
3×3	4	0.80	100
3×3	5	0.59	99.97
5×5	1	12.08	100
5×5	2	2.74	100
5×5	3	1.14	100
5×5	4	0.62	99.95
5×5	5	0.50	99.88
7×7	1	13.15	100
7×7	2	2.30	100
7×7	3	0.80	99.96
7×7	4	0.54	99.87
7×7	5	0.46	99.80

3.2.4 Discussion

The red channel of colour fundus images has the advantage of being brighter than the green channel, which results in having the highest contrast between the FOV and the black surrounding background. Because of this characteristic feature, this channel is used to generate a binary mask for retinal images. On average, the dark background region occupies 26.67% and 31.21% for images from the STARE and DRIVE datasets respectively. Excluding pixels outside the FOV from processing will result in reducing the processing time of the retinal images which is an important issue in retinal image processing.

It is clear from Tables 3.1 and 3.2, for the two datasets, that for the same $T_{block-size}$:

- With the increase in T_{std}, it is expected to have a decrease in the FPR.
- There is a large gap in the FPR values achieved between $T_{std} = 1$ and $T_{std} = 2$, while this gap decreased with increasing T_{std}, which indicates that the optimum choice for the parameter T_{std} is 2.

Given that the above two observations are valid for both datasets, this consistency of observation augers well for the proposed method. Figures 3.6 and 3.7 demonstrate the robustness of the proposed method and how it gives high performance for a wide range of the

$T_{block-size}$ and T_{std} parameters. The two Figures (3.6 and 3.7) are plotted at $T_{mar} = 5$ and $T_{mean} = 40$.

3.3 Enhancement of Colour Fundus Images

3.3.1 Introduction

Unsupervised methods for segmenting blood vessels from colour fundus images use the green channel [12, 46, 63, 65, 66] because generally it has the highest contrast between blood vessels and the retinal background while the red channel is rather saturated and the blue channel is rather dark. Gray-level distributions of three (red, green, and blue) channels for a colour fundus image are shown in Figure 3.8. For the same reason, the green channel is used in supervised methods to detect image ridges [44] or to extract features [73] for pixels that will be classified as vessels or not. Experiments show that the red channel has the advantage of being brighter and distributed over a wider range of gray-level values, than the green channel, which results in less contrast between abnormalities and the retinal background.

In this section, a novel method of using the red channel gray-level distributions and a novel application of the histogram matching approach other than colour normalisation is proposed. The intensity information from red and green channels of the same retinal image are combined without using a reference image, as it is believed that each image has its own gray-level distributions according to the FOV, the location of optic disc, normality, or abnormality. Performances of automatic detection of retinal blood vessels using histogram matched images that result from the proposed method and using different reference images are compared. The red channel is used in pre-processing of colour fundus images for two reasons: firstly, to improve the visual appearance of retinal images in cases of non-uniform illumination. Secondly, to improve the performance of unsupervised methods of blood vessel segmentation, which will be a helpful step towards the automatic analysis of retinal images. As many methods are based on applying the two-dimensional matched filter [63] before segmenting the retinal blood vessels [12, 65, 66, 67], it is used here as an example

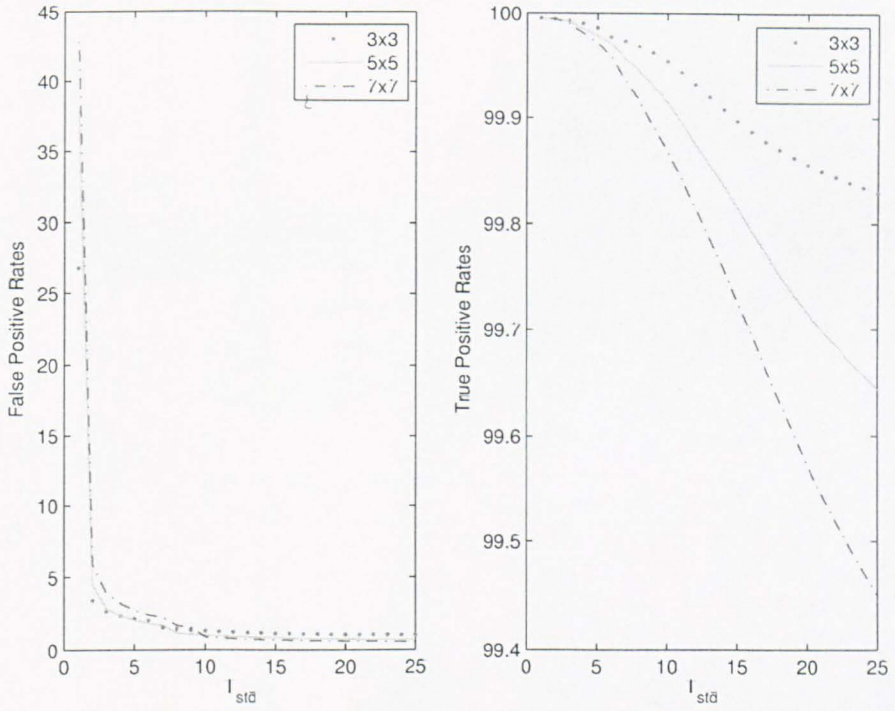

Figure 3.6: Performance at different T_{std} and $T_{block-size}$ values for STARE dataset images.

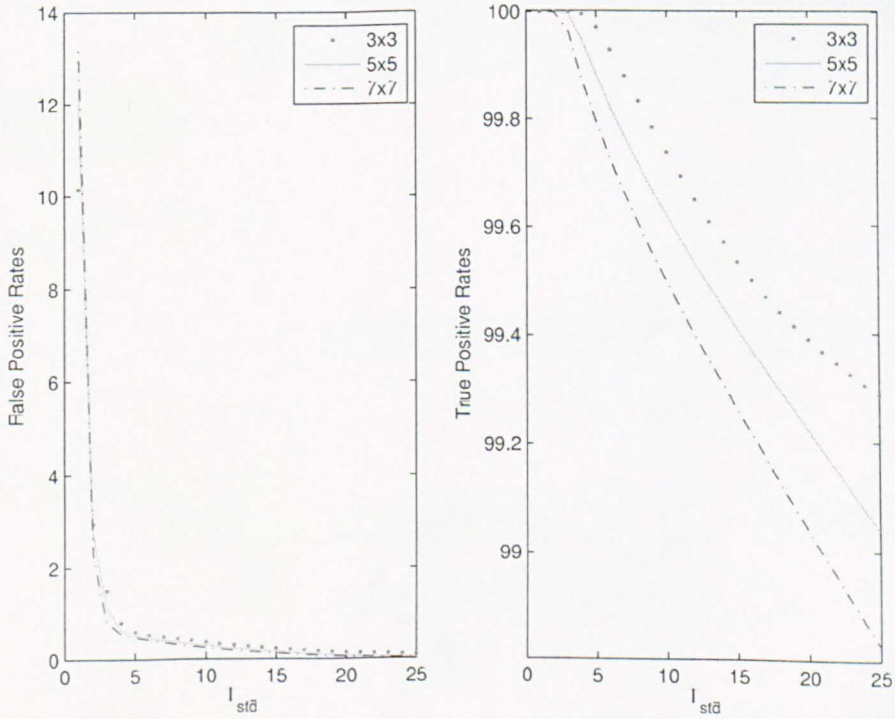

Figure 3.7: Performance at different T_{std} and $T_{block-size}$ values for DRIVE dataset images.

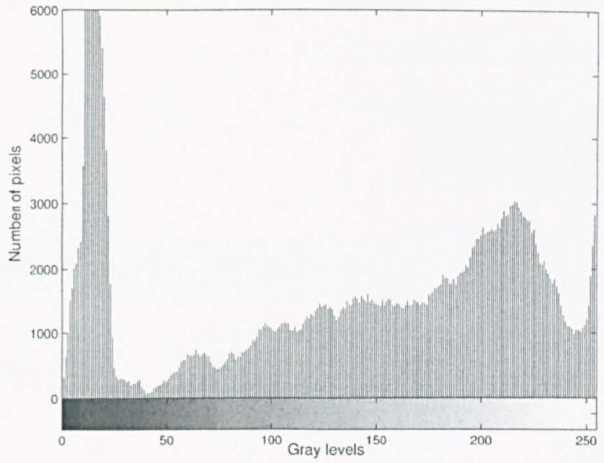

(a)

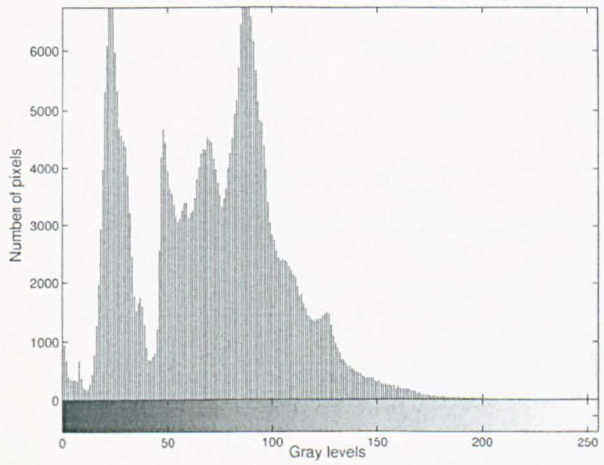

(b)

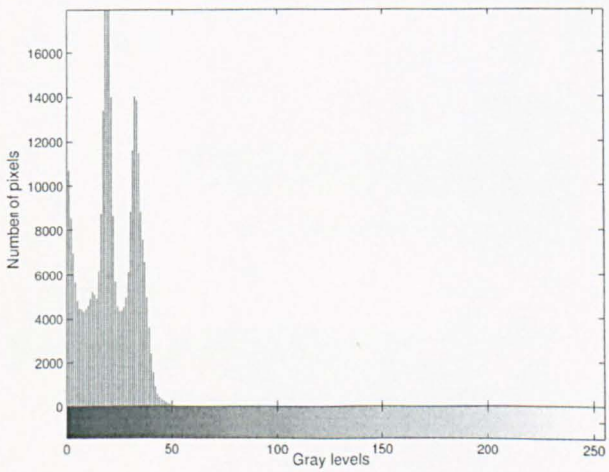

(c)

Figure 3.8: Gray-level distributions in (a) red channel, (b) green channel, and (c) blue channel of one fundus image.

of unsupervised methods and the effect of using red channel, green channel, and histogram matched image (HMI) on the efficiency of blood vessel detection are investigated. Results are compared with the piece-wise threshold probing method [12].

3.3.2 Histogram matching

Histogram matching is an approach that is used to generate a processed image that has a specified histogram [45], it has the advantage of producing more realistic looking images than those generated by equalisation. Histogram matching was proven to be a good normalisation method for making colour images invariant with respect to background pigmentation variation between individuals. By selecting a particular retinal image as a reference image and using histogram matching to modify the three channels of each colour image, the problem of wide variations in colour of the fundus from different patients is solved in [27] while clustering results of different lesion types are improved in [80]. Histogram matching is also used in visual image quality assessment [81], where model histograms for pixel and edge value distributions are used. These models were defined using a set of good quality images.

In the proposed method, the concept of histogram matching is used to modify the histogram of the green channel image to match that of the red channel image in order to combine the distributions of gray-levels in both images [83]. The procedures are summarised as follows:

1. Obtain histograms of both images (green and red channels),

2. Perform a mapping from the levels in the green channel image g_k into corresponding levels s_k based on its histogram

$$s_k = T(g_k) = \sum_{j=0}^{k} P_g(g_j)$$

$$= \sum_{j=0}^{k} \frac{n_j}{n} \qquad k = 0, 1, 2, ..., (L-1) \tag{3.1}$$

where $P_g(g)$ is the PDF for the green channel image, n is the total number of pixels in the image, n_j is the number of pixels with gray-level g_j, and L is the number of discrete gray-levels,

3. From $P_r(r)$, the histogram of the red channel image, obtain a transformation function G such that:

$$G(r_k) = \sum_{j=0}^{k} P_r(r_j) = s_k \qquad k = 0, 1, 2, ..., (L-1) \tag{3.2}$$

4. By using the inverse transform,

$$r_k = G^{-1}[T(g_k)] \qquad k = 0, 1, 2, ..., (L-1) \tag{3.3}$$

or

$$r_k = G^{-1}(s_k) \qquad k = 0, 1, 2, ..., (L-1) \tag{3.4}$$

theoretically, we are seeking values of r that satisfy Equation 3.4,

5. Practically, for each gray-level g_k, map this value to its corresponding level s_k; then map level s_k into the final level r_k. This is shown in Figure 3.9.

3.3.3 Saturation condition

Figure 3.10 shows results of applying the proposed method in cases of saturated images (the histogram of the red channel in used to modify the histogram of the green channel to obtain the histogram matched image which is shown in Figure 3.10 (d)). As the red channel image is very bright, then combining information from both channels results in a a histogram matched image (HMI) with contrast much lower than the contrast in the green channel image. In these cases (of saturated images), the use of green channel images is preferred over the use of histogram matched images. For this reason, a criterion to test the saturation of the red channel image of the test image is necessary to establish whether the green channel image or the histogram matched image should be used.

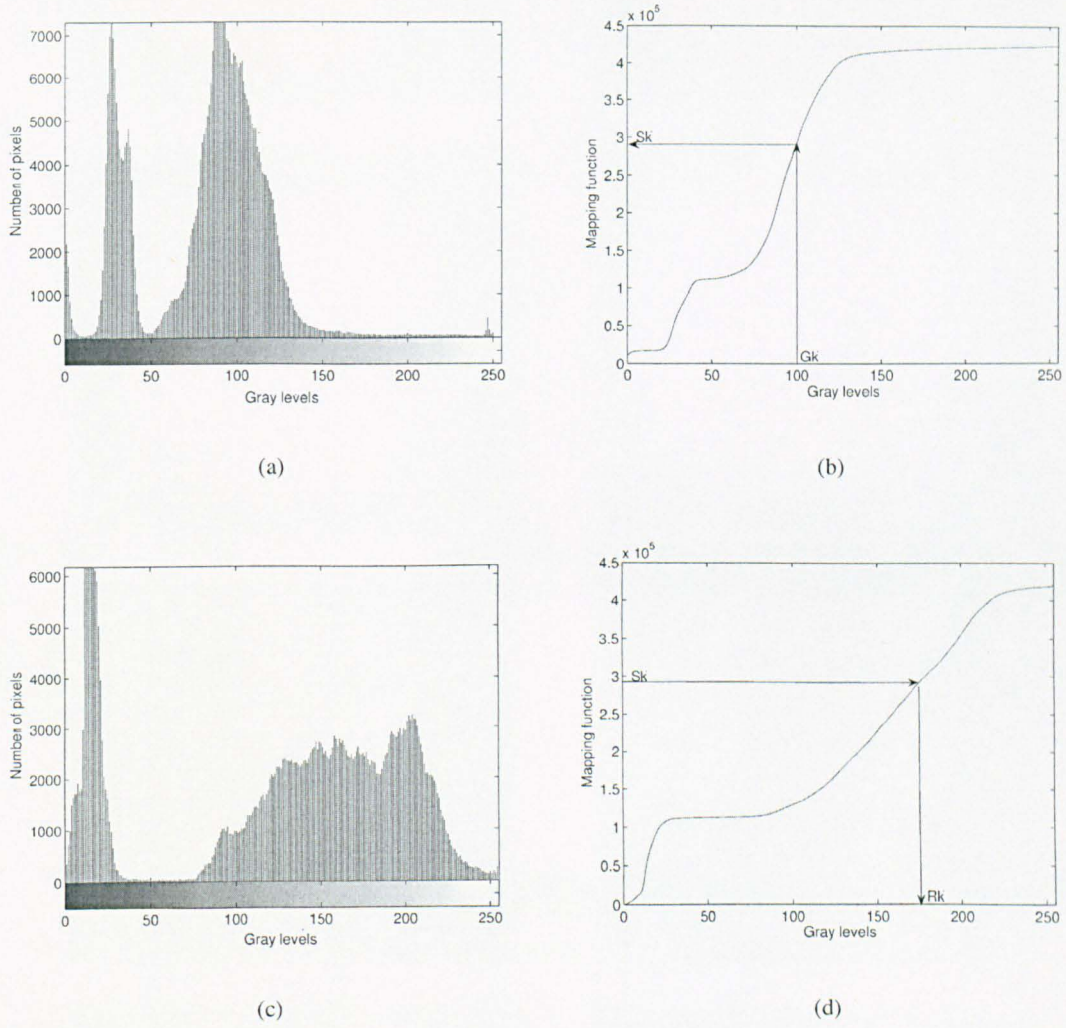

Figure 3.9: (a) Histogram of the green channel image, (b) its mapping function, (c) histogram of the red channel image, and (d) its mapping function.

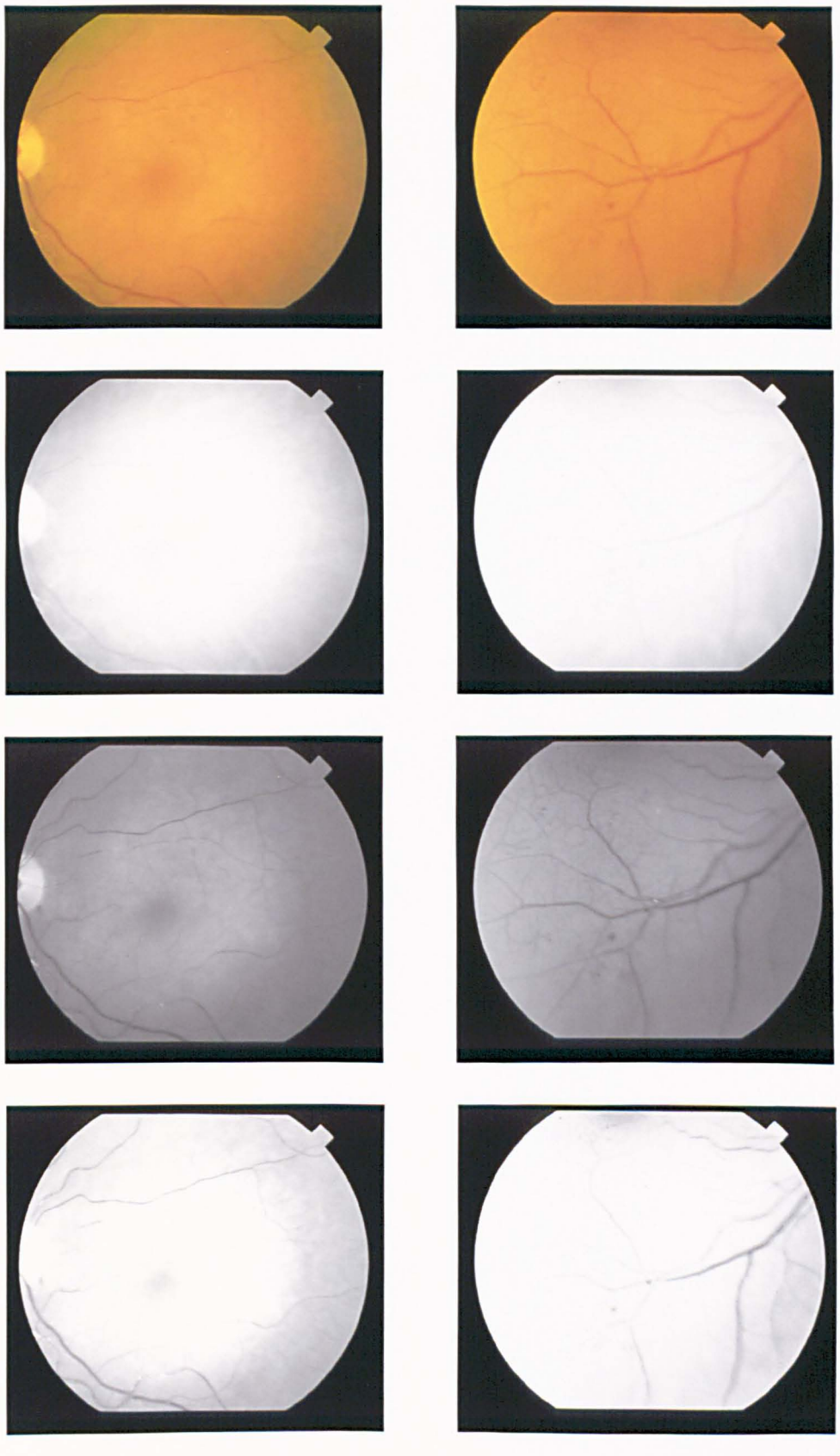

Figure 3.10: Two examples of saturated images and their (a) RGB, (b) red channel, (c) green channel, and (d) histogram matched image.

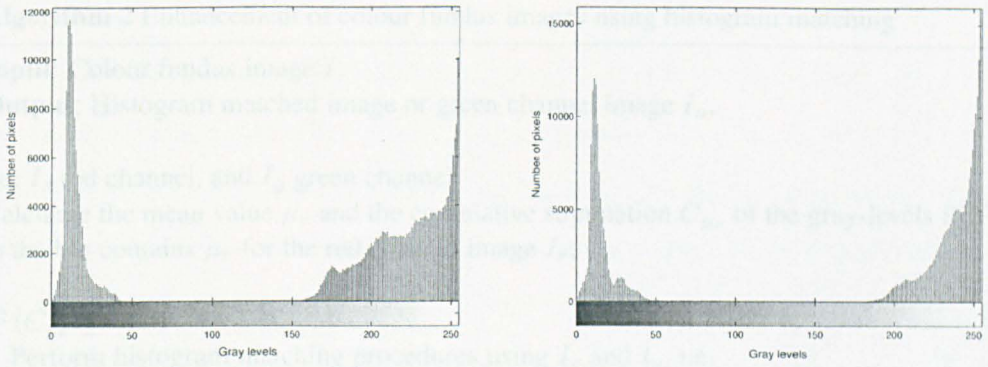

Figure 3.11: Histogram of red channels of saturated images in Figure 3.10.

It has been observed that the histogram of very bright images is characterised by a large gap in the gray-level distributions, (see Figure 3.11). There are many ways to detect this characteristic. Having experimented with different criteria, a computationally simple yet an effective criterion is as follows: calculate the cumulative summation of the gray-levels PDF in the red channel up to the mean value:

$$\mu_r = \sum_{j=0}^{L-1} r_j \cdot P_r(r_j) \tag{3.5}$$

$$C_k = \sum_{j=0}^{k} P_r(r_j) \tag{3.6}$$

where $P_r(r)$ is the PDF for the red channel image, k is the bin containing the mean value, μ_r, and L is the number of discrete gray-levels. The condition which used to test the saturation of a test image is:

$$C_{\mu_r} \geq 0.3$$

This value has been determined experimentally. The proposed method is presented in Figure 3.12.

Algorithm 2 Enhancement of colour fundus images using histogram matching

Input: Colour fundus image I.
Output: Histogram matched image or green channel image I_o.

Let I_r red channel, and I_g green channel.
Calculate the mean value μ_r and the cumulative summation C_{μ_r} of the gray-levels PDF up to the bin contains μ_r for the red channel image I_r.

IF ($C_{\mu_r} \geq 0.3$)
  Perform histogram matching procedures using I_r and I_g, i.e.
  $I_o = hist\_match\ (I_r, I_g)$
Else
  $I_o = I_g$
EndIF

Figure 3.12: Algorithm 2 enhancement of colour fundus images using histogram matching.

3.3.4 Experiments

The improvement in visual appearance of a retinal image as a whole will be investigated by processing the histogram of the green channel in conjunction with the histogram of the red channel as described earlier. Then, to test the effect of this enhancement on the appearance of blood vessels, the algorithm in [63] is implemented to test the ability of the two-dimensional matched filter to segment blood vessels from retinal images. The red channel, green channel, and the histogram matched images are used to obtain the MFR images for every test image in the dataset.

For the purposes of comparison, three normal images (from the dataset) are selected as reference images, where the green channel histograms of these images are used as reference model histograms. The histogram matching is used to modify the green channel of test images using these reference histograms.

To evaluate the performance of the proposed method, a set of 20 images publicly available [42] is used and the performance is measured with ROC curves.

3.3.5 Results and Discussion

For efficient segmentation of retinal blood vessels, it is desirable to have high contrast between the retinal blood vessels and retinal background whilst there should be low contrast between retinal background and retinal abnormalities. Combining the advantages of both channels, brightness in red channel and high contrast in green channel, results in decreasing the contrast between the abnormalities and the retinal background. This helps to reduce some responses, which do not resemble any blood vessels and which would otherwise decrease the performance of blood vessel segmentation methods.

The first application of the proposed method is to correct the non-uniform illumination, which is a common problem, in retinal images. Figure 3.13 shows results of matching the green channel histogram with the red channel histogram for two test images. The HMI is now a combination of the green channel image (which is less bright but with higher contrast) and the red channel image (which is more uniformly illuminated).

The second application is to improve the performance of unsupervised blood vessel detection methods. The retinal blood vessels are segmented using the method in [63], where the red channel, green channel, the histogram matched images are used. Two types of histogram matched images are used; the result of combining red and green histograms as well as the result of combining the green channel with three different reference histograms as shown in Figure 3.14, ROC curves for these images are plotted in Figure 3.15.

Figures 3.13, 3.14 and 3.15 show that the proposed combination of gray-level distributions from red and green channels is a useful pre-processing step in cases of non-uniform illumination and in improving the performance of blood vessel segmentation.

Average ROC curves for all twenty (normal and abnormal) images were considered for sensitivity and specificity analysis at some specified points and results are summarised in Table 3.3. It is clear from Table 3.3 that the red channel (MFR_r) has the least sensitivity while the reference 3 (MFR_{r3}) offers the next least sensitivity followed by the green channel. The reference 1 (MFR_{r1}) and reference 2 (MFR_{r2}) are similar to each other and offer better sensitivity. The best sensitivity is achieved by the proposed HMI (MFR_{hm}) where

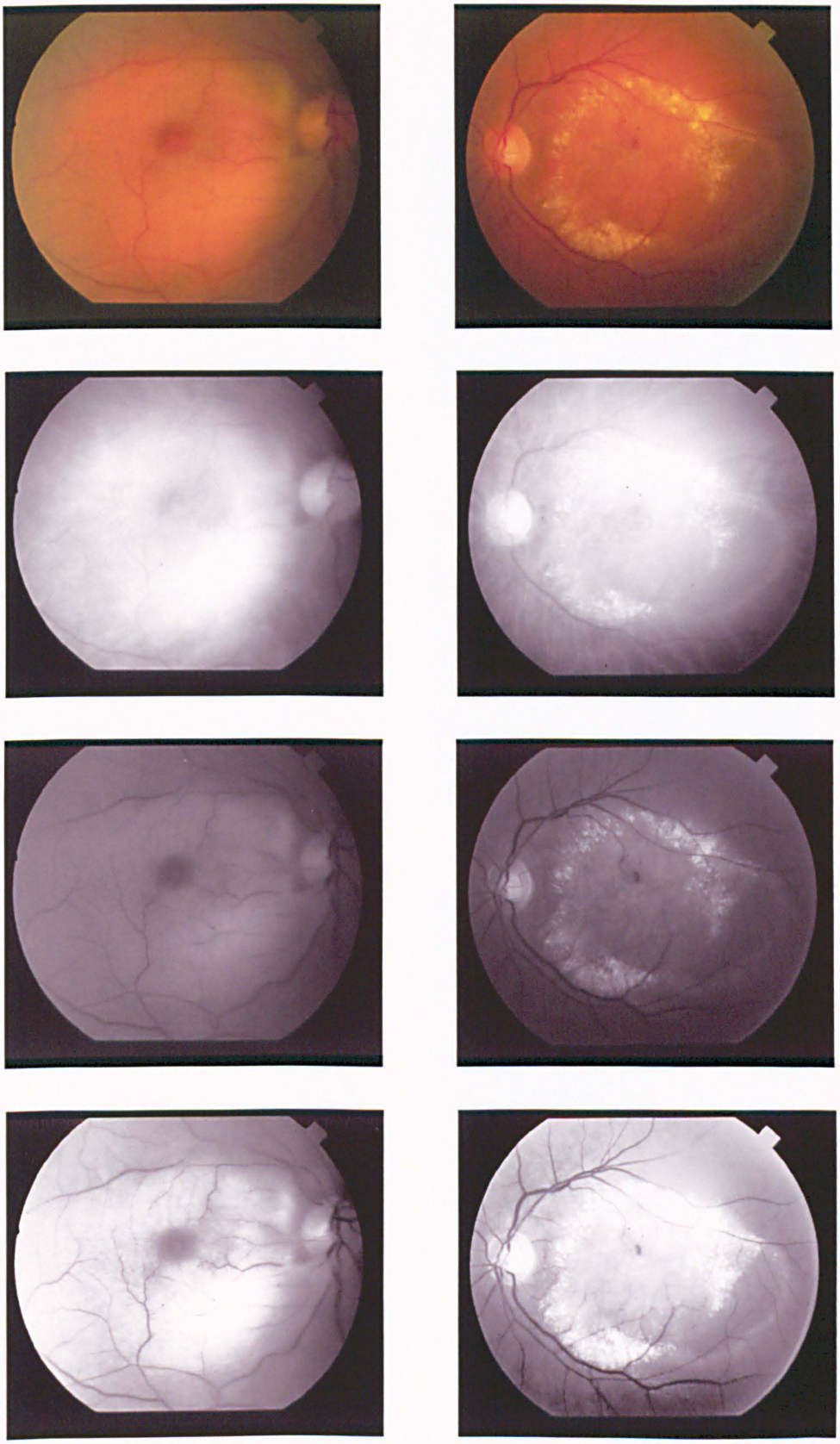

Figure 3.13: Application of the proposed method for non-uniform illumination (a) RGB images, (b) red channel, (c) green channel, and (d) HM images.

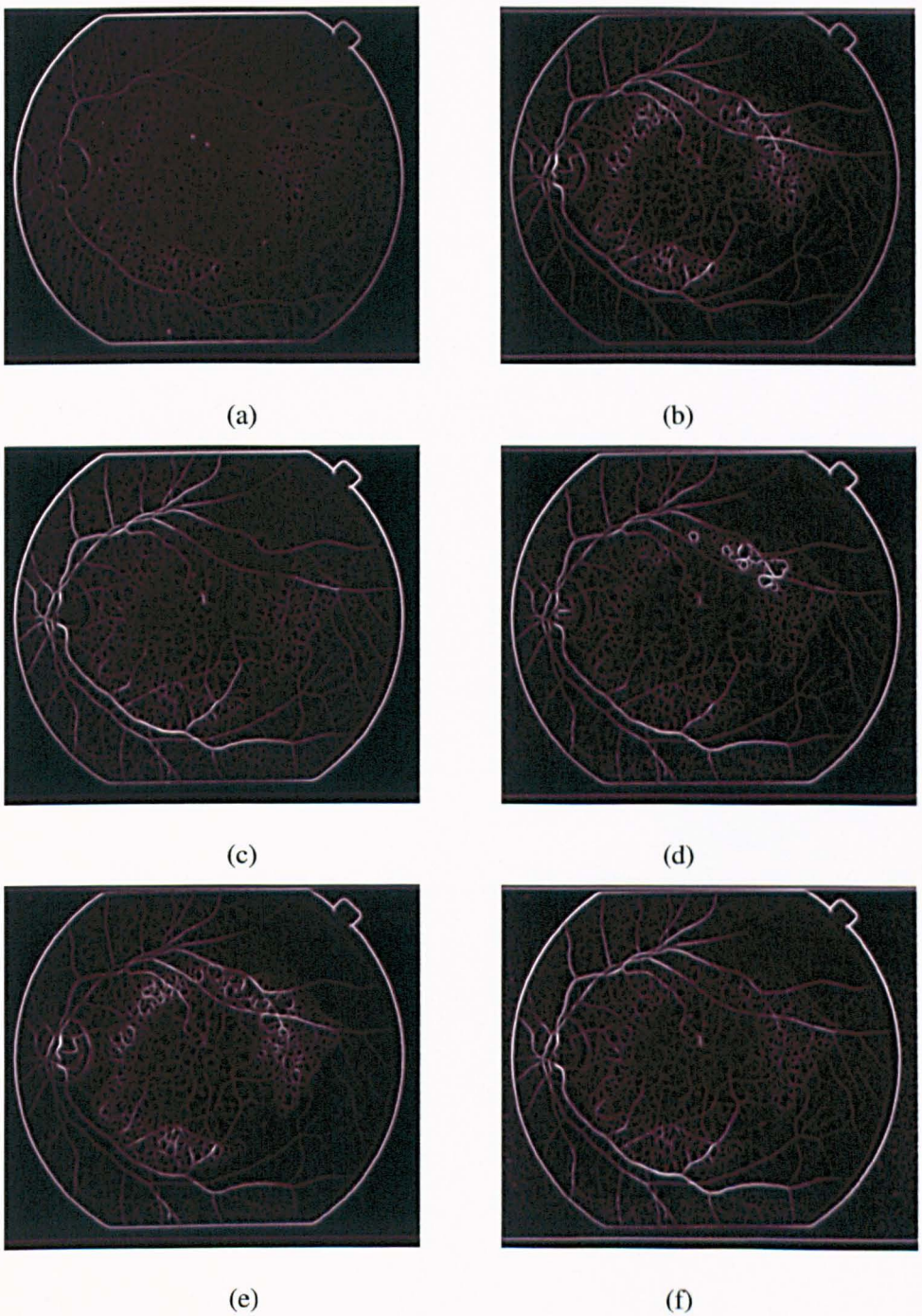

Figure 3.14: MFR images using (a) red channel, (b) green channel, and HMI when (c) combining red and green, (d, e, f) using three different reference models.

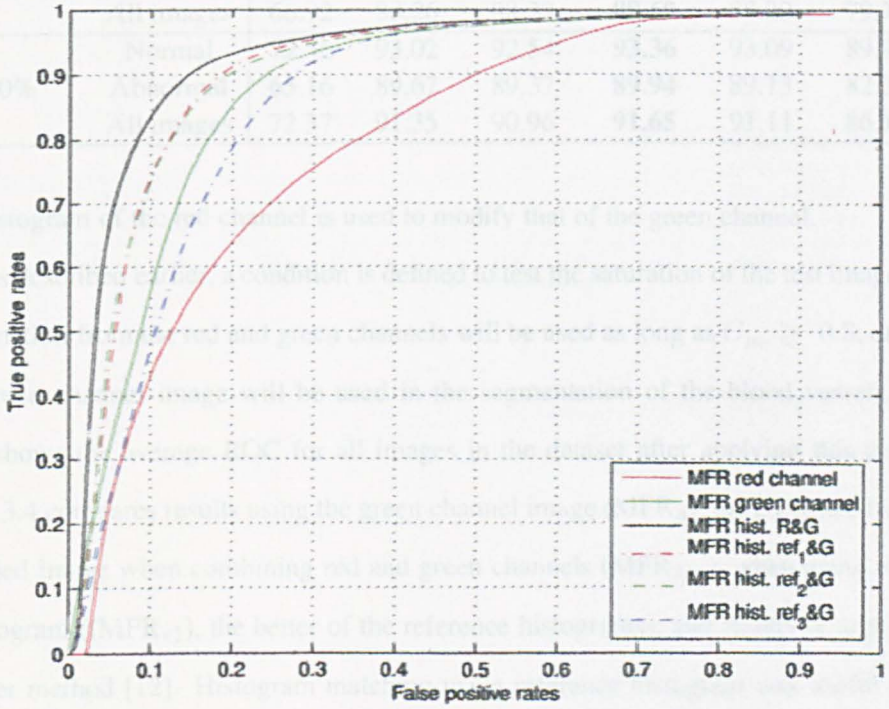

Figure 3.15: ROC curves for images in Figure 3.14.

Table 3.3: Sensitivity and specificity values for MFR images (using red, green, HMI, and 3 normal reference images)

Specificity %	Image type	Sensitivity %					
		MFR_r	MFR_g	MFR_{hm}	MFR_{r1}	MFR_{r2}	MFR_{r3}
95%	Normal	53.16	71.38	**73.45**	72.42	72.58	58.82
	Abnormal	28.56	50.45	**60.83**	57.24	58.19	36.17
	All images	40.86	60.92	**67.14**	64.83	65.38	47.50
90%	Normal	69.54	87.05	86.66	**87.09**	86.91	77.39
	Abnormal	48.15	76.46	**79.83**	78.40	78.15	59.85
	All images	58.85	81.75	**83.41**	82.74	82.53	68.62
85%	Normal	75.64	91.08	90.67	**91.37**	91.11	85.49
	Abnormal	58.21	85.44	**86.08**	86.00	85.29	74.00
	All images	66.92	88.26	88.37	**88.69**	88.20	79.74
80%	Normal	72.56	93.02	92.54	**93.36**	93.09	89.98
	Abnormal	65.16	89.67	89.37	**89.94**	89.13	82.29
	All images	72.37	91.35	90.96	**91.65**	91.11	86.14

the histogram of the red channel is used to modify that of the green channel.

As described earlier, a condition is defined to test the saturation of the test image, so the information from the red and green channels will be used as long as $C_{\mu_r} \geq 0.3$, otherwise the green channel image will be used in the segmentation of the blood vessels, Figure 3.16 shows the average ROC for all images in the dataset after applying this condition. Table 3.4 compares results using the green channel image (MFR_g), the proposed histogram matched image when combining red and green channels (MFR_{hm}), when using reference 1 histogram ((MFR_{r1}), the better of the reference histograms), and results of applying the Hoover method [12]. Histogram matching using reference histogram was useful in cases of normal images and very bright abnormal images; also results are affected by different choices of the reference histograms (as seen in Table 3.3) which required an expert to select a suitable reference histogram. On the other hand, histogram matching using red and green histograms of the same image was useful in most of the abnormal images, and to overcome the problem caused by very bright images (normal or abnormal), a saturation condition is set which improved the performance (as in Table 3.4).

To evaluate the performance of the proposed method, results are compared with results of Hoover *et al.* [12] which require more post-processing. Results show that the use of

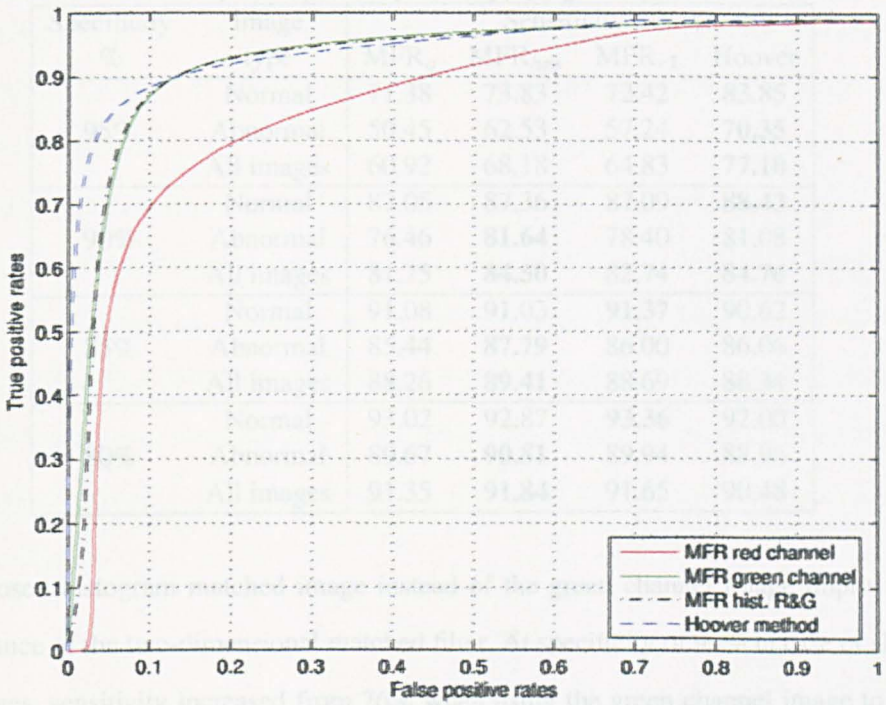

(a)

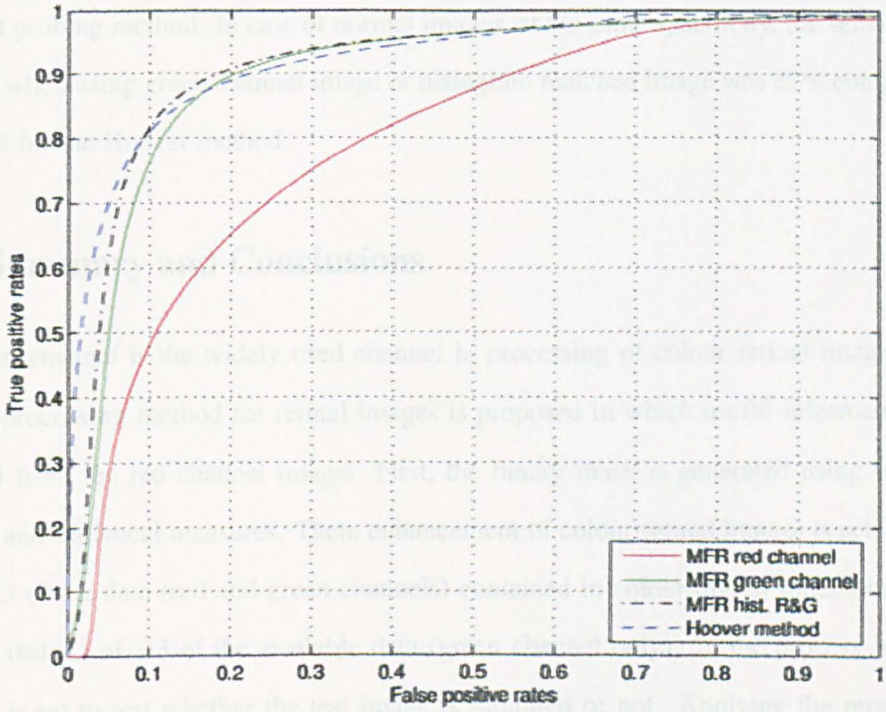

(b)

Figure 3.16: Average ROC curves (after testing image saturation) for (a) normal, and (b) abnormal images.

Table 3.4: Sensitivity and specificity after applying the saturation condition

Specificity %	Image type	Sensitivity %			
		MFR_g	MFR_{hm}	MFR_{rl}	Hoover
95%	Normal	71.38	73.83	72.42	**83.85**
	Abnormal	50.45	62.53	57.24	**70.35**
	All images	60.92	68.18	64.83	**77.10**
90%	Normal	87.05	87.36	87.09	**88.43**
	Abnormal	76.46	**81.64**	78.40	81.08
	All images	81.75	**84.50**	82.74	**84.76**
85%	Normal	91.08	91.03	**91.37**	90.62
	Abnormal	85.44	**87.79**	86.00	86.06
	All images	88.26	**89.41**	88.69	88.34
80%	Normal	93.02	92.87	**93.36**	92.00
	Abnormal	89.67	**90.81**	89.94	88.96
	All images	91.35	**91.84**	91.65	90.48

the proposed histogram matched image instead of the green channel image improve the performance of the two-dimensional matched filter. At specificity of 90% in case of abnormal images, sensitivity increased from 76% when using the green channel image to 82% when using the histogram matched image compared with 81% when using the piece-wise threshold probing method. In case of normal images, at the same specificity, the sensitivity obtained when using green channel image or histogram matched image was 87% compared with 88% for the Hoover method.

3.4 Summary and Conclusions

The green channel is the widely used channel in processing of colour retinal images. A new pre-processing method for retinal images is proposed in which useful information is extracted from the red channel image. First, the binary mask is generated using region growing and statistical measures. Then, enhancement of colour retinal images is achieved, where 2/3 of the data (red and green channels) contained in colour digital fundus images are used instead of 1/3 of the available data (green channel only). In the process, a new criterion is set to test whether the test image is saturated or not. Applying the proposed method, a visual enhancement for retinal images in cases of non-uniform illumination is achieved and the performance of the two-dimensional matched filter is improved. This

method can be used to pre-process retinal images before applying unsupervised blood vessel segmentation methods as it results in decreasing the contrast between the abnormalities and the retinal background, and therefore can improve the performance of blood vessel segmentation methods.

In supervised and semi-supervised methods which are investigated in the next chapter, image pixels are classified into vessel and non-vessel pixels, which is a pixel based classification. In these cases, the processing time depends on the total number of pixels to be processed. The dark black background region around the FOV, which contains no information, occupies more than 25% of the image. Consequently, using a binary mask to segment the retinal FOV will avoid processing this region and this will results in reducing the processing time.

Chapter 4

Vessel Segmentation using Scale-Space Features

4.1 Introduction

IN this chapter, a feature vector of three features is proposed to be used in conjunction with supervised and semi-supervised classification of pixels in retinal images. Using this feature vector results in a significant reduction in the processing time required for the K-nearest neighbour (KNN) classifier compared with the feature vector proposed in [73]. Classification and clustering methods share the same concept of generating a feature vector for each image pixel, then classify or cluster pixels that are similar or share similar features to belong to the same class or cluster. The proposed feature vector consists of the green channel image intensity, the local maximum of the gradient magnitude, and the local maximum of the large eigenvalue of the Hessian matrix (both over scales). Then, three different vessel segmentation methods - supervised, unsupervised, and semi-supervised are investigated. These methods start by generating a feature vector for each pixel in the retinal image, then a classifier or a clustering algorithm is applied. In cases where GT images are available, the use of supervised methods is recommended. But when these GT are not available, then unsupervised methods are the most suitable ones. In other cases where the GT images are available but incomplete or for part of the image only, a semi-supervised

method can be used to take advantage of the percentage of the available GT. The *KNN* classifier is used as an example of supervised classification methods, while the nearest neighbour clustering algorithm (*NNCA*) is used as an example of unsupervised methods. As a semi-supervised method, a radius based Clustering Algorithm (*RACAL*) is used to segment retinal blood vessel pixels using a fraction of the available GT pixels for each image in the dataset. In Section 4.5.3.2, a modification is proposed to *RACAL*, to use it as a classifier which results in an improvement in segmentation results.

4.2 Feature Extraction

The two characterising attributes of any vessel, i.e. piecewise linearity and parallel edges [1], are considered when choosing the set of features for every pixel in retinal images. The piecewise linear property of a blood vessel can be recognised by extracting centrelines of blood vessels, simply by extracting the image ridges. The parallel edges property is well recognised by calculating the gradient magnitude of the image intensity. Because vessels are of different diameters, so these features are extracted at different scales and then the local maxima over all scales is calculated for both features. In addition to the property that the blood vessel can be seen in the colour retinal image as a dark object on a brighter background, from the three colour channels (red, green and blue) the green channel is chosen to represent this characteristic as it has the highest contrast between the blood vessel and the retinal background.

Scale-space features such as the gradient magnitude of the image intensity and the ridge strength, at different scales are proposed in [74]. Also, the first and second order derivatives of the green channel in x- and y- directions [73] or with respect to other image coordinates at different scales are used as features for every pixel in the retinal images [44]. In [73] a set of 31 feature are generated for each pixel in the retinal image, these 31 features are the green channel image intensity as well as the filtered image using the Gaussian and its derivatives in $x-$ and $y-$ directions up to order 2 at scales $s = 1, 2, 4, 8, 16$. In [52], a feature vector that consists of the pixel intensity and the maximum response of the two-

dimensional Gabor wavelet transform - at different orientations - for multiple scales was proposed.

In [84], the large eigenvalue of the Hessian matrix was proposed to be used as an indicator of the vessel centreline (the eigenvalues are sorted in an increasing order) which is different from the work done in [85, 86] (which sort the eigenvalues using the absolute values). As vessels are of different diameters, then different scales are used to calculate the eigenvalues and then keeping the maximum response at each image pixel over scales.

Figure 4.1 shows a sub-image with the intensity information for a blood vessel section plotted along with the gradient magnitude, the ridge strength and the largest eigenvalue. From the graphs, it is clear that the green channel has a higher contrast than the red channel image, gradient magnitude gives two peaks at the parallel edges of the blood vessels, and finally the large eigenvalue is better than the ridge strength in determining the centrelines of the blood vessels when processing colour fundus images. Figure 4.2 shows the three features; green, gradient magnitude, and the large eigenvalue for a sub-image.

4.2.1 Gradient magnitude

The gradient magnitude is calculated as:

$$|\nabla L| = \sqrt{L_x^2 + L_y^2}$$

where L_x and L_y are the first derivative of the intensity image $I(x, y)$ in $x-$ and $y-$ directions. Image derivatives can be taken by convolving the image with derivatives of Gaussian using the Gaussian scale-space techniques [87].

$$L_x = \frac{\partial L(\mathbf{x}, s)}{\partial x} = \frac{1}{2\pi s^2} \int_{\mathbf{x}' \in \mathbb{R}^2} \frac{\partial \mathrm{e}^{-\|\mathbf{x}-\mathbf{x}'\|^2/2s^2}}{\partial x} L(\mathbf{x}')\mathrm{d}\mathbf{x}' \tag{4.1}$$

where $L(\mathbf{x}, s) = I(\mathbf{x}) \otimes G(\mathbf{x}, s)$, $\mathbf{x} = (x, y)'$, and L_x is the image derivative with respect to $x-$ direction. Mixed and higher order derivatives are computed by taking mixed and higher order derivatives of the Gaussian kernel $G(\mathbf{x}, s)$. Calculations for image derivatives are given in Appendix B. First derivatives are calculated as [74]:

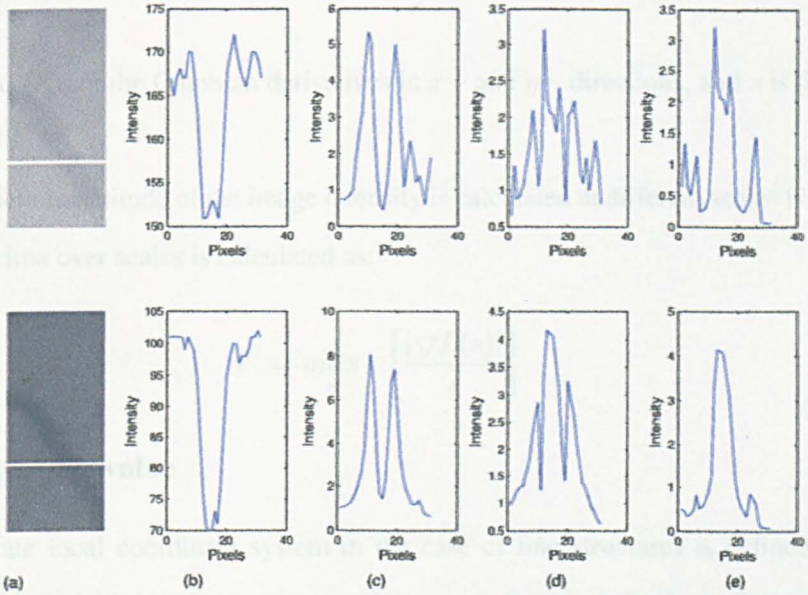

Figure 4.1: Sub-image with colour and scale-space features along a horizontal line crossing a blood vessel (a) sub-image, (b) intensity, (c) gradient magnitude, (d) ridge strength, and (e) large eigenvalue from a red channel image (top row) and a green channel image (bottom row).

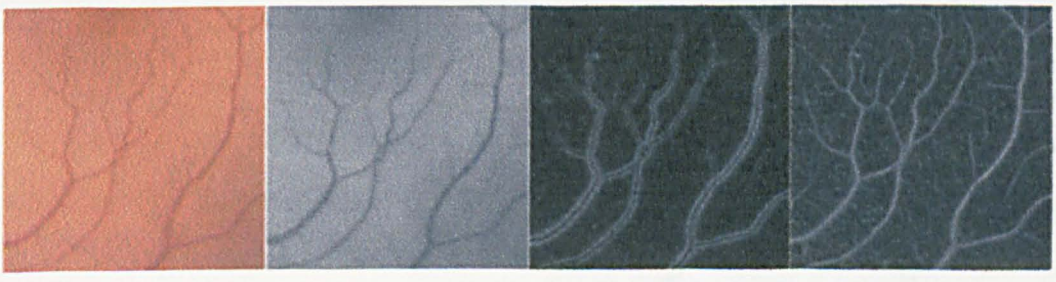

Figure 4.2: (a) RGB, (b) green channel, (c) gradient magnitude, and (d) large eigenvalue for a sub-image.

$$L_x = I(x, y) \otimes sG_x \tag{4.2}$$

$$L_y = I(x, y) \otimes sG_y \tag{4.3}$$

where G_x and G_y are the Gaussian derivatives in $x-$ and $y-$ directions, and s is the scale parameter.

The gradient magnitude of the image intensity is calculated at different scales [74], then the local maxima over scales is calculated as:

$$\gamma = \max_s \left[\frac{|\nabla L(s)|}{s}\right] \tag{4.4}$$

4.2.2 Large eigenvalue

The appropriate local coordinate system in the case of line structures is defined by the eigenvectors of the Hessian matrix, matrix of the second order derivatives of the intensity image $I(x, y)$. Eigenvalues (the large eigenvalue, λ_+, and the small eigenvalue, λ_-, where $\lambda_+ > \lambda_-$) of the Hessian matrix of the intensity image $I(x, y)$ are calculated in Appendix C.2:

$$\lambda_+ = \frac{L_{xx} + L_{yy} + \alpha}{2} \tag{4.5}$$

$$\lambda_- = \frac{L_{xx} + L_{yy} - \alpha}{2} \tag{4.6}$$

where L_{xx}, L_{yy} are the second derivatives of the intensity image in $x-$ and $y-$ directions, and $\alpha = \sqrt{(L_{xx} - L_{yy})^2 + 4L_{xy}^2}$. Then, the local maxima over scales is calculated as :

$$\lambda_{max} = \max_s \left[\frac{\lambda_+(s)}{s}\right] \tag{4.7}$$

In order to obtain dimensionless features, the normal transformation to the feature space [88] is used:

$$\widehat{f}_i = \frac{f_i - \mu_i}{\sigma_i} \tag{4.8}$$

where f_i is the ith feature assumed by each pixel, μ_i is the average value of the ith feature, and σ_i is the associated standard deviation. The normal transformation is applied separately to each feature space, i.e., every image's feature space is normalised by its own means and standard deviations, which help to compensate for intrinsic variation between images [52].

4.3 *K*-Nearest Neighbour Classifier

4.3.1 Introduction

The nearest neighbour classifier is one of the simplest and oldest methods for performing general, non-parametric classification [89]. To classify an unknown pixel x_q, choose the class of the nearest example in the training set as measured by a distance metric. A common extension is to choose the most common class in the K nearest neighbours. Let an arbitrary pixel x be described by the feature vector:

$$< a_1(x), a_2(x), ..., a_n(x) >$$

where $a_r(x)$ is used to denote values of the rth attribute of pixel x. Consider two pixels x_i and x_j, then the distance between these pixels is defined as $d(x_i, x_j)$ which is expressed in Equation 4.9:

$$d(x_i, x_j) \equiv \sqrt{\sum_{r=1}^{n} (a_r(x_i) - a_r(x_j))^2} \tag{4.9}$$

For hard classification, the *KNN* output is the most common value among K training examples nearest to x_q, while the mean value of the K nearest neighbour examples is calculated, instead of the most common value, for soft classification.

4.3.2 Experiments

For supervised classifiers, two sets of images are required; one for training and the other for testing. In our experiments - the STARE dataset is used - the dataset is randomly divided into two sets of images, each contains 5 normal and 5 abnormal images. The training set contains large number of training samples, which is the main problem with this type of classifier. To overcome such a problem, a random number of pixels is chosen from the FOV of each image in the training set. Targets for these training samples are available from the manually segmented images. The testing set contains 10 images to test the performance of the classifier. For every pixel in each retinal image in the dataset, a feature vector is generated, which contains three values - the pixel intensity from the green channel image, the local maxima of the gradient magnitude, and the local maxima of the large eigenvalue. Having experimented with different values of K, the value of $K = 60$ offered the best results; hence this value was chosen for the experiments.

4.3.3 Results and Discussion

Results

Figure 4.3 shows two examples, normal (left) and abnormal (right) images, after blood vessel segmentation using *KNN* classifier with the proposed set of features (green channel, and the maximum over scales for the gradient magnitude and the large eigenvalue) and the 31 features in [73] while the corresponding ROC curves are plotted in Figure 4.4. For the normal image, the two sets of features gives approximately the same results, but in case of abnormal image, the three features give higher sensitivity at the same specificity values. Table 4.1 summaries the hard classification results. Average ROC curves are considered for specificity and sensitivity analysis and the results for segmentation of retinal blood vessels is summarised in Table 4.2, where the average sensitivity is calculated at certain specificity values for normal and abnormal images in the testing set. The processing time is significantly decreased when using three features instead of 31 features.

Results obtained from the *KNN* classifier show that there is a need for a post-processing

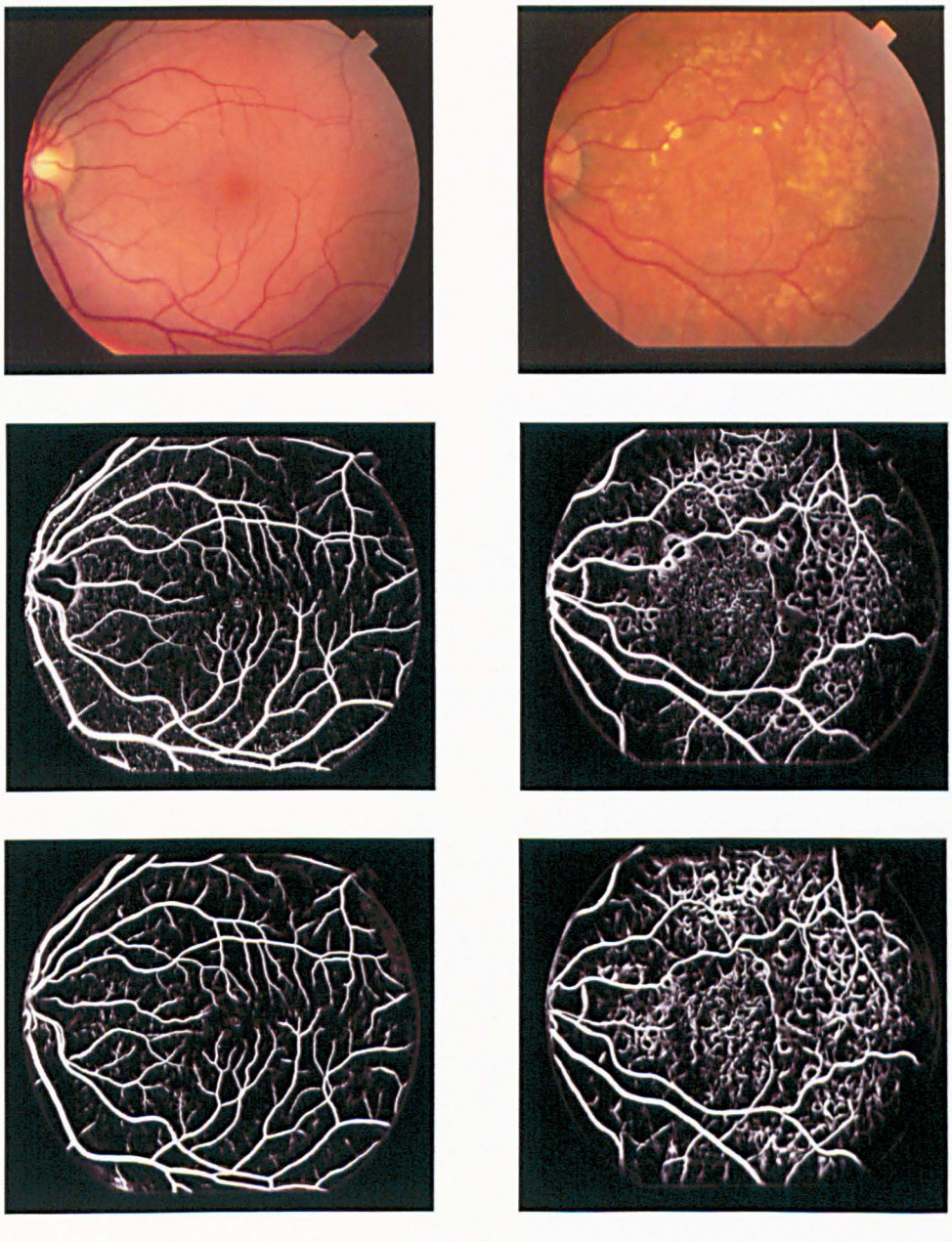

Figure 4.3: (a) RGB images, output of the *KNN* classifier using (b) 3 features, and (c) 31 features for normal (left) and abnormal (right) images.

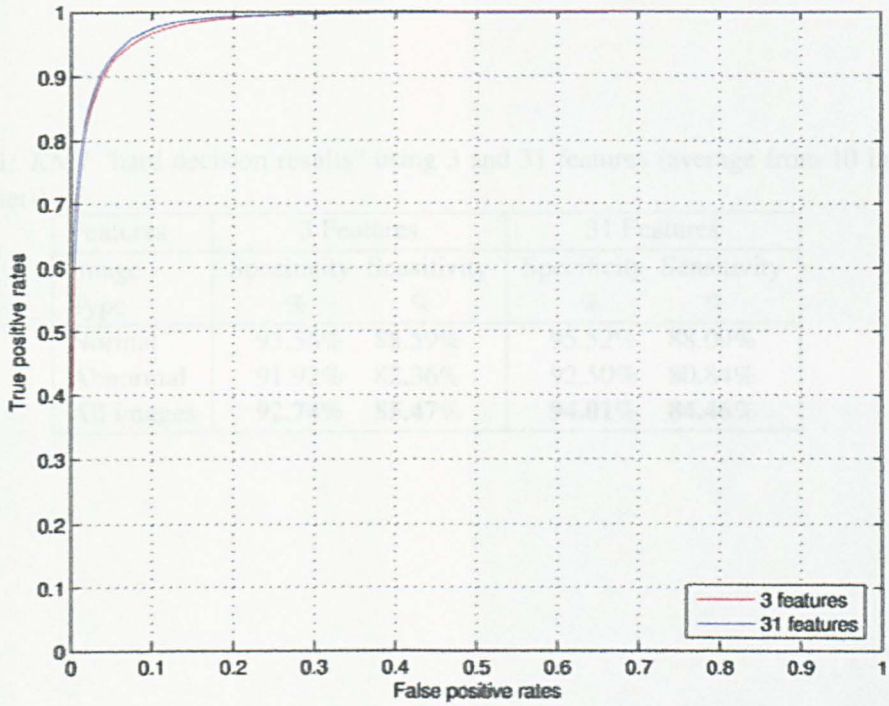

(a)

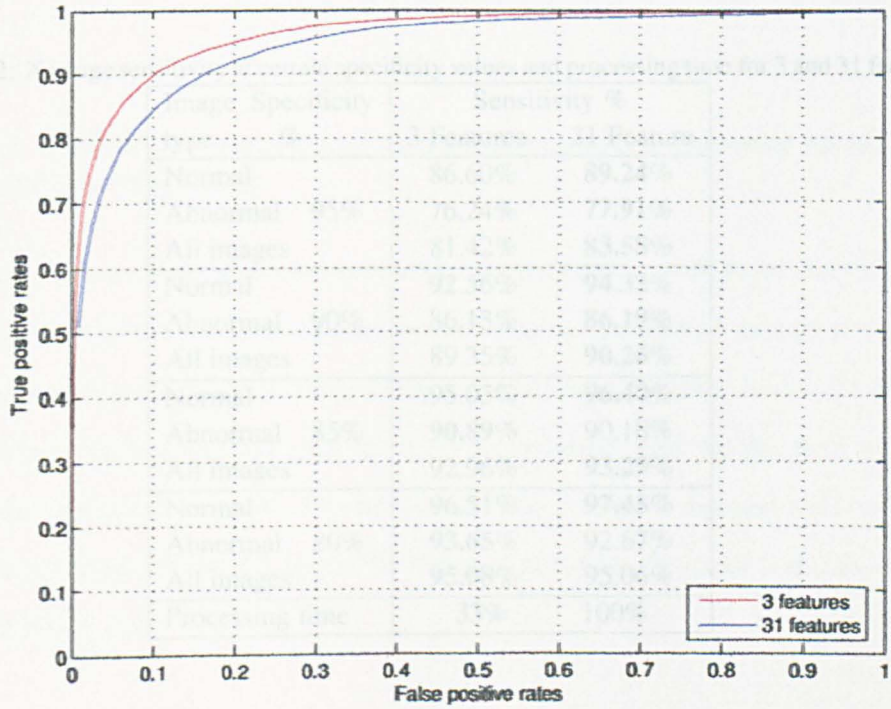

(b)

Figure 4.4: ROC curves for (a) normal, and (b) abnormal images in Figure 4.3.

Table 4.1: *KNN* "hard decision results" using 3 and 31 features (average from 10 images (testing set))

Features	3 Features		31 Features	
Image Type	Specificity %	Sensitivity %	Specificity %	Sensitivity %
Normal	93.56%	88.59%	95.52%	88.09%
Abnormal	91.92%	82.36%	92.50%	80.84%
All images	**92.74%**	**85.47%**	**94.01%**	**84.46%**

Table 4.2: Average sensitivity at certain specificity values and processing time for 3 and 31 features

Image type	Specificity %	Sensitivity % 3 Features	Sensitivity % 31 Feature
Normal		86.60%	**89.24%**
Abnormal	95%	76.24%	**77.91%**
All images		81.42%	**83.58%**
Normal		92.56%	**94.32%**
Abnormal	90%	86.13%	**86.19%**
All images		89.35%	**90.26%**
Normal		95.03%	**96.40%**
Abnormal	85%	**90.89%**	90.18%
All images		92.96%	**93.29%**
Normal		96.51%	**97.45%**
Abnormal	80%	**93.65%**	92.67%
All images		**95.08%**	95.06%
Processing time		**33%**	100%

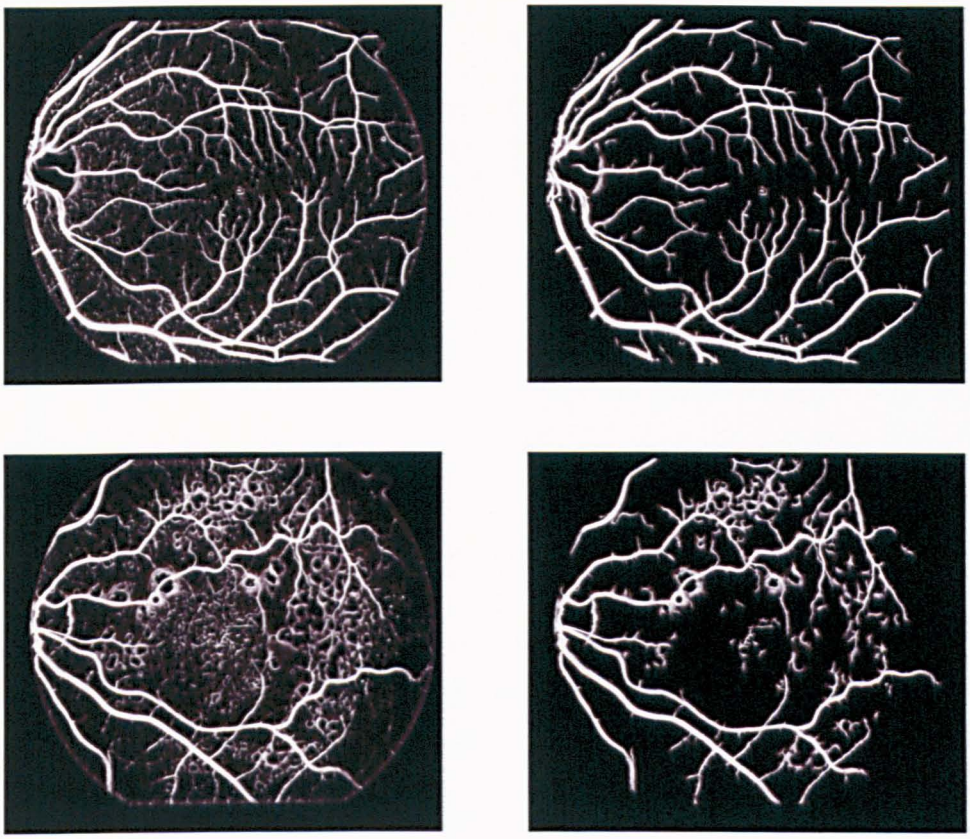

(a) (b)

Figure 4.5: Effect of post-processing (a) before, and (b) after post-processing normal (top) and abnormal (bottom) images.

step to remove some connected components that are not blood vessels in order to improve the performance of the classifier. In this step, an iterative thresholding strategy to remove small segments is applied. The processed image (output image from the classifier) is thresholded and segments of size less than 15 pixels are removed, then the threshold value is incremented and small segments are removed and this process is repeated until no more pixels are removed. Figure 4.5 shows the effect of removing the small segments on the images in Figure 4.3.

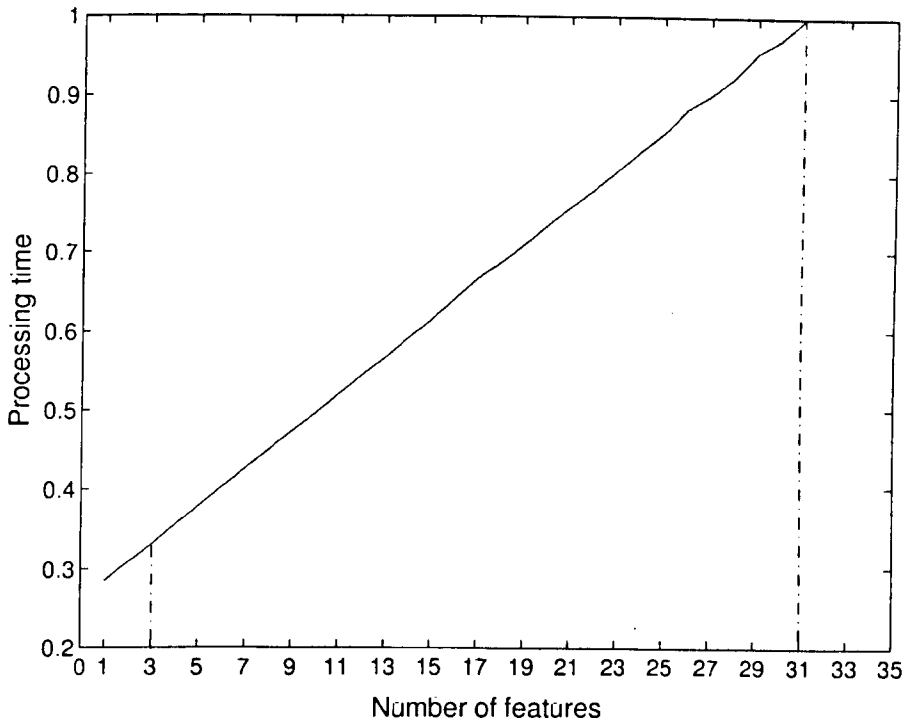

Figure 4.6: Effect of number of features on processing time.

Discussion

As demonstrated in Table 4.2, at specificity of 90%, the proposed three features give promising results of 93% and 86% sensitivity for normal and abnormal images respectively compared with the pixel classification method that uses a set of 31 features and gives 94% and 86% sensitivity for normal and abnormal images. Furthermore, at specificity of 95%, the sensitivity of the proposed method is 87% and 76% compared with 89% and 78% sensitivity of the pixel classification method for normal and abnormal images respectively. One of the factors that should be considered when using supervised classifiers is the size of feature vector. As the size of the feature vector is increased, the processing time is increased, as shown in Figure 4.6. Another factor that affects directly the complexity of the *KNN* classifier is the size of the training set. Let N_{Tr} and N_{Te} be the number of training and testing samples respectively. The *KNN* calculates distance between each pair of samples in the training set, then finds the sample with the smallest distance. The complexity of

the *KNN* is given by: $N_{Te} \times O(N_{Tr}^2)$. As a result of high computational requirements for the *KNN*, another method is investigated, (the *NNCA)* in the next section.

4.4 Nearest Neighbour Clustering Algorithm

In this section, retinal blood vessels are segmented using the *NNCA*. This algorithm is based on the nearest neighbours concept that is used in the *KNN* classifier with one main difference that this clustering algorithm does not need a training set [90].

4.4.1 Introduction

NNCA algorithm has the same analogy of the *KNN* classifier. This algorithm is completely unsupervised and there is no need for training set as in *KNN* classifier. Four parameters are used to control the clustering process of *NNCA*. These parameters are:

- N is number of pixels to be clustered,
- K_{init} is the nearest neighbour pixels from N,
- N_C is the number of required clusters,
- K is the number of nearest clustered pixels.

Initially, the clustering process is started by constructing non-overlapped clusters from randomly selected pixels. By increasing the neighbourhood of each pixel, one or more clusters can be combined which in turn reduce the number of clusters. This process is repeated until N_C clusters are obtained. Apart from the randomly selected pixels, each unselected pixel (unclustered pixel) is clustered to the most cluster of the nearest K clustered pixels from N. Finally, the degree of membership can be measured by obtaining the mean of the K nearest neighbours for each pixel in retinal image [90]. A flow chart to describe the *NNCA* is shown in Figure 4.7. Figure 4.8 shows the result for clustering blood vessels from a colour retinal sub-image.

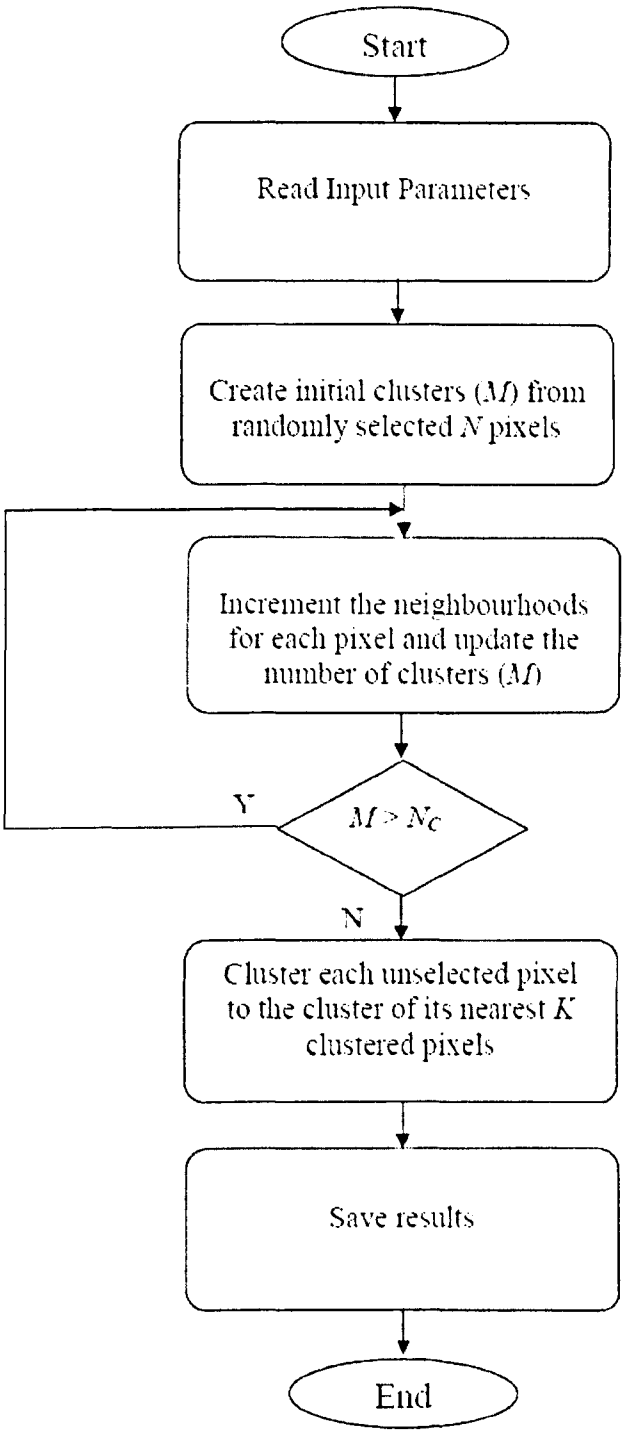

Figure 4.7: The Nearest neighbour clustering algorithm.

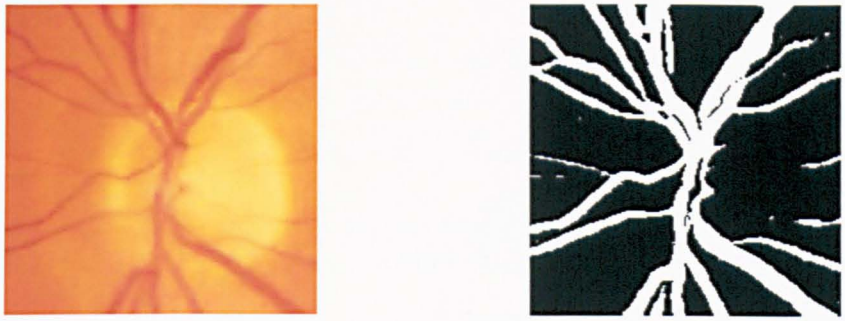

Figure 4.8: Colour sub-image with blood vessels clustered using *NNCA*.

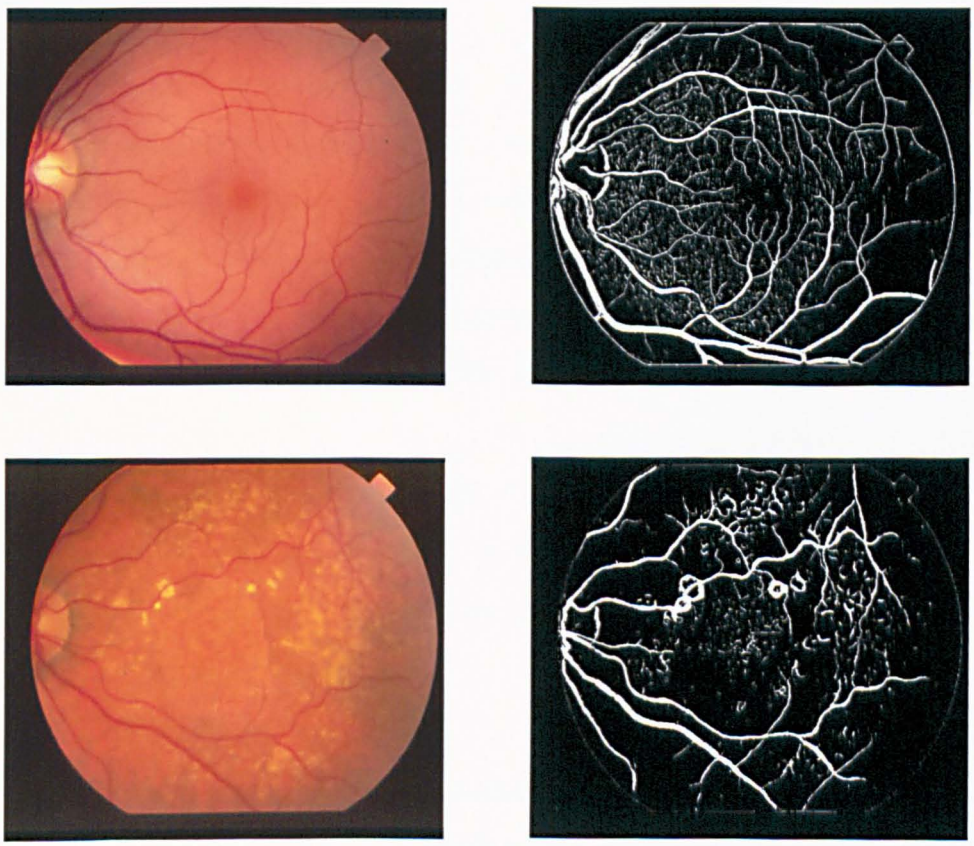

(a) (b)

Figure 4.9: (a) RGB images, and (b) output from the *NNCA* (hard decision) for normal (top) and abnormal (bottom) images .

Table 4.3: *NNCA* results (average from 20 images) [90]

Image type	Specificity %	Sensitivity %
Normal	92.30%	81.42%
Abnormal	87.61%	72.13%
All images	89.95%	76.77%

Table 4.4: *NNCA* results when using one feature (average from 20 images) [90]

Image type	Specificity %	Sensitivity %
Normal	94.97%	81.02%
Abnormal	93.53%	71.77%
All images	93.11%	76.39%

4.4.2 Experimental results

In these experiments, retinal blood vessels - from STARE dataset - are segmented using the *NNCA* in conjunction with the predefined set of features (green channel, gradient magnitude, and large eigenvalue). Figure 4.9 (a and b) shows two examples; normal (top) and abnormal (bottom) images and their results after blood vessel segmentation using the *NNCA*. On the whole, when using 20 images, average sensitivity of 77% is achieved at average specificity of 90% as summarised in Table 4.3. These values are calculated using the retinal FOV only.

Table 4.4 shows results when using the maximum eigenvalue as the only feature to cluster pixels which indicate an improvement in the specificity values compared to using the previous set of three features (green channel, gradient magnitude, and large eigenvalue).

4.4.3 Discussion

Two of the advantageous aspects of *NNCA* are that there is no need for a training set and it achieves results as a hard decision which can be directly used in further analysis of the blood vessel network. For soft classification or soft segmentation, FPR and TPR are calculated when the image is thresholded using different threshold values which gives the ROC curve. In this case, there is a need to decide the optimum threshold value to be used for each image. On the other hand, hard segmentation, gives a 1 or 0 value to each

image pixel to decide if it is a blood vessel or not, and in this case there is only one FPR corresponding to a single TPR to describe the performance of the method.
In segmentation of retinal blood vessel using the *NNCA*:

- Concepts of supervised and unsupervised methods are combined, where a feature vector is generated for each pixel in the image, then image pixels are clustered depending on these features without using a training set.
- For the twenty images in the dataset, average sensitivity and specificity of 77% and 90% are achieved respectively when using three features, and 76% and 93% respectively when using only one feature (the large eigenvalue).

The complexity of the *NNCA* depends on the number of randomly selected pixels, N_r, and the number of iterations, J, to achieve the required number of clusters. *NNCA* complexity is given by: $JN_r \times O(N_r^2)$. To reduce the complexity of the *NNCA*, Salem and Nandi [91] proposed a parallel implementation of the *NNCA* with a *fast* strategy to find the K nearest neighbour (*FKNN*) clusters. The *FKNN* strategy reduces the time required to find the nearest K clusters, which results in reducing the *NNCA* to $JN_r \times O(\sqrt{N_r \times \frac{k}{k-1}})$ which can be approximated to $JN_r \times O(\sqrt{N_r})$.

4.5 Radius-based Clustering Algorithm

Clustering is an example of unsupervised classification, where there are no predefined classes (labels). Clustering provides groups of objects (pixels) that have not yet been labelled "vessel" or "non-vessel". Labelling clusters effectively segments the pixels of the underlying retinal image. The process of labelling cluster objects "pixels" is always an expensive and error-prone task that requires time and human intervention. In many situations, objects are neither perfectly nor completely labelled. Therefore, the main idea of clustering with a partial supervision strategy is to take the advantage of the manually labelled objects to guide the clustering process of the unlabelled objects.

RACAL has been proposed to classify breast cancer tumors to benign and malignant [76]. This algorithm is a radius-based clustering algorithm which achieves clustering without the knowledge of the number of clusters using a distance parameter δ_o. In this section, *RACAL* is used to segment retinal blood vessels from colour fundus images. It is demonstrated from exploratory experiments that this algorithm is able to segment blood vessels of small diameters and low contrasts. In Section 4.5.3.2, a modification is proposed in *RACAL* to be used as a classifier.

4.5.1 Introduction

The main concept of *RACAL* is to discover the most centralised objects, prototypes, that can describe the distributions in the underlying dataset. These prototypes are determined through a user defined input parameter $\delta_o (0 \leq \delta_o \leq 1)$ [76]. Each prototype is considered as a cluster representative in such away that any object assigned to a cluster falls within the present distance parameter δ_o. It should be noted that small and tight clusters are achieved through small values of δ_o, while large values create large and loose clusters.

The partial supervision strategy for *RACAL* is used to guide the clustering process to a better search space [76]. In the supervised strategy, a small proportion of labelled objects (pixels) are used to supervise the clustering of the unlabelled pixels. Two steps are defined to perform the partial supervision. The first step is to achieve the clustering process using *RACAL* algorithm, i.e. cluster the entire pixels (all pixels in an image) into K clusters according to the input parameter δ_o, while the second step is to classify each cluster to either vessel or non-vessel classes. This is achieved by randomly select N_P pixels from the GT to be labelled pixels (vessel or non vessel), these labelled pixels are used to categorise clusters to either vessel or non vessel clusters. Then an iterative control strategy is applied to assign each misclassified pixel to the nearest cluster that belongs to the same class. After that, prototypes are updated and then the process is repeated until convergence. Finally, the class of each pixel is considered to be the class label of its cluster. A flow chart to describe the *RACAL* with partial supervision is shown in Figure 4.10.

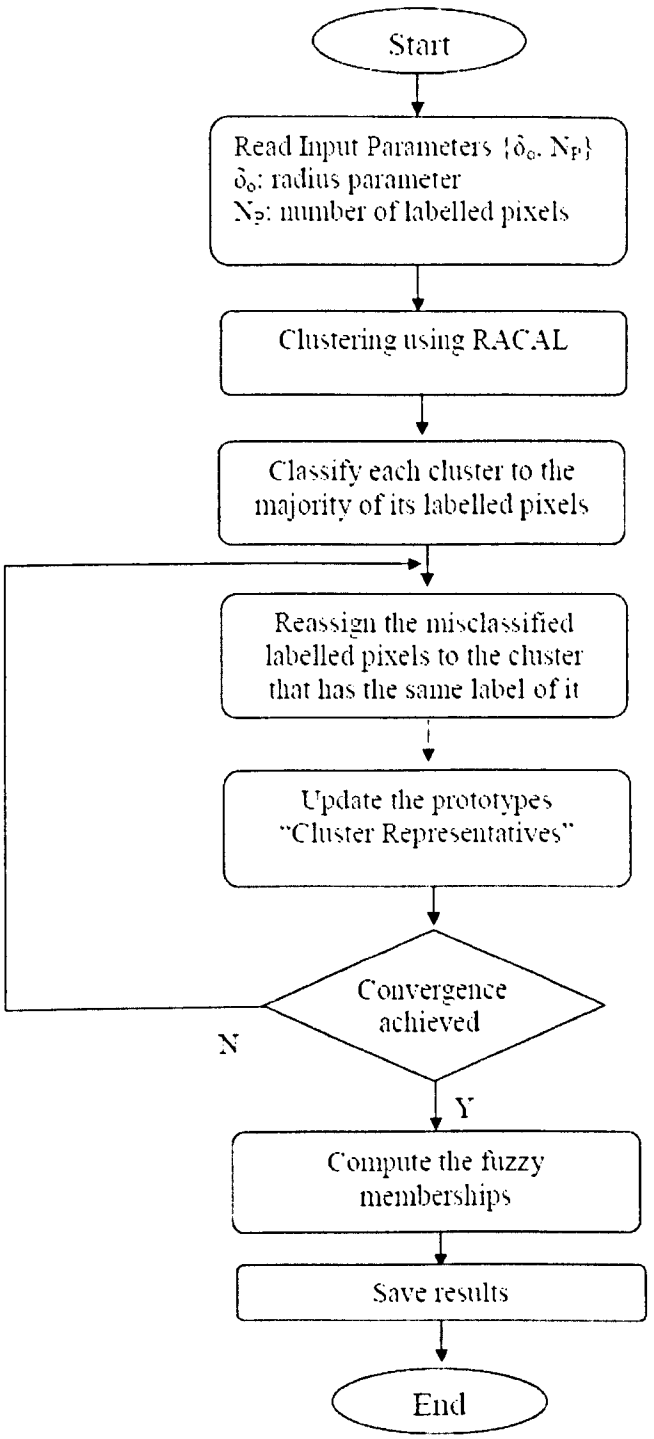

Figure 4.10: The Radius-based clustering algorithm with partial supervision.

Table 4.5: Specificity and sensitivity of a segmented sub-image from a retinal image by *RACAL* with partial supervision strategy at different δ_o values

δ_o	Specificity %	Sensitivity %
0.045	**97.90%**	**90.04%**
0.100	98.19%	89.04%
0.250	98.43%	81.73%
0.450	99.67%	70.90%

4.5.2 Experiments

In the experiments carried out, retinal blood vessels are segmented using *RACAL* with partial supervised strategy. Figure 4.11 shows a colour retinal sub-image and its GT, while Figures 4.12, 4.13, and 4.14 show the clustered sub-images by *RACAL* algorithm at different δ_o values and their corresponding segmented sub-images after applying *RACAL* with partial supervision strategy using 20% of the GT pixels. At $\delta_o = 0.045$, 0.100, 0.250 and 0.450, all pixels are being clustered to 245, 46, 10, and 4 clusters respectively. As shown in Table 4.5, smaller values for δ_o offer better sensitivity as a result of producing higher number of small and tight clusters which help in detection of vessels of small diameter and low contrast.

4.5.3 Experimental results

4.5.3.1 RACAL with partial supervision strategy

Hard decision

Results for retinal blood vessel segmentation using *RACAL* when applied to the 20 images in the STARE dataset are presented in this section. A binary mask is generated for each image in the dataset to segment the retinal FOV. Figure 4.15 (b and c) shows two examples; normal (left) and abnormal (right) images and their results after blood vessel segmentation

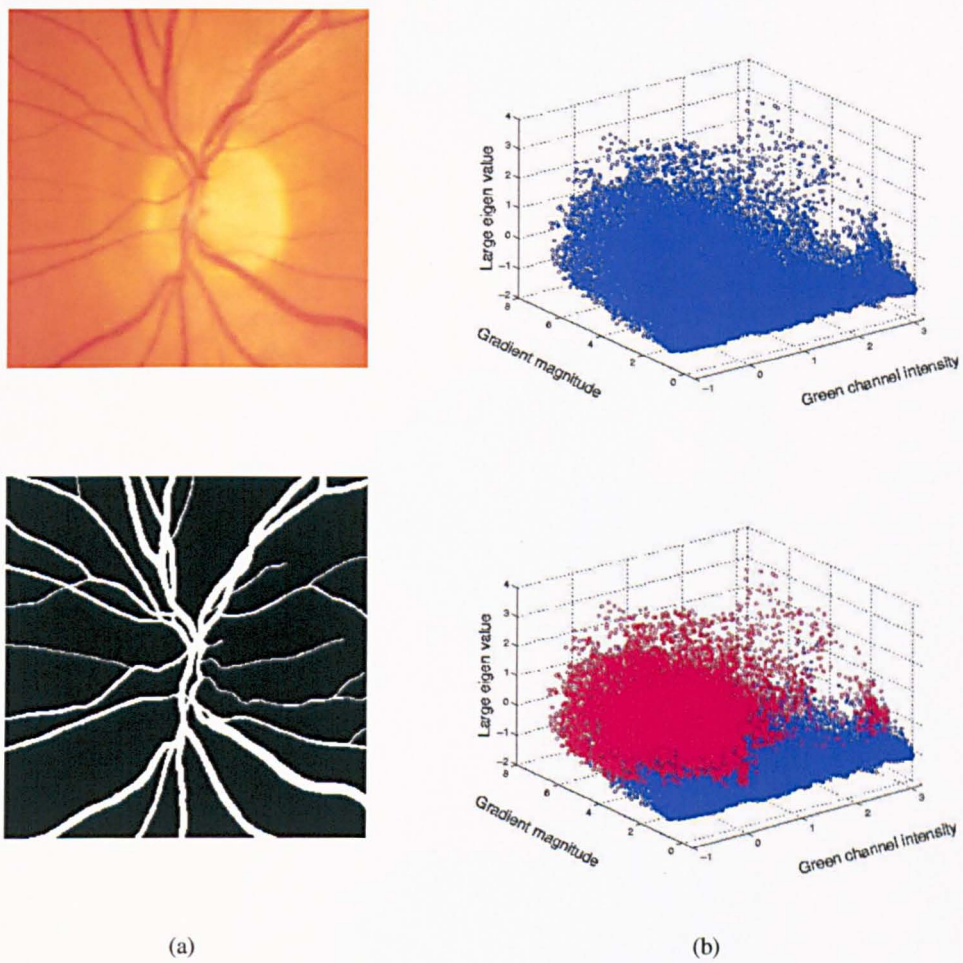

(a) (b)

Figure 4.11: Colour retinal sub-image (top) and its GT (bottom) in (a) image space, and (b) feature space.

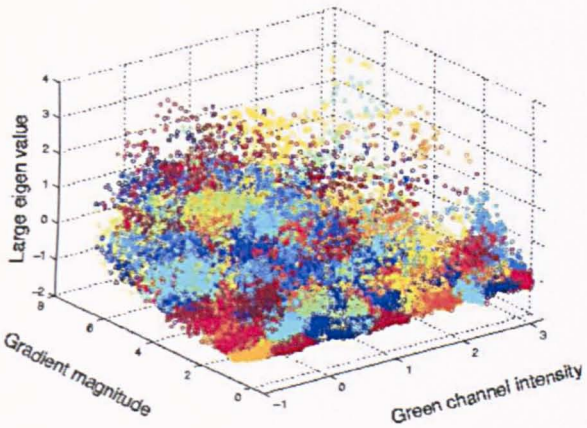

$\delta_0 = 0.045$

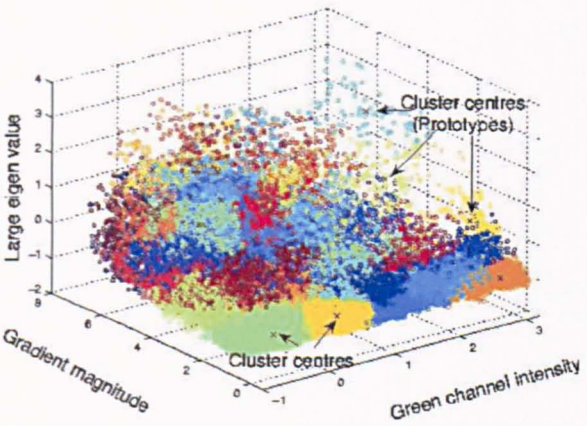

$\delta_0 = 0.100$

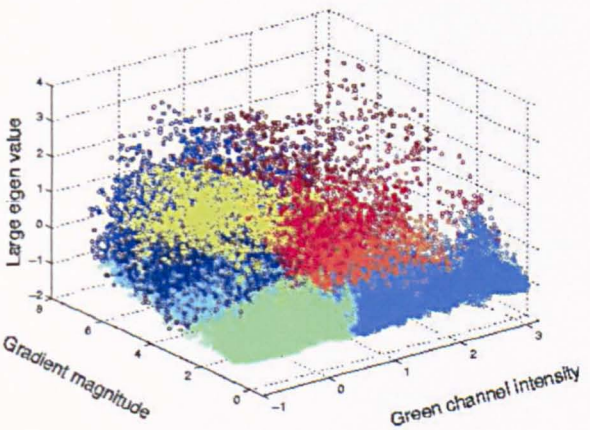

$\delta_0 = 0.250$

Figure 4.12: *RACAL* stage 1: clustering results for a sub-image when using different δ_o values in the feature space.

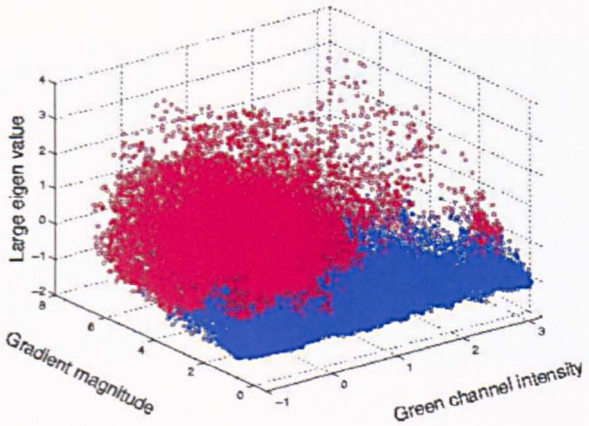

$\delta_0 = 0.045$

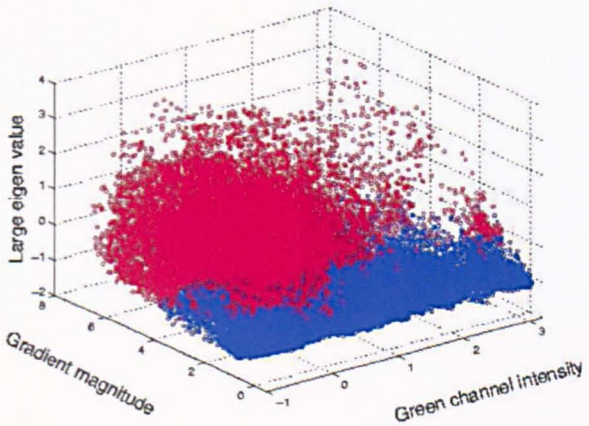

$\delta_0 = 0.100$

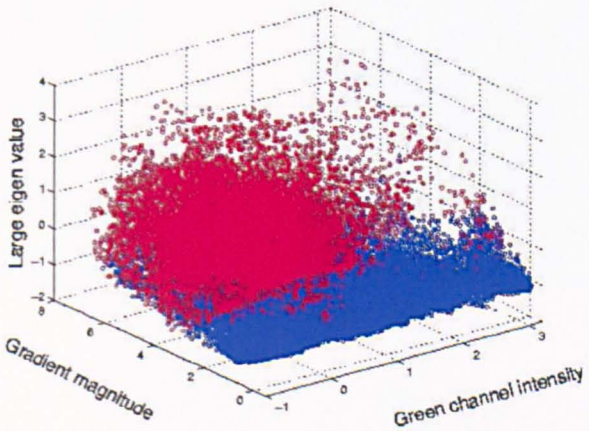

$\delta_0 = 0.250$

Figure 4.13: *RACAL* stage 2: after applying partial supervision strategy, results at different δ_o values in the feature space.

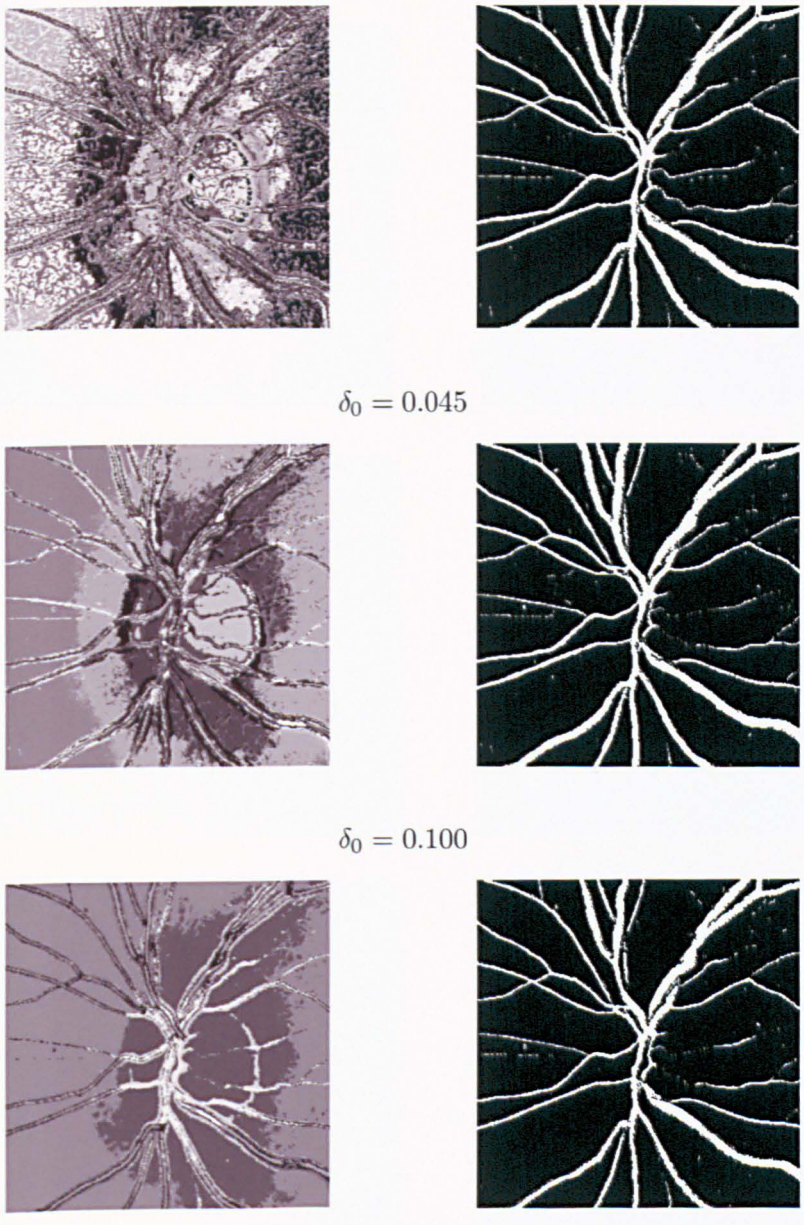

Figure 4.14: *RACAL* clustering results: (a) before, and (b) after applying the partial supervision strategy at different δ_o values (in the image space).

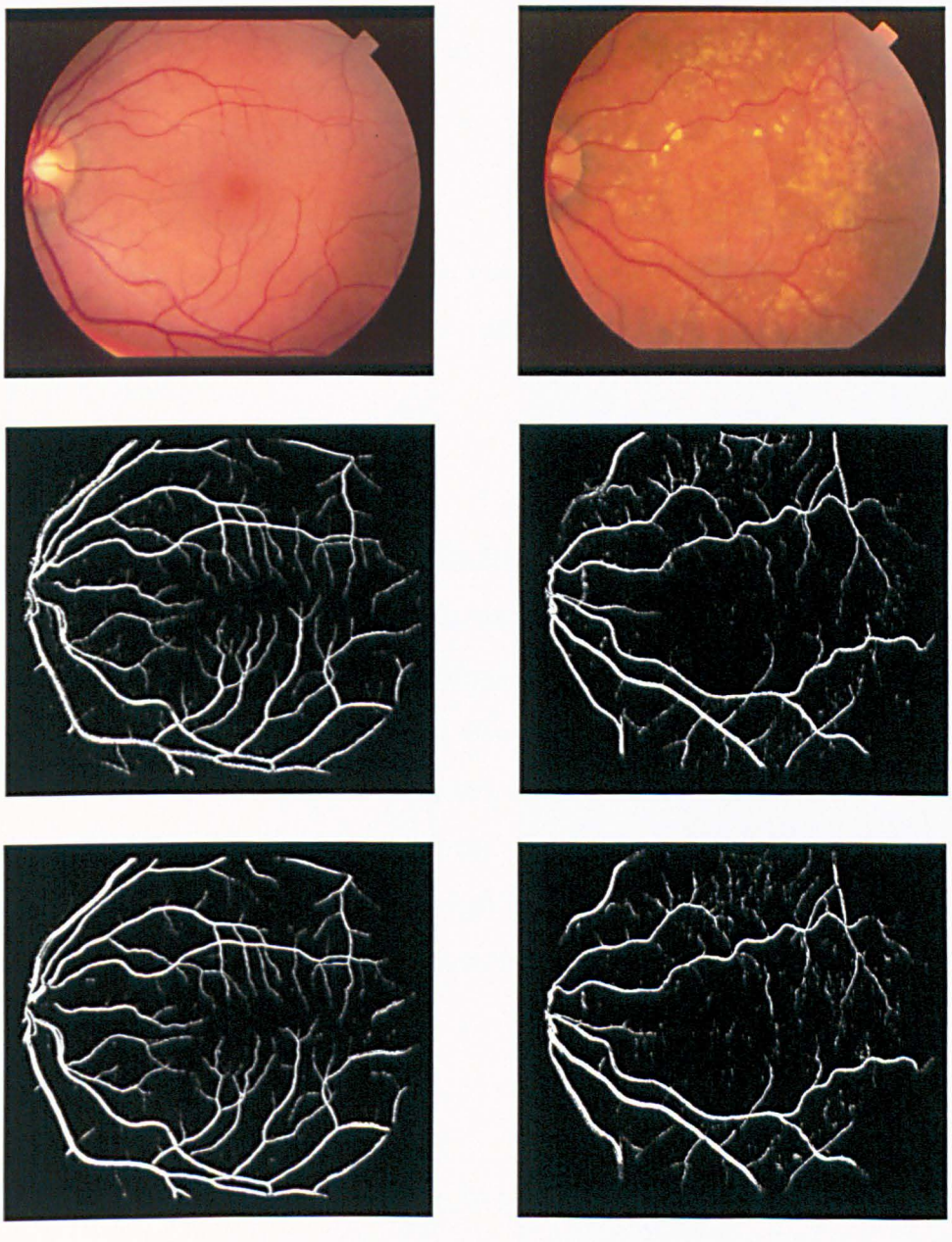

Figure 4.15: (a) RGB images, output as hard decision from *RACAL* when using (b) 3 features, and (c) 31 features for normal (left) and abnormal (right) images.

Table 4.6: *RACAL* "hard decision results" using 3 and 31 features (average from 20 images)

Features	3 Features		31 Features	
Image type	Specificity %	Sensitivity %	Specificity %	Sensitivity %
Normal	97.02%	85.01%	**97.64%**	**86.03%**
Abnormal	96.39%	77.67%	**97.36%**	**78.27%**
All images	96.70%	81.34%	**97.50%**	**82.15%**

using *RACAL* with partial supervision strategy. On the whole, using 20 images, average sensitivity of 81.34% and 82.15% are achieved at average specificity of 96.70% and 97.50% using the 3 and 31 features respectively, these values are calculated for the FOV only, as summarised in Table 4.6.

Soft decision

For soft classification, the performance of *RACAL* in terms of sensitivity and specificity along with the effect of the fuzziness exponent are obtained. As shown in Figure 4.16, the choice of the fuzziness exponent value q affects on pixels' membership degrees. Table 4.7 shows the soft decision results of *RACAL* in conjunction with 3 features to segment the retinal images (normal and abnormal). As shown, the fuzziness exponent value, $q = 1.25$, achieves better sensitivity with the corresponding specificity values for normal and abnormal images respectively. For 31 features, the fuzziness exponent value, $q = 1.50$, achieves better sensitivity with the corresponding specificity values for normal and abnormal images respectively as summarised in Table 4.8.

4.5.3.2 RACAL as a classifier

In this section, a modification to *RACAL* to be used as a classifier is proposed. It was shown, in the previous Sections, that *RACAL* with partial supervision strategy requires the knowledge of some labelled pixels from the GT. This knowledge is not always available. To overcome such a problem, two phases are required to modify *RACAL* to act as a classifier. A flow chart to describe these two phases is shown in Figure 4.17. The first phase is a *training phase*; where there is a training set of images. In this phase *RACAL* is applied to

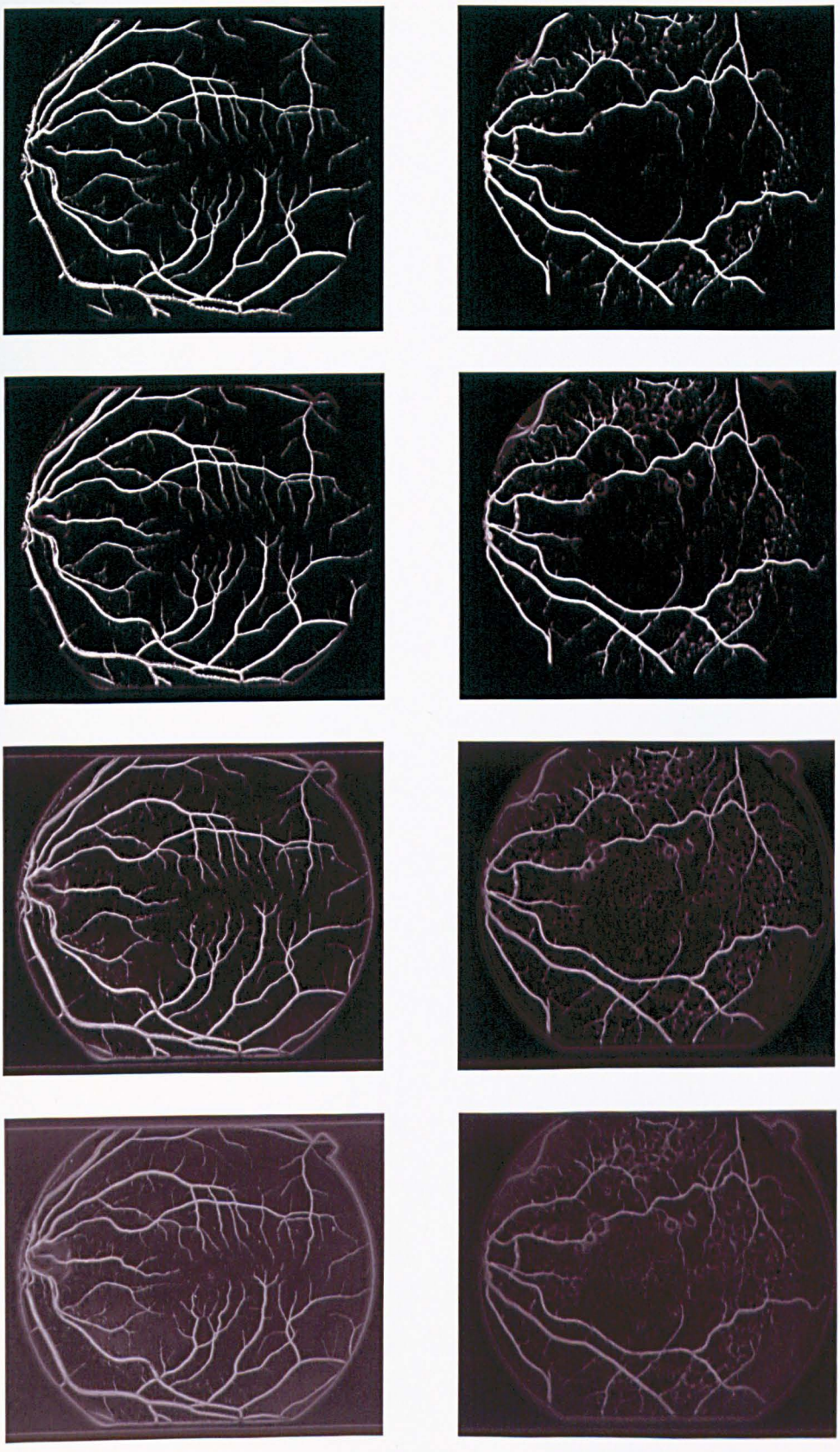

Figure 4.16: Effect of the choice of fuzziness exponent (q) on the segmented normal (left) and abnormal image (right) at (a) $q = 1.25$, (b) $q = 1.50$, (c) $q = 2.00$, and (d) $q = 2.50$.

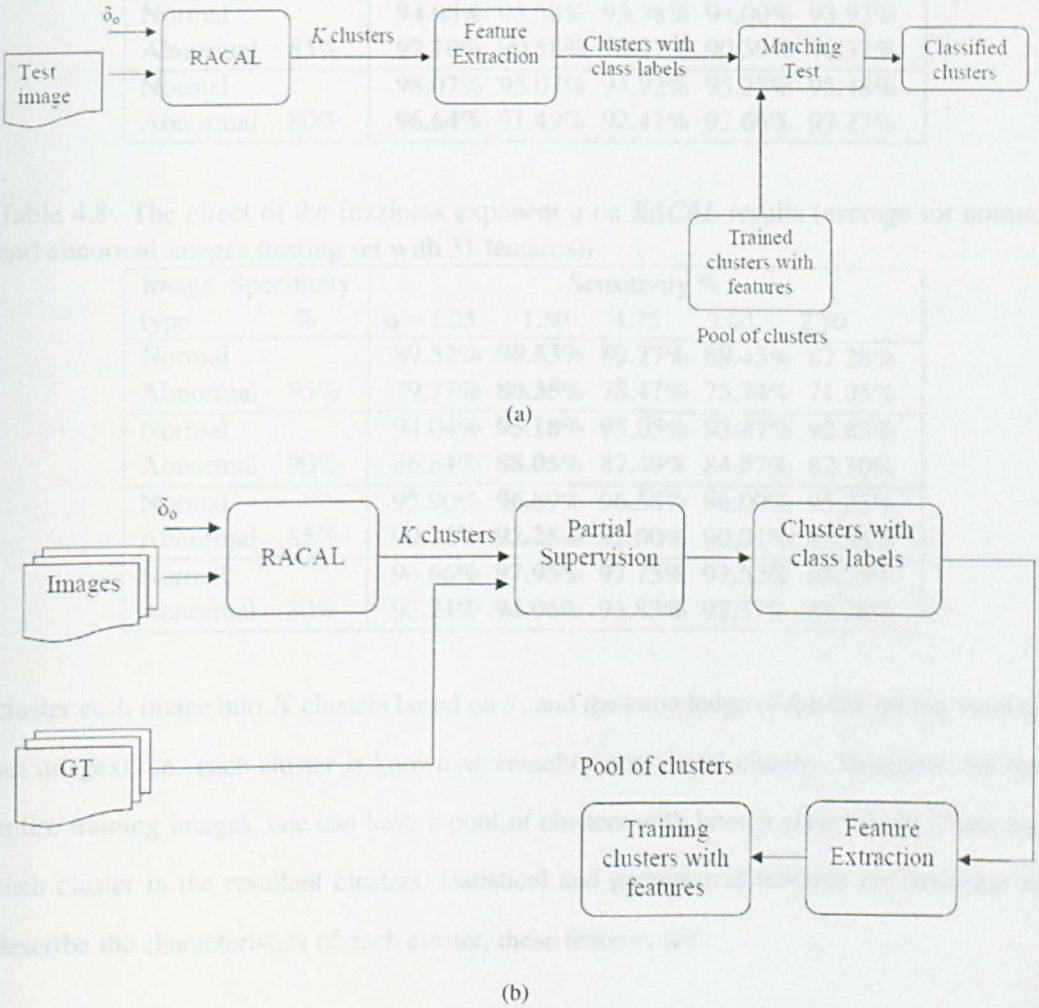

Figure 4.17: *RACAL* as a classifier (a) training phase, and (b) testing phase.

Table 4.7: The effect of the fuzziness exponent q on *RACAL* results (average for normal and abnormal images (testing set with 3 features))

Image type	Specificity %	Sensitivity % q = 1.25	1.50	1.75	2.00	2.50
Normal		**85.31%**	85.52%	86.19%	86.23%	86.11%
Abnormal	95%	**81.04%**	77.30%	77.68%	77.77%	77.19%
Normal		**92.89%**	91.31%	91.67%	91.98%	92.13%
Abnormal	90%	**93.53%**	85.86%	86.52%	86.26%	86.23%
Normal		**94.08%**	93.58%	93.78%	94.00%	93.93%
Abnormal	85%	**97.70%**	90.58%	90.17%	90.39%	90.37%
Normal		**98.07%**	95.07%	94.92%	95.28%	95.48%
Abnormal	80%	**96.64%**	91.49%	92.41%	92.66%	93.27%

Table 4.8: The effect of the fuzziness exponent q on *RACAL* results (average for normal and abnormal images (testing set with 31 features))

Image type	Specificity %	Sensitivity % q = 1.25	1.50	1.75	2.00	2.50
Normal		89.52%	**90.53%**	89.77%	89.45%	87.28%
Abnormal	95%	79.77%	**80.35%**	78.47%	75.74%	71.05%
Normal		94.04%	**95.18%**	95.05%	93.87%	92.83%
Abnormal	90%	86.84%	**88.05%**	87.49%	84.57%	82.30%
Normal		95.90%	**96.89%**	96.58%	96.00%	95.85%
Abnormal	85%	90.22%	**92.25%**	92.00%	90.01%	85.58%
Normal		96.66%	**97.95%**	97.75%	97.52%	95.75%
Abnormal	80%	92.24%	**94.06%**	93.83%	92.37%	88.38%

cluster each image into K clusters based on δ_o and the knowledge of the GT (of the training set images), i.e. each cluster is known as vessel or non-vessel cluster. Therefore, for the entire training images, one can have a pool of clusters with known class labels. Then, for each cluster in the resultant clusters, statistical and geometrical features are extracted to describe the characteristics of each cluster, these features are:

1. mean value for each feature of pixels in each cluster,
2. cluster compactness,
3. maximum diameter of the cluster,
4. minimum diameter of the cluster.

Table 4.9: *RACAL* as a classifier "hard decision results" using 3 and 31 features (average from 10 images (testing set))

Features	3 Features		31 Features	
Image type	Specificity %	Sensitivity %	Specificity %	Sensitivity %
Normal	**98.64%**	**91.33%**	99.57%	86.91%
Abnormal	**98.32%**	**89.52%**	98.71%	86.68%
All images	**98.48%**	**90.43%**	99.14%	86.79%

The second phase is the *testing phase*; where there is a testing set of images (unseen images). In this phase, *RACAL* is applied to cluster each image to achieve K clusters according to the input parameter δ_o. These clusters are achieved in an unsupervised manner, i.e. without the knowledge of the GT. As in the training phase, a set of features are generated for each cluster in a testing image. Then, each cluster in the testing set is classified to the class of the closest cluster in the training set. In the experiments carried out, 10 images (5 normal and 5 abnormal) from the STARE data are used as a training set while the other 10 images are used as a testing set. Figure 4.18 (b and c) shows two examples; normal (left) and abnormal (right) images and their results after blood vessel segmentation using *RACAL* as a classifier. Table 4.9 shows the classification performance (using the FOV only).

For 3 features, on average, 90.43% sensitivity is achieved at specificity of 98.48% while in 31 features, average sensitivity of 86.79% is achieved at average specificity of 99.14%. These results vindicate the robustness of the extracted features which are proposed in Section 4.2.

4.5.4 Discussion

For the hard classification, as demonstrated in Table 4.6 for 20 images in the STARE dataset, the *RACAL* with partial supervision strategy gives promising results of 81% and 82% average sensitivity at average specificity of 97% and 98% when using a set of 3 and 31 features respectively. These results are improved when using *RACAL* as a classifier, where it learned from 10 images and was then tested on the other 10 images.

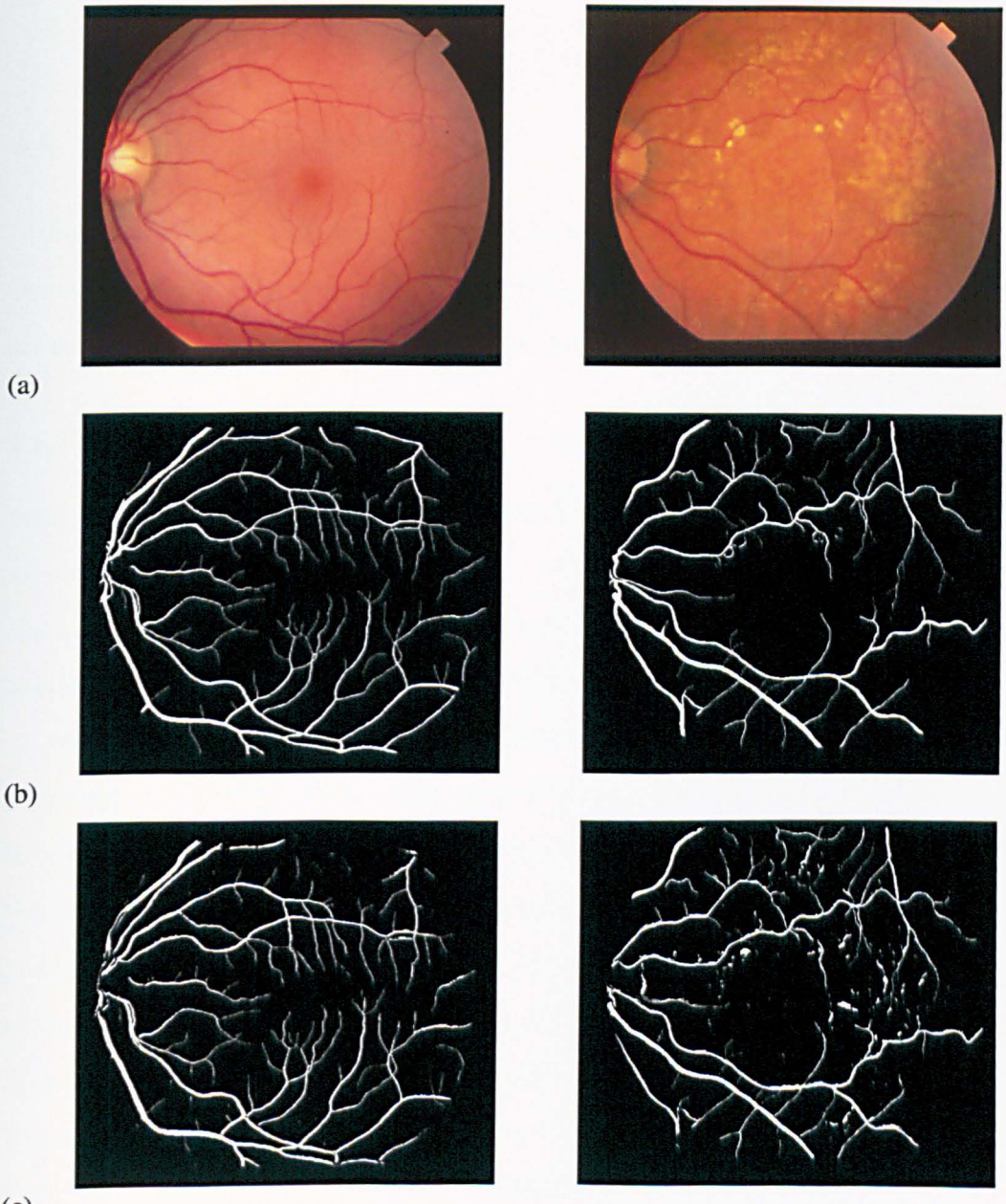

Figure 4.18: (a) RGB images, output from *RACAL* as a classifier when using (b) 3 features, and (c) 31 features for normal (left) and abnormal (right) images.

Table 4.10: *NNCA* results (average from 10 images (testing set))

Image type	Specificity %	Sensitivity %
Normal	91.70%	83.43%
Abnormal	87.21%	77.66%
All images	89.45%	80.54%

4.6 Comparative Results

In this section, results from the *NNCA* and *RACAL* algorithms are compared with results from the *KNN* classifier. When comparing with the *KNN* classifier, the same sets of images are used for training and testing (each set of 10 images).

4.6.1 NNCA versus KNN

Table 4.10 shows results from the *NNCA* using the same testing set of 10 images in order to compare with the *KNN* results in Section 4.3. Average sensitivity of 80.54% is achieved at average specificity of 89.45% from *NNCA* compared with average sensitivity of 85.47% at average specificity of 92.72% from the *KNN* classifier.

On average, the *KNN* classifier performs better than the *NNCA* because of the use of a training set that helps in the classification of pixels to vessels and non-vessel pixels. Results from *NNCA* are 5% less than the *KNN* classifier as it is completely unsupervised. For supervised classifiers, generating a training set required manually segmented images provided by an ophthalmologist or a trained person at least and the classifier needs to be trained for each and every dataset (as images were captured using different camera types, FOV's degree, and resolution). However, the performance of the clustering algorithm can be enhanced by adding new features that allow more accurate clustering for image pixels, such as: colour features, texture features, or directional features. Also the performance can be enhanced when clustering pixels to more than 2 clusters, i.e. to extend the non-vessels cluster to background, bright abnormal regions, and dark abnormal regions.

Table 4.11: *RACAL* "hard decision results" using 3 and 31 features (average from 10 images (testing set))

Features	3 Features		31 Features	
Image type	Specificity %	Sensitivity %	Specificity %	Sensitivity %
Normal	97.18%	85.96%	**98.28%**	**86.66%**
Abnormal	**96.90%**	**80.32%**	96.86%	79.90%
All images	97.04%	83.14%	**97.57%**	**83.28%**

Table 4.12: Average sensitivity at certain specificity values for 3 and 31 features

Image type	Specificity %	3 Features Sensitivity %	31 Feature Sensitivity %
Normal		85.31%	**90.53%**
Abnormal	95%	**81.04%**	80.35%
All images		83.18%	**85.44%**
Normal		92.89%	**95.18%**
Abnormal	90%	**93.53%**	88.05%
All images		**93.21%**	91.62%
Normal		94.08%	**96.89%**
Abnormal	85%	**97.70%**	92.25%
All images		**95.89%**	94.57%
Normal		**98.07%**	97.95%
Abnormal	80%	**96.64%**	94.06%
All images		**97.36%**	96.00%

4.6.2 RACAL versus KNN

Hard decision results from *RACAL* are comparable with the *KNN* classifier as demonstrated in Tables 4.1 and 4.11. *RACAL* achieves average specificity of 97% and 98% at average sensitivity of 83% compared with average specificity of 93% and 94% at average sensitivity of 85% and 84% when using the *KNN* classifier in conjunction with 3 and 31 features respectively. On average, *RACAL* algorithm achieves better specificity than *KNN* classifier with comparable sensitivity.

Soft results obtained from *RACAL* - using same features and same testing set of images - are summarised in Table 4.12. When compared with *KNN* classifier (Table 4.2), it is clear that *RACAL* offers better results for abnormal images, and comparable results for normal images.

In the case of normal images, the *RACAL* gives comparable results with the *KNN* classi-

fier, on the other hand it gives better results for the abnormal images which can be explained as follows:

- For the *KNN* classifier: one training set is generated for the whole dataset and used to find the nearest K-neighbours for each sample in the testing set.
- For the *RACAL*: training samples are for each image individually which can reflect each image characteristics (such as: background colour, intensity levels for vessel and non-vessel pixels, contrast between vessels and background, ... etc).
- The property of multiple object classes of varying colour/reflectance [46] and - sometimes - there is a similarity between feature vectors for vessel and non-vessel pixels from different images. *RACAL* is a radius-based algorithm which means better segmentation for small and low contrast vessels.
- For normal images there are no abnormalities and the background is uniformly illuminated, so the results were comparable.
- For abnormal images, there are signs for abnormalities which are misclassified as vessels in the *KNN*. In addition to the small blood vessels (of low contrast) that are missed in the *KNN* classifier and picked by *RACAL*.

When using *RACAL* as a classifier, the performance is better than the *KNN* for both normal and abnormal images.

4.7 Summary and Conclusions

In this chapter, three methods - supervised, unsupervised, and semi-supervised methods - to segment retinal blood vessels from colour fundus images were investigated. A feature vector of three features in conjunction with the *KNN* classifier is proposed to classify pixels of retinal images as vessel pixels or non-vessel pixels. The local maxima of the large eigenvalue has been proposed to be used as a feature in addition to the green channel and the local maxima of the gradient magnitude of the intensity image. Results have shown

that using these three features significantly reduces the processing time with comparable sensitivity to the pixel classification method that uses 31 features.

The *NNCA* is used to cluster pixels of retinal images into those belonging to blood vessels and others not belonging to blood vessels, based on feature vectors. Experimental results show that the *NNCA* gives promising results with the advantage that it is completely unsupervised and needs no training set.

RACAL with partial supervision has been used in segmentation of retinal blood vessels which is helpful in cases where GT images are not completely available. The performance is enhanced when using *RACAL* as a classifier (by learning from a set of images, then classifying unseen images). The *RACAL* has been used as classifier to classify image pixels as vessels and non-vessel pixels and its results were comparable with the *KNN* classifier in normal cases. On the other hand, for the abnormal images, results were better than the *KNN* classifier which has been demonstrated in Section 4.6.2. An interesting observation about partial supervised methods is that it gives comparable results with the *KNN* classifier. This will lead to another question: can we use an algorithm to segment the retinal image and then choose a trusted set of pixels to act as GT for a semi-supervised method?

As discussed, there was a trade off between performance, complexity, and the availability of GT. In cases where GT images are available, best results were obtained using *KNN* or *RACAL* as a classifier. On the other hand, when using the *NNCA* - as an unsupervised method - performance was 5% less than that obtained from the *KNN*.

Unsupervised methods have the advantage of not using a training set, so there is no need for the manually labelled images, or generating features for each pixel in the image which directly affects the performance and complexity of supervised methods. Unsupervised methods, in the literature, require a number of parameters that need to be set, which limit their applicability. Motivated by these prerequisites, an unsupervised method is proposed in the next chapter to segment retinal blood vessels based on eigenvalue analysis of the Hessian matrix that requires the setting of one parameter only.

Chapter 5

Vesselness Measure

5.1 Introduction

IN this chapter, a novel vesselness measure is proposed which is based on eigenvalues and eigenvectors of the Hessian matrix, the matrix of the second order derivatives of the intensity image. Blood vessel centrelines and orientations are used to measure the vesselness. Vessel centrelines are detected from the large eigenvalue of the Hessian matrix while the orientation is estimated from eigenvectors that correspond to the small eigenvalues. Based on this vesselness measure, an unsupervised method for segmentation of retinal blood vessels from colour fundus images is proposed. The main advantage of the proposed method is that it is completely unsupervised, so there is no need for manually labelled images which are time consuming and require an expert.

5.2 Related Work

In the literature, the term "vesselness" is used to refer to the degree of being a vessel for a certain pixel in an image. Different measures have been proposed for many applications in 2D and 3D images, such as vessel enhancement [85, 92, 86], identifying vessel centrelines [53], and vessel segmentation [49]. In [85, 92] multi-scale line filters are proposed for segmenting line-like structures based on eigenvalues of the Hessian matrix. The similarity

measure, μ, proposed by Lorenze *et al.* [85] (assuming ($|\lambda_1| > |\lambda_2| > |\lambda_3|$), for 2D and 3D images, is as follows:

$$\mu_{2D} = \sigma^{\gamma} \frac{|\lambda_1|}{|\lambda_2|} \tag{5.1}$$

$$\mu_{3D} = \sigma^{\gamma} \frac{|\lambda_1| + |\lambda_2|}{2|\lambda_3|} \tag{5.2}$$

where $\gamma > 0$, and σ is the width of the Gaussian Kernel.

Sato *et al.* [92] propose another similarity measure to discriminate line structures from other structures in 3D images, they sort the eigenvalues in increasing values (not absolute ones), i.e. $\lambda_1 > \lambda_2 > \lambda_3$). The similarity measure for line-like structures is given by:

$$L = f(\lambda_1; \lambda_c) \times \lambda_c \tag{5.3}$$

$$f(\lambda_1; \lambda_c) = \begin{cases} e^{-\frac{\lambda_1^2}{2(\alpha_1 \lambda_c)^2}} & \lambda_1 \leq 0, \lambda_c \neq 0 \\ e^{-\frac{\lambda_1^2}{2(\alpha_2 \lambda_c)^2}} & \lambda_1 > 0, \lambda_c \neq 0 \\ 0 \end{cases} \tag{5.4}$$

where $\lambda_c = min(-\lambda_2, -\lambda_3) = -\lambda_2$, and $\alpha_1 < \alpha_2$.

Frangi *et al.* [86] propose a vesselness measure taking into account responses from blob-, plate-, and line-like structures, this measure considers responses from background pixels. Frangi's vesselness measure for 3D images is given by:

$$\nu_o(s) = \begin{cases} 0 & \text{if } \lambda_2 > 0 \text{ or } \lambda_3 > 0, \\ (1 - e^{-\frac{R_A^2}{2\alpha^2}}) e^{-\frac{R_B^2}{2\beta^2}} (1 - e^{-\frac{S^2}{2c^2}}) \end{cases} \tag{5.5}$$

This measure is given in 2D images by:

$$\nu_o(s) = \begin{cases} 0 & \text{if } \lambda_2 > 0, \\ e^{-\frac{R_B^2}{2\beta^2}} (1 - e^{-\frac{S^2}{2c^2}}) \end{cases} \tag{5.6}$$

where α, β, and $\mathcal{S}$ are thresholds to control the filter sensitivity, and the other ratios are:

- $R_A = \frac{|\lambda_2|}{|\lambda_3|}$ to distinguish between plate- and line-like structures,
- $R_B = \frac{|\lambda_1|}{\sqrt{|\lambda_2 \lambda_3|}}$ to account for the deviation from a blob-like structures,
- $\mathcal{S} = \sqrt{\sum_{j \leq D} \lambda_j^2}$ to differentiate between vessel and background pixels.

It is important to note that in 2D images, the term that differentiates between plate- and line-like structures is removed which makes this measure not effective in distinguishing between vessel and edge pixels.

The vesselness measure proposed by Sofka *et al.* [53] is based on six responses for vessel and edge pixels. These responses are the multi-scale matched filter r_v, multi-scale edge detection (results in two edges r_{es}, and r_{ew}), and confidence measures for vessel η_v and edge ($\eta_{es}$and η_{ew}) pixels. Then, a six dimensional vector, Θ, is mapped into a single likelihood ratio to produce a vesselness measure LRV.

$$LRV(\Theta) = \frac{P(\Theta/\text{on})P(\text{on})}{P(\Theta/\text{off})P(\text{off})} \tag{5.7}$$

where $\Theta(\mathbf{x}) = (r_v(\mathbf{x}), r_{es}(\mathbf{x}), r_{ew}(\mathbf{x}), \eta_v(\mathbf{x}), \eta_{es}(\mathbf{x}), {}_{ew}(\mathbf{x}))$, $P(\text{on})$ is the prior probability of a pixel being on the centreline of a vessel, $P(\Theta/\text{on})$ is the conditional probability density function, and $P(\text{off}) = 1 - P(\text{on})$. This vesselness measure is mainly concerned with vessel centrelines rather than retinal blood vessel extraction.

In [49], a hybrid multi-scale filter is proposed to segment retinal blood vessels which combines eigenvalues of the Hessian matrix V_h, the response of matched filters V_m, and edge constrains V_e, all calculated at different scale values s.

V_h is produced using the ratio of the eigenvalues($|\lambda_1| > |\lambda_2|$) of the Hessian matrix as follows:

$$V_h(\mathbf{x}; s) = \begin{cases} e^{-\frac{|\lambda_2/\lambda_1|^2}{2\beta^2}}(1 - e^{-\frac{|\lambda_1|^2}{2\gamma^2}}) & \text{if } \lambda_1 < 0 \\ 0 \quad \text{otherwise} \end{cases} \tag{5.8}$$

$$\gamma = \frac{I_{xy}}{\alpha/\sqrt{s}}$$

where $\gamma = \frac{I_{xy}}{\alpha/\sqrt{s}}$, $I_{xy}$is the image intensity at pixel (x, y), s is the scale value, β and α are constants.

The matched filter response is obtained by convolving the the pixels in the cross section with a vector m and given by:

$$V_m(\mathbf{x}; s) = \frac{p.m}{|p|\,|m|} \tag{5.9}$$

where $m_i|_{i=1:s} = -1$, $m_i|_{i=s+1:3s} = 1$, and $m_i|_{i=s+1:4s} = -1$, and p represents the intensities of pixels in a cross section of length $4s$.

Edge responses are obtained by convolving the pixels with a step edge filter to produce V_e^1 and V_e^2, both values should be positive. The final vesselness measure is given by:

$$F(\mathbf{x}; s) = \begin{cases} V_h(s).V_m(s) & \text{if } V_e^1(s) > 0 \wedge V_e^2(s) > 0 \\ 0 & \text{otherwise} \end{cases} \tag{5.10}$$

Results in [49] are reported when defining TP as any pixel marked by the filter as a vessel and is located within a 3×3 neighbourhood from a GT pixel. While FP is defined as any pixel marked by the filter as a vessel and not included in any GT vessel. These definitions are different from the definition used in this thesis for performance evaluation in Section 2.2.4.3.

5.3 Proposed Vesselness Measure

Blood vessels can be considered as dark elongated line structures - of different diameters and orientations - on a brighter background. The proposed vesselness measure is based on detecting vessels centrelines and orientations over scales.

5.3.1 Vessel centrelines

In Section 4.2, the large eigenvalue of the Hessian matrix was used as an indicator of the vessel centreline (without using the absolute value). As vessels are of different diameters, then different scales are used to calculate the eigenvalues, keeping the maximum response at each image pixel over scales. Eigenvalues (the large eigenvalue, λ_+, and the small

eigenvalue, λ_-, where $\lambda_+ > \lambda_-$) of the Hessian matrix of the intensity image $I(x, y)$ are calculated as in Equations 4.5 and 4.6. The local maximum of the large eigenvalue λ_{max}, over scales, is calculated as :

$$\lambda_{max} = \max_{s} [\lambda_+(s)] \tag{5.11}$$

What has been observed from the experiments is that as the scale parameter value increases so does the apparent diameter of the detected blood vessel. This can be clearly appreciated from Figure 5.1 which displays a sub-image and the corresponding sub-images containing the large eigenvalue at every pixel at six different scales. Figure 5.2 shows the large eigenvalue at different scales for a sub-image, as the scale parameter increases, vessels of different diameters can be detected. In this Figure, thin vessels (as in bottom of the sub-image) can be detected at small values of s ($s = 1$), while wider vessels (in the middle) can be detected at bigger values of s ($s = 2$ or $s = 3$). Very wide vessels needs larger values for s.

It is important to note that in Equation 5.11, the scale value s is not used in the denominator as in Equation 4.7. In Equation 4.7, the vessel centrelines were extracted and then the gradient magnitude (Equation 4.4) is used to compensate the remaining part of the vessel. But in the proposed vesselness measure, most of the vessel is needed as a first stage, then the orientation will be used to remove responses outside the vessel.

Figure 5.3 shows the maximum over scales, for the large eigenvalues, when using Equations 4.7 and 5.11. It is clear that most of the vessel can be extracted when using Equation 5.11 compared to using Equation 4.7 (which results in centreline detection rather than the full vessel). In the next step, the orientation will be used to decide which part of the response does not resemble to a blood vessel.

5.3.2 Vessel orientation

Vessel orientation in degrees, θ, are calculated from the eigenvectors of the Hessian matrix, in Appendix C.3, as:

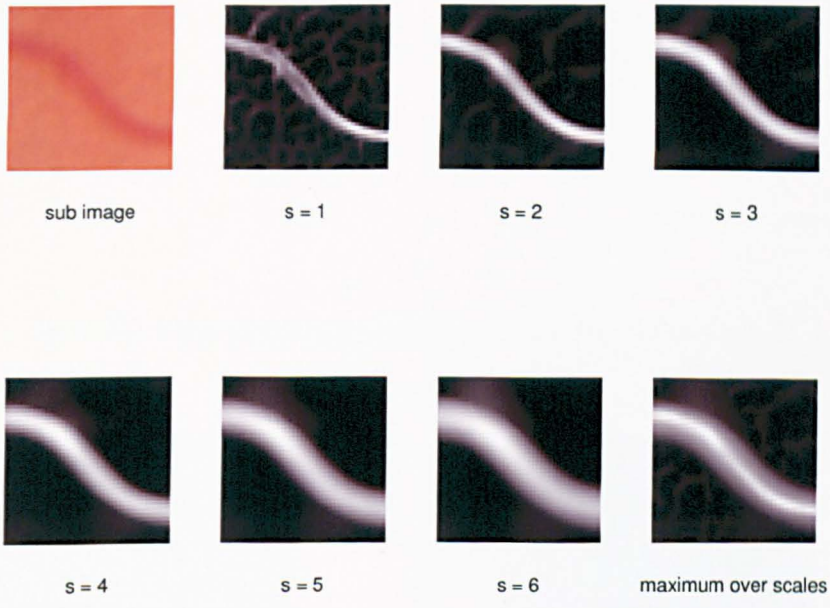

Figure 5.1: The large eigenvalue for a retinal blood vessel at different scales.

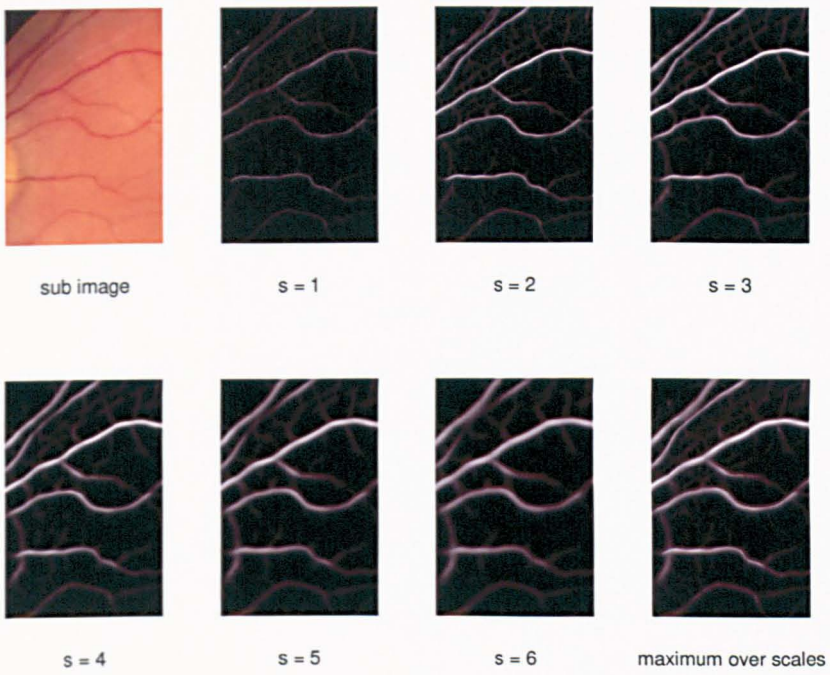

Figure 5.2: Large eigenvalue at different scales for a sub-image.

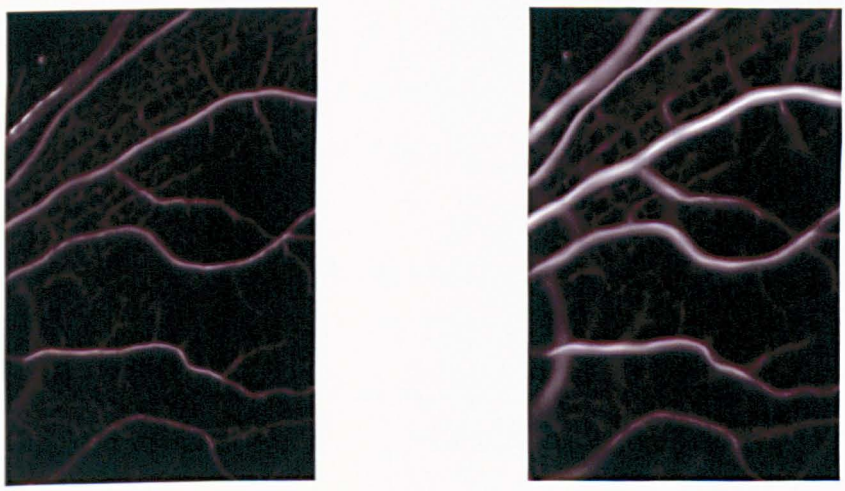

(a) (b)

Figure 5.3: Large eigenvalue, maximum over scales, when using (a) Equation 4.7, and (b) Equation 5.11.

$$\hat{e}_+ = \frac{\mathrm{I}}{N} \begin{vmatrix} 2L_{xy} \\ L_{yy} - L_{xx} + \alpha \end{vmatrix} \tag{5.12}$$

$$\hat{e}_- = \frac{\mathrm{I}}{N} \begin{vmatrix} L_{yy} - L_{xx} + \alpha \\ -2L_{xy} \end{vmatrix} \tag{5.13}$$

$$\theta_+ = tan^{-1}\left[\frac{L_{yy} - L_{xx} + \alpha}{2L_{xy}}\right] \tag{5.14}$$

$$\theta_- = tan^{-1}\left[\frac{-2L_{xy}}{L_{yy} - L_{xx} + \alpha}\right] \tag{5.15}$$

where $\hat{e}_+$ and $\hat{e}_-$ are eigenvectors, and θ_+ and θ_- are orientations of the corresponding λ_+ and λ_-, and $N = \sqrt{(L_{yy} - L_{xx} + \alpha)^2 + 4L_{xy}^2}$.

Figure 5.4 shows eigenvectors corresponding to large and small eigenvalues at different scales. Orientation from the eigenvector that corresponds to the small eigenvalue shows the direction of the vessel, while the orientation from the eigenvector that corresponds to the large eigenvalue shows the direction of the large changes in the intensity values which represents the perpendicular direction to the vessel. As explained earlier, when the scale parameter increases, the vessel diameter increases, while the vessel orientation remains the same over scales.

Directions of eigenvectors corresponding to the small eigenvalue at each pixel are depicted in the sub-image for six different scales in Figure 5.5. It has also been observed that the variation of the directions of the eigenvectors in a pixel over six different scales is smaller for blood vessel pixels compared with non-blood vessel pixels. Therefore to quantify this variation, the standard deviation of eigenvectors corresponding to smaller eigenvalues over scales is used. At vessel centres, the standard deviation of θ_-(angle with respect to $x-$ axis calculated from the eigenvector that corresponds to small eigenvalue λ_-) over scales tends towards zero, or a very small value, compared with higher values

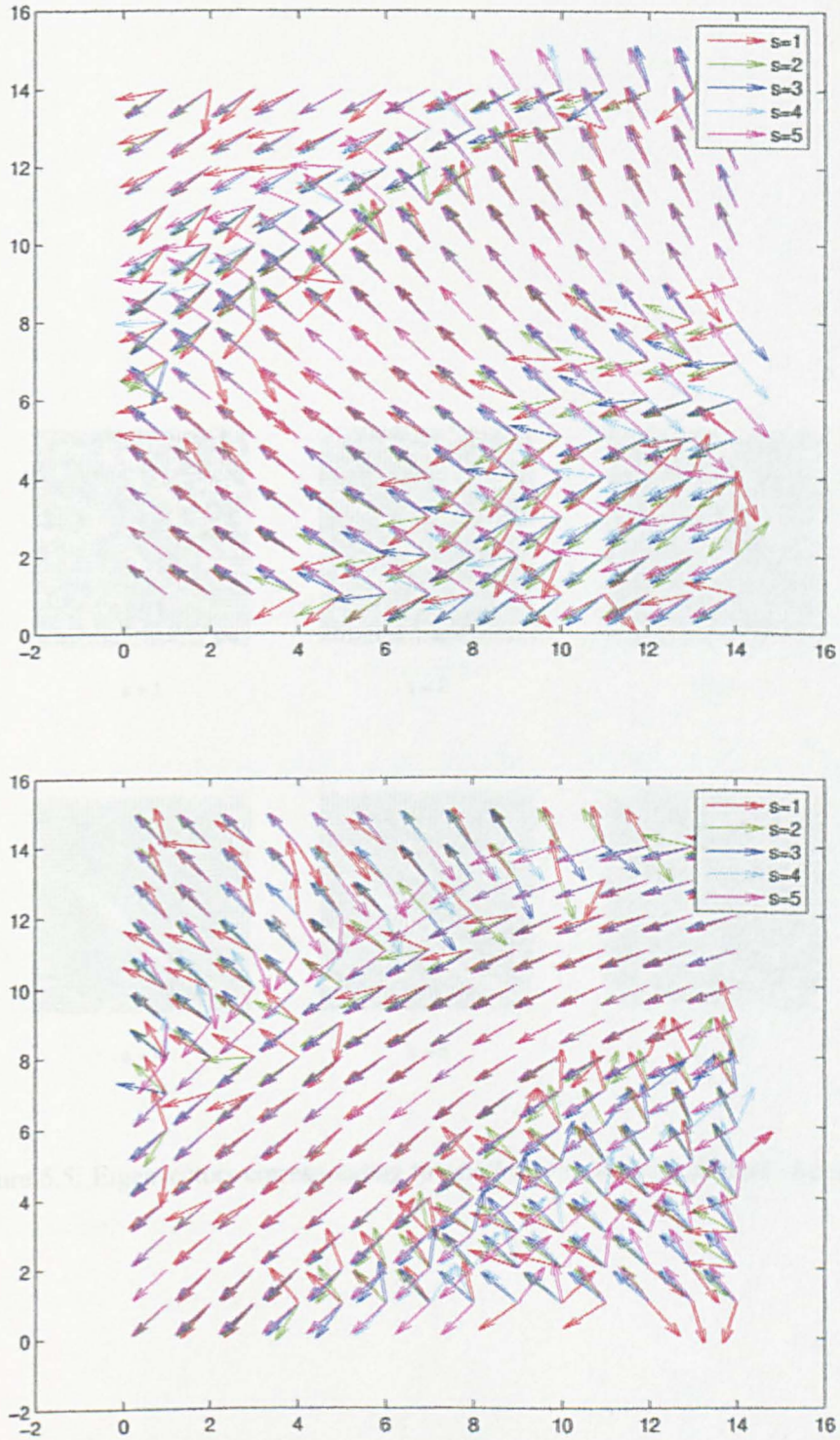

Figure 5.4: Eigenvectors corresponding to large (top), and small (bottom) eigenvalues at different scales.

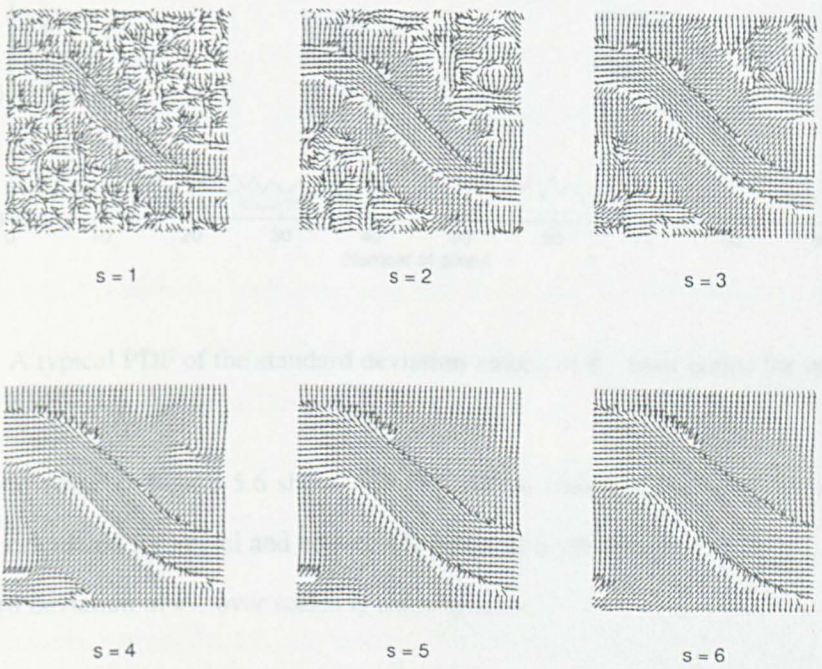

Figure 5.5: Eigenvectors corresponding to small eigenvalues at different scales.

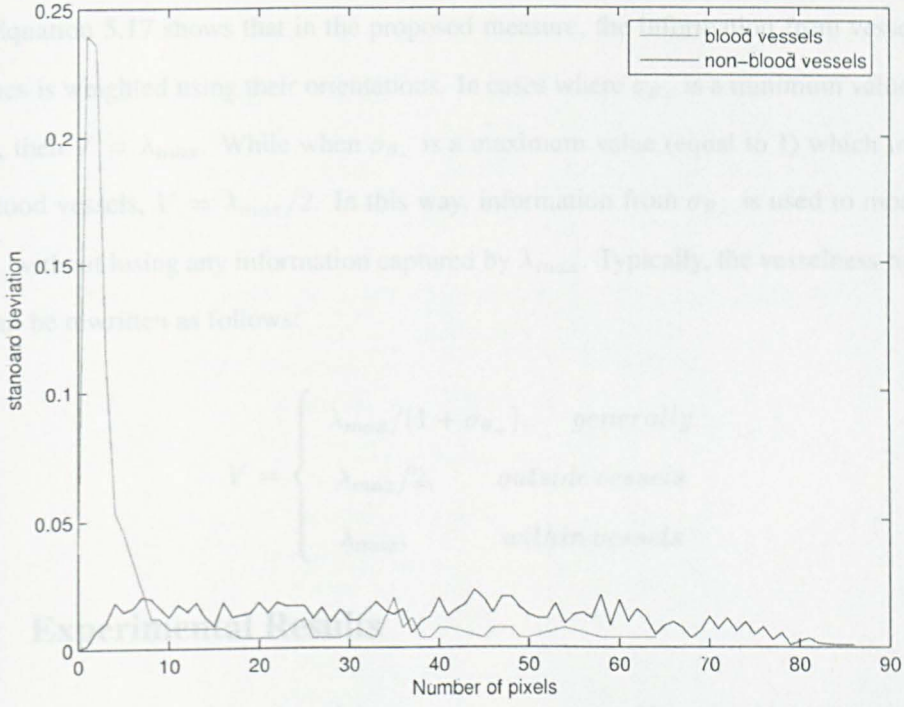

Figure 5.6: A typical PDF of the standard deviation values of θ_- over scales for vessel and non-vessel pixels.

outside blood vessels. Figure 5.6 shows the PDF of the standard deviation values of θ_- over scales calculated for vessel and non-vessel pixels in a sub-image.

The standard deviation of θ_- over scales is calculated as:

$$\sigma_{\theta_-} = \underset{s}{std}\left[\theta_-(s)\right] \tag{5.16}$$

5.3.3 Vesselness measure

The proposed vesselness measure V is calculated as :

$$V = \frac{\lambda_{max}}{1 + \sigma_{\theta_-}} \tag{5.17}$$

where λ_{max} is the local maximum of the large eigenvalue over scales, σ_{θ_-} is the standard deviation of the θ_- over scales. Values of λ_{max} and σ_{θ_-} are normalised to be between 0 and 1.

Equation 5.17 shows that in the proposed measure, the information from vessels centrelines is weighted using their orientations. In cases where $\sigma_{\theta\_}$ is a minimum value (equal to 0), then $V = \lambda_{max}$. While when $\sigma_{\theta\_}$ is a maximum value (equal to 1) which indicates no blood vessels, $V = \lambda_{max}/2$. In this way, information from $\sigma_{\theta\_}$ is used to modify the λ_{max} without losing any information captured by λ_{max}. Typically, the vesselness measure, V, can be rewritten as follows:

$$V = \begin{cases} \lambda_{max}/(1+\sigma_{\theta\_}), & generally \\ \lambda_{max}/2, & outside\ vessels \\ \lambda_{max}, & within\ vessels \end{cases}$$

5.4 Experimental Results

In the experiments performed, each image was pre-processed by using histogram matching, as proposed in Chapter 3, to reduce the contrast between abnormalities and the retinal background as well as to correct the non-uniform illumination in retinal images. Then the vesselness measure is used for vessel segmentation by finding the local maximum of the large eigenvalue and the standard deviation of vessel orientations over scales, as in Equation 5.17.

In the experiments conducted, the maximum over scales were calculated up to scale 4, which was chosen after some exploratory experiments (different values for the scale s are used). Table 5.1 shows the effect of changing the scale value s on the sensitivity at certain specificity values. It is clear that sensitivity values increased with the increase in s, till reaching its maximum value, then a decrease in the sensitivity is occurred. The best performance was obtained where the maximum sensitivity was achieved, i.e. at $s = 4$. This value for s is then used in the experiments carried out in the chapter.

From ROC curves, sensitivity at certain specificity values was used to compare the proposed algorithm and other methods in the literature. Also the A_z (area under the ROC curve) is used as a single measure for performance.

Table 5.1: Results from exploratory experiments (for one image)

Specificity	Sensitivity					
	$s = 2$	$s = 3$	$s = 4$	$s = 5$	$s = 6$	$s = 7$
95%	73.67%	78.13%	**78.26%**	76.49%	74.31%	72.16%
90%	80.55%	85.32%	**86.23%**	85.55%	84.32%	82.89%
85%	84.29%	88.81%	**89.98%**	89.66%	89.01%	88.11%
80%	87.01%	91.13%	**92.19%**	92.14%	91.63%	91.01%

Table 5.2: Results for vesselness measure (averaged over 20 images)

Image	Specificity	Sensitivity
Normal	95%	87.43%
Abnormal		77.31%
All images		**82.37%**
Normal	90%	92.69%
Abnormal		85.90%
All images		**89.29%**
Normal	85%	94.89%
Abnormal		90.11%
All images		**92.50%**
Normal	80%	96.18%
Abnormal		92.88%
All images		**94.53%**

Figure 5.7 shows two images with their results using the piecewise threshold probing method [12] and the vesselness measure. ROC curves are also plotted for these two methods in Figure 5.8. For the normal image, the improvement is from FPR > 0.05, while for the abnormal image, improvement starts at very low values of FPR. This can be explained as a result of the pre-processing step, where the responses corresponding to abnormalities around the fovea have lower contrast in the HMI.

On average, when using 20 images from the STARE dataset, at specificity of 95%, a sensitivity of 87.43% and 77.31% are achieved for normal and abnormal images respectively. These sensitivity values increased to 92.69% and 85.90% respectively at specificity of 90%. Table 5.2 summarises results obtained when using the vesselness measure.

For purposes of comparison, the TPR are calculated at FPR of 4.4% for all images, to compare with [12, 46, 63]. The algorithm in [63] is implemented and images of the Hoover *et al.* method [12] are used to find these TPR. Results for Jiang *et al.* were reported in

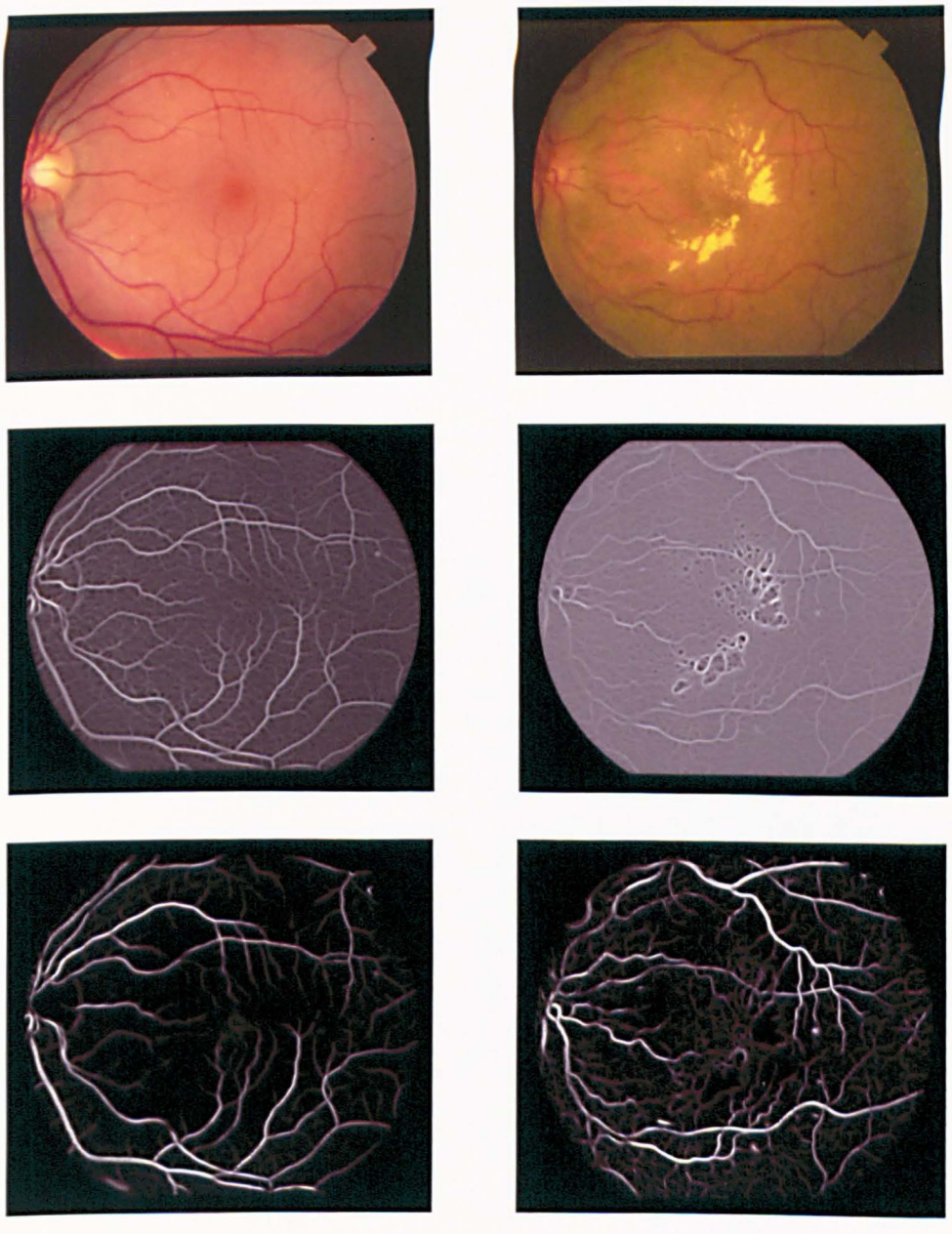

Figure 5.7: (a) RGB images, (b) Hoover method, and (c) vesselness measure for normal (left) and abnormal (right) images.

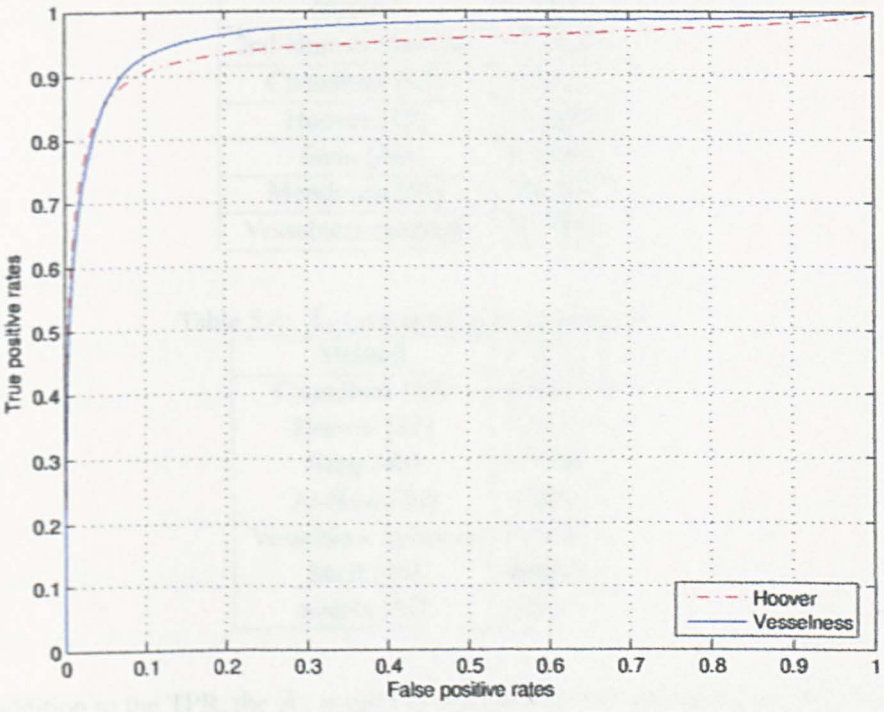

(a)

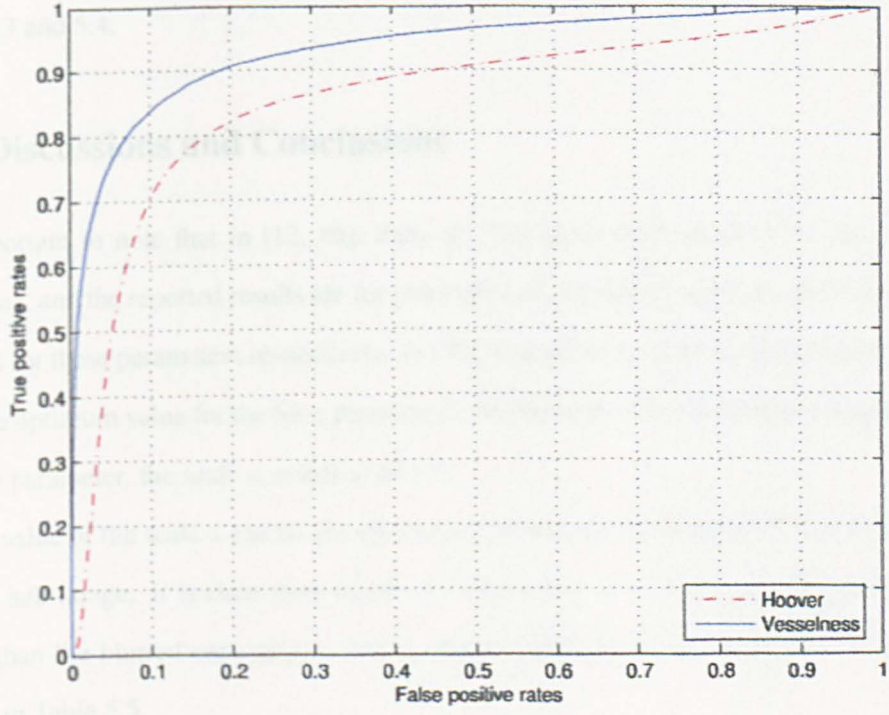

(b)

Figure 5.8: ROC curves for (a) normal, and (b) abnormal images in Figure 5.7.

Table 5.3: TPR at 4.4% FPR (averaged over 20 images, No mask)

Method	TPR
2nd Human observer	89.50%
Chaudhuri [63]	55.01%
Hoover [12]	75.48%
Jiang [46]	83.50%
Mendonca [51]	**84.2%**
Vesselness measure	80.93%

Table 5.4: A_z (averaged over 20 images)

Method	A_z
Chaudhuri [63]	0.8987
Hoover [12]	0.9112
Jiang [46]	0.9298
Al-Rawi[50]	0.9090
Vesselness measure	0.9450
Staal [44]	**0.9671**
Soares [52]	0.9614

[46]. In addition to the TPR, the A_z is used to compare results obtained from the proposed method and those reported by [12, 44, 46, 50, 52, 63]. These results are summarised in Tables 5.3 and 5.4.

5.5 Discussions and Conclusions

It is important to note that in [12, 46], there are five parameters required for these two algorithms, and the reported results are for processing all 20 images using *ten* and *eight* sets of values for these parameters respectively. In [50], it depends on optimisation procedure to select the optimum value for the filter parameters. Significantly, for the proposed algorithm, only *one* parameter, the scale s, needs to be set.

The value of the scale s can be chosen when considering the diameter of blood vessels within a sub-image. It is clear from Figure 5.2 that values $s = 3 \text{ or } 4$ give more realistic vessels than the blurred ones at $s = 5 \text{ or } 6$. Results using different values of s are summarised in Table 5.5.

Table 5.5: Sensitivity at 95% specificity and the A_z using different scale value (averaged from 20 images)

scale	sensitivity	A_z
3	81.76%	0.9395
4	**82.37%**	**0.9450**
5	81.32%	0.9439
6	79.62%	0.9407

Results from [44, 52] are better than results obtained using the proposed method as these are supervised methods which has some advantages over the unsupervised ones, as higher performance. On the other hand, the need for GT (manually segmented images) in order to extract training set and the necessity of a good feature vector in order to classify image pixels to their corresponding classes presents some drawbacks. There is no doubt that the performance of the classifier is affected by the choice of the feature vector and the training set. Moreover, in this application, where retinal blood vessel segmentation is the main task, generating a training set is not an easy job to do. First, there are 423,500 pixels/image with more than 25% dark background pixels and the dataset consists of 20 images some of them of bad quality (very bright or saturated images). Second, the property of multiple object classes of varying colour/reflectance [46] and - sometimes - there is a similarity between feature vectors for vessel and non-vessel pixels from different images.

A novel unsupervised method for retinal blood vessel segmentation is proposed. This method is based on a proposed vesselness measure, which depends on vessel centrelines and orientations. One of the main advantages of the proposed method, is that it is completely unsupervised, so there is no need for manually labelled images - segmented by a human observer - which is time consuming and subject to observer bias. Another major advantage is that a minimum number of parameters are used (only one parameter is needed), in addition to its simplicity and easy implementation.

Ongoing work will use results from the vesselness measure in conjunction with classifiers or semi-supervised clustering algorithms. This is by generating a binary image to be used instead of the manually segmented images to train a classifier or as labelled samples for a semi-supervised clustering.

Chapter 6

Conclusions and Future Work

6.1 Summary and Conclusions

AUTOMATED segmentation of retinal blood vessels is important for vessel measurements also it is a prerequisite in many other applications including localisation of other anatomical structures and abnormality detection. This research is motivated by the challenging problem of blood vessel segmentation from colour fundus images. In this context, a pre-processing step has been proposed and different segmentation methods have been investigated.

Chapter 3 presented a pre-processing step that utilises the intensity information from the red channel of colour fundus images. Inspection of the three colour channels of the retinal image shows that the red channel is brighter than the green one. Therefore, the red channel is used to segment the retinal FOV, i.e. to generate a binary mask. Differences between standard deviation values for regions contain successive rows (columns) are calculated. The maximum value of these differences is located at the row (column) from where the retinal FOV starts or ends. A rectangle that surrounds the FOV is formed by rows and columns that define start and end points of the FOV. Pixels outside this rectangle are used as seeds for a region growing step.

Additionally, a novel enhancement method for colour retinal images has been developed by combining intensity information from red and green channels. Histogram match-

ing has been used to modify the histogram of the green channel using the histogram of the red channel of the same retinal image which is different from the previously proposed applications of histogram matching in the literature. This step results in enhancement of the visual appearance of the retinal image, decreasing the contrast between bright abnormalities and the retinal background in abnormal cases, also correcting the non-uniform illumination in many normal cases. An important observation that should be mentioned about the pre-processing step is that it is not applicable for all retinal images. For example, in case of very bright images, combining red and green channels will result in a HMI with much lower contrast than the green channel alone. To detect these cases, a saturation condition criterion was proposed to define the very bright red channels and therefore use the green channel image without modifying its histogram.

Chapter 4 has explored different methods - supervised, unsupervised, and semi-supervised methods - to segment retinal blood vessels from colour fundus images. In this chapter, a feature vector was first extracted for each pixel in the retinal image based on three main characteristics of the blood vessel - darker than the background, piecewise linear, and has parallel edges. These features are the large eigenvalue and the gradient magnitude extracted at multiple scales in addition to the green channel image.

The *KNN* classifier has been used to classify image pixels into vessel and non-vessel pixels taking into account these three features for each image pixels. Significant reduction in the processing time is the major outcome of the use of this feature vector compared with another feature vector of 31 features proposed by Niemeijer *et al.* [73] with comparable classification results.

Instead of using a feature vector with a supervised method, it has been used with an unsupervised one, where supervised and unsupervised concepts were combined in the *NNCA*, in which pixels are clustered based on this feature vector without generating a training set or using a labelled samples. Experimental results show that the *NNCA* gives 5% lower performance than the *KNN* classifier, however this is a result of it being unsupervised.

In cases where the GT image is not completely available, semi-supervised methods, such as *RACAL* with partial supervision appears to be the best possible solution. The

RACAL have been used as a classifier to classify image pixels as vessel and non-vessel pixels. In the supervision strategy, a percentage of the GT pixels are used as labelled samples. In normal cases, *RACAL* gives comparable results with the *KNN* classifier. Additionally, for the abnormal images, results were better than the *KNN* classifier. An interesting observation about partial supervised methods, is that it give comparable results with the *KNN* classifier.

Chapter 5 has introduced a novel unsupervised method for vessels segmentation, which utilises vessel centreline and orientation variations at multiple scales. Blood vessel centrelines are detected as the local maximum of large eigenvalues of the Hessian matrix at different scales. While variation in orientations is calculated from the standard deviation between angles of the eigenvectors at different scales. Completely unsupervised nature and use of a single parameter, its simplicity and easy implementation are advantages which make this method preferable over other segmentation methods.

In conclusion, this thesis has provided an extensive study of retinal vessel segmentation methods and has proposed novel ways towards the automatic segmentation of retinal blood vessels from colour fundus images. This research aims to provide a reliable method for blood vessel segmentation, and hopefully the findings of this work contribute a step forward towards the automatic detection and diagnosis of ocular diseases.

6.2 The Road Ahead

This thesis is mainly concerned with blood vessel segmentation from colour fundus images. Based on the work proposed in this research, further investigations are suggested in this section.

A quality assessment step could be introduced to decide the suitability of a retinal image for automatic processing in order to solve problems associated with poor quality images.

The work done on the vesselness measure could be extended by introducing a scheme to select candidate pixels in order to get a binary image (Generated Ground Truth (GGT) image). This GGT image would be of great importance and could be used to provide la-

belled objects for supervised methods or to overcome the initialisation problem in tracking methods. The initial points for a tracking algorithm can be selected from the GGT image. In this case, pixels from the GGT image are stored in a queue, and each pixel in the queue acts as a starting point to trace part of the vessel network. In case of semi-supervised methods such as in the *RACAL* algorithm which has been proposed as a classifier, this GGT could be used to provide initial prototypes for the clustering step, or considered as the labelled objects, instead of selecting random pixels from the GT images, to classify the non-overlapped clusters into their corresponding classes.

On the image analysis side, skeletons from the GGT image could be used to detect and measure many important features of the vascular network. One of these measurements is the vessel tortuosity, which is the result of accumulation of curvature along blood vessel length. Branching angles are another feature, which could indicate the presence of hypertension. Also blood vessel width can be measured by using these skeletons along with the eigenvectors (corresponding to the large eigenvalues).

One way to reduce the false positives is the detection of retinal abnormalities such as microaneurysms, hemorrhages, exudates and cotton-wool spots. Other avenues for possible extension of this work is the analysis of the blood vessel network in order to get more information which will be valuable in detection and diagnosis of many ocular diseases.

Appendix A

ROC Curves

A.1 Efficient Generation of ROC Curves

Given a gray scale image of size $n \times m$ and it is required to generate an ROC curve, a straight forward algorithm will start by setting threshold values. For each threshold value obtain the binary image, then calculate the FPR and TPR which represent a single point on the ROC curve. This algorithm is not practical as the threshold values need to be set based on the maximum and minimum intensities in the image and the required increment value.

In [61], Tom Fawcett proposed an efficient algorithm based on the monotonicity of thresholded classifications, where any pixel that is classified positive with respect to a given threshold will be classified positive for all higher thresholds as well. Therefore, this algorithm simply sorts image pixels in descending order, moves down the list, processes one pixel at a time, and updates TP and FP as moving down the list. In this way, an ROC graph can be created from a linear scan.

A.2 Area Under an ROC Curve

The area under an ROC curve (A_z) is used as a single scalar value to represent the performance of a classifier. As the perfect classification results produces a point at the top left corner which gives $A_z = 1$, while the random classifier produces a straight line ($x = y$),

the area under this line $\bar{A}_z = 0.5$. This implies that $\bar{A}_z$ values should be between 0.5 and 1. The $\bar{A}_z$ has an important statistical property: the $\bar{A}_z$ of a classier is equivalent to the probability that the classifier assigns a higher rank to a randomly chosen positive sample than that assigned to a randomly chosen negative samples which is equivalent to the Wilcoxon test of ranks [93].

To calculate the $\bar{A}_z$, a method which based on constructing trapezoids under the curve as an approximation of area is used. The area of a trapezoid can be computed as the length of the mid-segment, multiplied by the distance along a perpendicular line between the parallel sides. If a and b are the two parallel sides and h is the distance (height) between the two parallel sides, the area of a trapezoid $= (\frac{a+b}{2})h$, the $\bar{A}_z$ is the summation of successive areas of trapezoids that approximated the ROC curve.

Appendix B

Image Derivatives

For a given intensity image, $I(x, y)$, the observed image, $L(x, y)$, is defined as the convolution of the outside world image with the aperture function. It is obtained by convolution with the Gaussian kernel:

$$L(x, y) = I(x, y) \otimes G(x, y)$$

To take derivatives of the observed image, taking into account the linearity of the differential and the convolution operators, these two operators can be commuted. Therefore image derivatives can be taken by convolving the intensity image with derivatives of the Gaussian kernel as:

$$\frac{\delta}{\delta x} L(x, y) = \frac{\delta}{\delta x}(I(x, y) \otimes G(x, y)) = I(x, y) \otimes \frac{\delta}{\delta x} G(x, y)$$

The Gaussian kernel is considered as the unique scale-space operator to change the scale [94]. Then, to represent image information at different scales, the convolution is then performed using a Gaussian kernel, $G(x, y; s)$, of variance s^2:

$$L(x, y; s) = I(x, y) \otimes G(x, y; s)$$

where s is the scale factor and $G(x, y; s)$ is:

$$G(x, y; s) = \frac{1}{2\pi s^2} e^{-\frac{x^2+y^2}{2s^2}}$$

Image derivatives are computed by convolution with derivatives of the Gaussian kernel as:

$$\frac{\delta}{\delta x}L(x,y;s) = I(x,y) \otimes \frac{\delta}{\delta x}G(x,y;s)$$

The scale-normalised Gaussian derivative operators are used in order to make all measurements relative to the scale. In this context, let

$$\tilde{x} \longmapsto \frac{x}{s}$$

the Gaussian derivatives will be:

$$\frac{\delta^n G}{\delta \tilde{x}^n} = s^n \frac{\delta G}{\delta x^n}$$

First and second derivatives of the intensity image in the $x-$ and $y-$ directions can be expressed as:

$$L_x = I(x,\, y) \otimes\, sG_x$$

$$L_y = I(x,\, y) \otimes\, sG_y$$

$$L_{xx} = I(x,\, y) \otimes\, s^2 G_{xx}$$

$$L_{xy} = I(x,\, y) \otimes\, s^2 G_{xy}$$

$$L_{yy} = I(x,\, y) \otimes\, s^2 G_{yy}$$

Mixed and higher order derivatives are computed by taking mixed and higher order derivatives of the Gaussian kernel.

Appendix C

Eigenvalue Analysis of the Hessian Matrix

C.1 Linear Algebra

Hessian matrix, the matrix of the second order derivative of the intensity image, is expressed as:

$$H = \begin{pmatrix} L_{xx} & L_{xy} \\ L_{yx} & L_{yy} \end{pmatrix}$$

where $L_{xy} = L_{yx}$ which implies that the Hessian matrix is symmetrical with real eigenvalues and orthogonal eigenvectors. λ_1 is an eigenvalue of H if there is a non-zero vector ν_1 such that: $H\nu_1 = \lambda_1\nu_1$ (where ν_1 is the eigenvector corresponding to λ_1). To find eigenvalues and their corresponding eigenvectors, let us start with

$$H\nu = \lambda\nu$$

$$H\nu = \lambda I\nu$$

$$H\nu - \lambda I\nu = 0$$

$$(H - \lambda I)\nu = 0$$

To solve this Equation:

- if $(H - \lambda I)$ is invertible;

  then the only solution will be $\nu = (H - \lambda I)^{-1}0 = 0$ which is not accepted,

- if $(H - \lambda I)$ is not invertible;

  then $det(H - \lambda I) = 0$ is the solution to find the eigenvalues of H.

C.2 Eigenvalues

To find eigenvalues of the Hessian matrix:

$$|H - \lambda I| = 0$$

$$\begin{vmatrix} L_{xx} - \lambda & L_{xy} \\ L_{xy} & L_{yy} - \lambda \end{vmatrix} = L_{xx}L_{yy} - L_{xx}\lambda - L_{yy}\lambda + \lambda^2 - L_{xy}^2$$

$$\lambda^2 - (L_{xx} + L_{yy})\lambda + (L_{xx}L_{yy} - L_{xy}^2) = 0$$

$$\lambda = \tfrac{1}{2}\left((L_{xx} + L_{yy}) \pm \sqrt{(L_{xx} + L_{yy})^2 - 4L_{xx}L_{yy} + 4L_{xy}^2}\right)$$

$$\lambda = \tfrac{1}{2}\left((L_{xx} + L_{yy}) \pm \sqrt{(L_{xx} - L_{yy})^2 + 4L_{xy}^2}\right)$$

Then, eigenvalues of the Hessian matrix are:

$$\lambda_+ = \frac{L_{xx} + L_{yy} + \alpha}{2} \tag{C.2.1}$$

$$\lambda_- = \frac{L_{xx} + L_{yy} - \alpha}{2} \tag{C.2.2}$$

where $\alpha = \sqrt{(L_{xx} - L_{yy})^2 + 4L_{xy}^2}$

C.3 Eigenvectors

To find eigenvectors corresponding to λ_+ and λ_-:

$Hv = \lambda v$

at $\lambda = \lambda_+$, this can be written as: $Hv_+ = \lambda_+ v_+$

$$\begin{pmatrix} L_{xx} & L_{xy} \\ L_{xy} & L_{yy} \end{pmatrix} \begin{pmatrix} x \\ y \end{pmatrix} = \lambda_+ \begin{pmatrix} x \\ y \end{pmatrix}$$

$L_{xx}x + L_{xy}y = \frac{L_{xx}+L_{yy}+\alpha}{2}x$

$2L_{xx}x + 2L_{xy}y = L_{xx}x + L_{yy}x + \alpha x$

$(L_{xx} - L_{yy} - \alpha)x + 2L_{xy}y = 0$

Let $x = k$, then $y = \frac{-L_{xx}+L_{yy}+\alpha}{2L_{xy}}k$

$$v_+ = \begin{pmatrix} k \\ \frac{-L_{xx}+L_{yy}+\alpha}{2L_{xy}}k \end{pmatrix} \tag{C.3.3}$$

similarly for v_-:

$$v_- = \begin{pmatrix} \frac{-L_{xx}+L_{yy}+\alpha}{-2L_{xy}}k \\ k \end{pmatrix} \tag{C.3.4}$$

To make the eigenvectors of unit length, are normalised as follows:

$v_{+norm} = \begin{pmatrix} \frac{1}{a}k \\ \frac{1}{a}\left(\frac{-L_{xx}+L_{yy}+\alpha}{2}k\right) \end{pmatrix}$ where $a = \sqrt{k^2 + \left(\frac{-L_{xx}+L_{yy}+\alpha}{2L_{xy}}k\right)^2}$

a can be simplified as: $a = \frac{k}{2L_{xy}}\sqrt{(2L_{xy})^2 + (-L_{xx} + L_{yy} + \alpha)^2} = \frac{Nk}{2L_{xy}}$

Then, the normalised eigenvector corresponding to λ_+:

$$v_{+norm} = \frac{1}{N}\begin{pmatrix} 2L_{xy} \\ -L_{xx} + L_{yy} + \alpha \end{pmatrix} \tag{C.3.5}$$

similarly for v_{-norm}, the normalised eigenvector corresponding to λ_-:

$$\nu_{-norm} = \frac{1}{N} \begin{pmatrix} -L_{xx} + L_{yy} + \alpha \\ -2L_{xy} \end{pmatrix} \tag{C.3.6}$$

where $N = \sqrt{(-L_{xx} + L_{yy} + \alpha)^2 + 4L_{xy}^2}$

Bibliography

[1] J. J. Kanski, *Clinical Ophthalmology: A Systematic Approach.* London, U.K.: Butterworth-Heinemann, 1989.

[2] C. Sinthanayothin, J. F. Boyee, T. H. Williamson, H. L. Cook, E. Mensah, S. Lal, and D. Usher, "Automated detection of diabetic retinopathy on digital fundus images," *Diabetic Medicine*, vol. 19, pp. 105–112, February 2002.

[3] C. Heneghan, J. Flynn, M. O'Keefe, and M. Cahill, "Characterization of changes in blood vessel width and tortuosity in retinopathy of prematurity using image analysis," *Medical Image Analysis*, vol. 6, pp. 407–429, December 2002.

[4] F. Zana and J. Klein, "A multimodal registration algorithm of eye fundus images using vessel detection and Hough transform," *IEEE Transactions on Medical Imaging*, vol. 18, pp. 419–428, May 1999.

[5] A. Can, C. V. Stewart, B. Roysam, and H. L. Tanenbaum, "A feature-based, robust, hierarchical algorithm for registering pairs of images of the curved human retina," *IEEE Transactions on Pattern Analysis and Machine Intelligent*, vol. 24, pp. 347–364, March 2002.

[6] A. Pinz, S. Bernögger, P. Daltinger, and A. Kruger, "Mapping the human retina," *IEEE Transactions on Medical Imaging*, vol. 17, pp. 606–619, August 1998.

[7] A. Hoover and M. Goldbaum, "Locating the optic nerve in a retinal image using fuzzy convergence of the blood vessels," *IEEE Transactions on Medical Imaging*, vol. 22, pp. 951–958, August 2003.

[8] M. Foracchia, E. Grisan, and A. Ruggeri, "Detection of optic disc in retinal images by means of a geometrical model of vessel structure," *IEEE Transactions on Medical Imaging*, vol. 23, pp. 1189–1195, October 2004.

[9] H. Li and O. Chutatape, "Automated feature extraction in color retinal images by model based approach," *IEEE Transactions on Biomedical Engineering*, vol. 51, pp. 246–254, February 2004.

[10] T. Saude, *Ocular Anatomy and Physiology*. Oxford ; Boston: Blackwell Scientific Publications, 1993.

[11] R. S. Snell and M. A. Lemp, *Clinical Anatomy of The Eye*. Boston: Blackwell Scientific Publications, 1989.

[12] A. Hoover, V. Kouznetsova, and M. Goldbaum, "Locating blood vessels in retinal images by piece-wise threshold probing of a matched filter response," *IEEE Transactions on Medical Imaging*, vol. 19, pp. 203–210, March 2000.

[13] M. Goldbaum, S. Moezzi, A. Taylor, S. Chatterjee, J. Boyd, E. Hunter, and R. Jain, "Automated diagnosis and image understanding with object extraction, object classification, and inferencing in retinal images," *IEEE International Conference on Image Processing*, vol. 3, pp. 695–698, September 1996.

[14] G. Wise, C. Dollery, and P. Henkind, *The Retinal Circulation*. New York: Harper & Row Medical Department, 1st ed., 1971.

[15] H. R. Taylor and J. E. Keeffe, "World blindness: a 21st century perspective," *British Journal of Ophthalmology*, vol. 85, pp. 261–266, March 2001.

[16] J. E. Shaw, P. Z. Zimmet, D. McCarty, and M. de Courten, "Type 2 diabetes worldwide according to the new classification and criteria," *Diabetes Care*, vol. 23, pp. B5–10, April 2000.

[17] ETDRS Research Group, "Early photocoagulation for diabetic retinopathy: Etdrs report 9," *Ophthalmology*, vol. 98, pp. 766–785, May 1991.

[18] G. Bresnick, D. Mukamel, J. Dickinson, and D. Cole, "A screening approach to the surveillance of patients with diabetes for the presence of vision-threatening retinopathy," *Opthalmology*, vol. 107, pp. 19–24, January 2000.

[19] J. Evans, C. Rooney, F. Ashwood, N. Dattani, and R. Wormald, "Blindness and partial sight in England and Wales: April 1990-March 1991," *Health Trends*, vol. 28, pp. 5–12, 1996.

[20] D. Maberley, H. Walker, A. Koushik, and A. Cruess, "Screening for diabetic retinopathy in James Bay, Ontario: a cost effectiveness analysis," *Canadian Medical Association Journal*, vol. 168, pp. 160–164, January 2003.

[21] F. L. Ferris, "How effective are treatments for diabetic retinopathy?," *The Journal of the American Medical Association*, vol. 269, pp. 1290–1291, March 1993.

[22] A. D. Fleming, S. Philip, K. A. Goatman, J. A. Olson, and P. F. Sharp, "Automated assessment of diabetic retinal image quality based on clarity and field definition," *Investigative Ophthalmology and Visual Science*, vol. 47, pp. 1120–1125, March 2006.

[23] M. Niemeijer, M. D. Abràmoff, and B. van Ginneken, "Image structure clustering for image quality verification of color retina images in diabetic retinopathy screening," *Medical Image Analysis*, vol. 10, pp. 888–898, December 2006.

[24] D. Usher, M. Dumskyj, M. Himaga, T. H. Williamson, S. Nussey, and J. Boyce, "Automated detection of diabetic retinopathy in digital retinal images: a tool for diabetic retinopathy screening," *Diabetic Medicine*, vol. 21, pp. 84–90, January 2004.

[25] A. D. Fleming, K. A. Goatman, S. Philip, J. A. Olson, and P. F. Sharp, "Automatic detection of retinal anatomy to assist diabetic retinopathy screening," *Physics in Medicine and Biology*, vol. 52, pp. 331–345, January 2007.

[26] M. Niemeijer, M. D. Abràmoff, and B. van Ginneken, "Segmentation of the optic disc, macula and vascular arch in fundus photographs," *IEEE Transactions on Medical Imaging*, vol. 26, pp. 116–127, January 2007.

[27] A. Osareh, M. Mirmehdi, B. Thomas, and R. Mrkham, "Automated identification of diabetic retinal exudates in digital colour images," *British Journal of Ophthalmology*, vol. 87, pp. 1220–1223, October 2003.

[28] T. Walter, J. Klein, P. Massin, and A. Erginay, "A contribution of image processing to the diagnosis of diabetic retinopathy - detection of exudates in colour fundus images of the human retina," *IEEE Transactions on Medical Imaging*, vol. 21, pp. 263–269, October 2002.

[29] A. Osareh, *Automated Identification of Diabetic Retinal Exudates and the Optic Disc*. PhD thesis, Department of Computer Science, University of Bristol, January 2004.

[30] J. H. Hipwell, F. Strachan, J. A. Olson, K. C. McHardy, P. F. Sharp, and J. V. Forrester, "Automated detection of microaneurysms in digital red-free photographs: a diabetic retinopathy screening tool," *Diabetic Medicine*, vol. 17, pp. 588–594, August 2000.

[31] M. Niemeijer, B. van Ginneken, J. Staal, M. Suttorp-Schulten, and M. D. Abràmoff, "Automatic detection of red lesions in digital color fundus photographs," *IEEE Transactions on Medical Imaging*, vol. 24, pp. 584–592, May 2005.

[32] M. Shahidi, N. P. Blair, M. Mori, J. Gieser, and J. S. Pulido, "Retinal topography and thickness mapping in atrophic age related macular degeneration," *British Journal of Ophthalmology*, vol. 86, pp. 623–626, June 2002.

[33] R. T. Smith, T. Nagasaki, J. R. Sparrow, I. Barbazetto, C. C. Klaver, and J. K. Chan1, "A method of drusen measurement based on the geometry of fundus reflectance," *BioMedical Engineering OnLine*, vol. 2, April 2003.

[34] A. Mora, J. Fonseca, and P. Vieira, "Drusen deposits modelling with illumination correction," in *the IASTED International Conference Biomedical Engineering*, (Innsbruck, Austria), 16–18 February 2005.

[35] L. A. King, A. V. Stanton, P. S. Sever, S. A. Thom, and A. D. Hughes, "Arteriolar length-diameter (l:d) ratio: a geometric parameter of the retinal vasculature diagnostic of hypertension," *Journal of Human Hypertension*, vol. 10, pp. 417–418, June 1996.

[36] H. Pakter, E. Ferlin, S. Fuchs, M. Maestri, R. Moraes, G. Nunes, L. Moreira, M. Gus, and F. Fuchs, "Measuring arteriolar-to-venous ratio in retinal photography of patients with hypertension: Development and application of a new semi-automated method," *American Journal of Hypertension*, vol. 18, pp. 417–421, March 2005.

[37] M. E. Martínez-Pérez, *Computer Analysis of the Geometry of the Retinal Vasculature*. PhD thesis, London: Imperial College of Science, Technology and Medicine, November 2000.

[38] X. Wang, H. Cao, and J. Zhang, "Analysis of retinal images associated with hypertension and diabetes," in *the 27th Annual International Conference of the IEEE Engineering in Medicine and Biology Society*, pp. 6407–6410, 1-4 September 2005.

[39] P. Zhou, M. Wang, and H. Cao, "Research on features of retinal images associated with hypertension and diabetes," in *the 27th Annual International Conference of the IEEE Engineering in Medicine and Biology Society*, pp. 6415–6417, 1-4 September 2005.

[40] Y. Hatanaka, Y. Hayashi, T. Nakagawa, A. Aoyama, X. Zhou, T. Hara, H. Fujita, Y.Mizukusa, A. Fujita, and M. Kakogawa, "Development of computer-aided diagnosis system for fundus images," in *the 8th International Conference on Medical Image Computing and Computer Assisted Intervention- MICCAI' 05*, (Palm Springs, California, USA), 26-30 October 2005.

[41] J. Yu, S. Abidi, P. Artes, A. McIntyre, and M. Heywood, "Diagnostic support for glaucoma using retinal images: a hybrid image analysis and data mining approach," in *Studies in Health Technology and Informatics* (R. Engelbrecht, A. Geissbuhler, C. Lovis, and G. Mihalas, eds.), vol. 116, pp. 187–192, 2005.

[42] "The STARE project." Available at http://www.ces.clemson.edu/~ahoover/stare.

[43] "The DRIVE database." Available at http://www.isi.uu.nl.Research/Databases/DRIVE.

[44] J. Staal, M. D. Abràmoff, M. Niemeijer, M. A. Viergever, and B. van Ginneken, "Ridge-based vessel segmentation in color images of the retina," *IEEE Transactions on Medical Imaging*, vol. 23, pp. 501–509, April 2004.

[45] R. C. Gonzalez and R. E. Woods, *Digital Image Processing*. Upper Saddle River, New Jersy: Prentice-Hall, 2002.

[46] X. Jiang and D. Mojon, "Adaptive local thresholding by verification-based multithreshold probing with application to vessel detection in retinal images," *IEEE Transactions on Pattern Analysis and Machine Intelligent*, vol. 25, pp. 131–137, January 2003.

[47] W. C. Cai and A. C. Chung, "Multi-resolution vessel segmentation using normalized cuts in retinal images," in *Lecture Notes in Computer Science 4191:928-936, 2006.*, vol. 4191, pp. 928–936, 2006.

[48] S. Garg, J. Sivaswamy, and S. Chandra, "Unsupervised curvature-based retinal vessel segmentation.," in *4th IEEE International Symposium on Biomedical Imaging: From Nano to Macro*, pp. 344–347, 12-15 April 2007.

[49] C. Wu, G. Agam, and P. Stanchev, "A hybrid filtering approach to retinal vessel segmentation," in *IEEE Internation Symposium On Biomedical Imaging: From Nano to Macro*, (Metro Washington DC, USA), 12-15 April 2007.

[50] M. Al-Rawi, M. Qutaishat, and M. Arrar, "An improved matched filter for blood vessel detection of digital retinal images," *Computers in Biology and Medicine*, vol. 37, pp. 262–267, February 2007.

[51] A. M. Mendonça and A. Campilho, "Segmentation of retinal blood vessels by combining the detection of centerlines and morphological reconstruction," *IEEE Transactions on Medical Imaging*, vol. 25, pp. 1200–1213, September 2006.

[52] J. V. B. Soares, J. J. G. Leandro, R. M. Cesar-Jr., H. F. Jelinek, and M. J. Cree, "Retinal vessel segmentation using the 2-D Gabor wavelet and supervised classification," *IEEE Transactions on Medical Imaging*, vol. 25, pp. 1214–1222, September 2006.

[53] M. Sofka and C. V. Stewart, "Retinal vessel extraction using multiscale matched filters, confidence and edge measures," *IEEE Transactions on Medical Imaging*, vol. 25, pp. 1531–1546, December 2006.

[54] D. Wu, M. Zhang, J. Liu, and W. Bauman, "On the adaptive detection of blood vessels in retinal images," *IEEE Transactions on Biomedical Engineering*, vol. 53, pp. 341–343, February 2006.

[55] M. Park, S. S. Jin, and S. Luo, "Locating the optic disc in retinal images," in *International Conference on Computer Graphics, Imaging and Visualisation*, pp. 141 – 145, 26-28 July 2006.

[56] K. Huang and M. Yan, "A region based algorithm for vessel detection in retinal images," in *Lecture Notes in Computer Science*, vol. 4190, pp. 645–653, 2006.

[57] A. Ruggeri, M. Forrachia, and E. Grisan, "Detecting the optic disc in retinal images by means of a geometrical model of vessel network," in *the 25th Annual International Conference of the IEEE Engineering in Medicine and Biology Society*, vol. 1, pp. 902–905, 17-21 September 2003.

[58] L. Wang and A. Bhalerao, "Model based segmentation for retinal fundus images," in *Lecture Notes in Computer Science*, vol. 2749, pp. 289–325, 2003.

[59] L. Wang, A. Bhalerao, and R. Wilson, "Analysis of retinal vasculature using a multiresolution hermite model," *IEEE Transactions on Medical Imaging*, vol. 26, pp. 137–152, February 2007.

[60] C. E. Metz, "Basic principles of ROC analysis," *Seminars in Nuclear Medicine*, vol. 8, pp. 283–298, October 1978.

[61] T. Fawcett, "ROC graphs: notes and practical considerations for researchers," Tech. Rep. HPL-2003-4, HP Laboratories, March 2004.

[62] C. Kirbas and F. Quek, "A review of vessel extraction techniques and algorithms," *ACM Computing Surveys*, vol. 36, pp. 81–121, June 2004.

[63] S. Chaudhuri, S. Chatterjee, N. Katz, and M. Goldbaum, "Detection of blood vessels in retinal images using two-dimensional matched filters," *IEEE Transactions on Medical Imaging*, vol. 8, pp. 263–269, September 1989.

[64] W. E. Hart, M. Goldbaum, B. Côté, P. Kube, and M. R. Nelson, "Measurement and classification of retinal vascular tortuosity," *International Journal of Medical Informatics*, vol. 53, pp. 239–252, February 1999.

[65] L. Gang, O. Chutatape, and S. M. Krishnan, "Detection and measurement of retinal vessels in fundus images using amplitude modified second-order Gaussian filter," *IEEE Transactions on Biomedical Engineering*, vol. 49, pp. 168–172, February 2002.

[66] T. Chanwimaluang and G. Fan, "An efficient algorithm for extraction of anatomical structures in retinal images," in *IEEE International Conference on Image Processing*, pp. 1093–1096, September 2003.

[67] L. Zhou, M. S. Rzezotarski, L. J. Singerman, and J. M. Chokreff, "The detection and quantification of retinopathy using digital angiograms," *IEEE Transactions on Medical Imaging*, vol. 13, pp. 619–626, August 1994.

[68] O. Chutatape, L. Zheng, and S. M. Krishnan, "Retinal blood vessel detection and tracking by matched Gaussian and Kalman filters," in *the 20th Annual International Conference IEEE Engineering in Medicine and Biology*, pp. 3144–3149, 1998.

[69] Y. A. Tolias and S. M. Panas, "A fuzzy vessel tracking algorithm for retinal images based on fuzzy clustering," *IEEE Transactions on Medical Imaging*, vol. 17, pp. 263–273, April 1998.

[70] T. McInerney and D. Terzopoulos, "T-snakes: topolgy adaptive snakes," *Medical Image Analysis*, vol. 4, pp. 73–91, June 2000.

[71] T. Walter and J.-C. Klein, "Segmentation of color fundus images of the human retina: detection of the optic disc and the vascular tree using morphological techniques," in *Lecture Notes in Computer Science*, vol. 2199, pp. 282–287, Berlin: Springer-Verlag, 2001.

[72] F. Zana and J.-C. Klein, "Segmentation of vessel-like patterns using mathematical morphology and curvature evaluation," *IEEE Transactions on Image Processing*, vol. 10, pp. 1010–1019, July 2001.

[73] M. Niemeijer, J. Staal, B. van Ginneken, M. Long, and M. D. Abràmoff, "Comparative study of retinal vessel segmentation methods on a new publicly available database," in *SPIE Medical Imaging*, vol. 5370, pp. 648–656, May 2004.

[74] M. E. Martínez-Pérez, A. Hughes, A. Stanton, S. Thom, A. Bharath, and K. Parker, "Scale-space analysis for the characterisation of retinal blood vessels," in *Medical Image Computing and Computer-Assisted Intervention - MICCAI '99* (C. Taylor and A. Colchester, eds.), pp. 90–97, 1999.

[75] C. Sinthanayothin, J. F. Boyee, H. L. Cook, and T. H. Williamson, "Automated localisation of the optic disc, fovea, and retinal blood vessels from digital colour fundus images," *British Journal of Ophthalmology*, vol. 83, pp. 902–910, August 1999.

[76] S. A. Salem and A. K. Nandi, "Novel clustering algorithm (RACAL) and a partial supervision strategy for classification," in *IEEE International Workshop on Machine Learning for Signal Processing*, (Mynooth, Ireland), pp. 313–318, 6-8 September 2006.

[77] N. Patton, T. M. Aslam, T. MacGillivray, I. J. Deary, B. Dhillon, R. H. Eikelboom, K. Yogesan, and I. J. Constable, "Retinal image analysis: concepts, applications and potential," *Progress in Retinal and Eye Research*, vol. 25, pp. 99–127, January 2006.

[78] T. Morris and Z. Newell, "Enhancement and segmentation of retinal images," in *Time Frequency Time Scale '97, University of Coventry*, 1997.

[79] L. Gagnon, M. Lalonde, M. Boucher, and M.-C. Boucher, "Procedure to detect anatomical structures in optical fundus images," in *Conference Medical Imaging 2001: Image Processing (SPIE #4322)*, (San Diego), pp. 1218–1225, 19-22 February 2001.

[80] K. A. Goatman, A. D. Whitwam, A. Manivannan, J. A. Olson, and P. F. Sharp, "Colour normalisation of retinal images," in *Medical Image Understanding and Analysis*, pp. 49–52, 2003.

[81] M. Lalonde, L. Gagnon, and M. Boucher, "Automatic visual quality assessment in optical fundus images," in *Vision Interface '2001*, pp. 259–264, June 2001.

[82] A. Moore, "An assessment of retinal blood vessel segmentation using a MLP classifier and contextual post-processing," Master's thesis, King's College London, 2002.

[83] N. M. Salem and A. K. Nandi, "Novel and adaptive contribution of the red channel in pre-processing of colour fundus images," *Journal of the Franklin Institute, Special Issue: Medical Applications of Signal Processing, Part I*, vol. 344, pp. 243–256, May-July 2007.

[84] N. M. Salem and A. K. Nandi, "Segmentation of retinal blood vessels using scale-space features and K-nearest neighbour classifier," in *the 31st International Conference on Acoustics, Speech, and Signal processing - ICASSP '06*, (Toulouse, France), 14-16 May 2006.

[85] C. Lorenz, I.-C. Carlsen, T. M. Buzug, C. Fassnacht, and J. Weese, "Multi-scale line segmentation with automatic estimation of width, contrast and tangential direction

in 2D and 3D medical images," in *CVRMed-MRCAS '97, Lecture Notes in Computer Science* (J. Troccaz, E. Grimson, and R. Mösges, eds.), vol. 1205, pp. 233–242, Springer-Verlag, Berlin Heidelberg, 1997.

[86] A. F. Frangi, W. J. Niessen, K. L. Vincken, and M. A. Viergever, "Multiscale vessel enhancement filtering," in *Medical Image Computing and Computer-Assisted Intervention - MICCAI '98* (W. M. Wells, A. Colchester, and S. L. Delp, eds.), pp. 130–137, 1998.

[87] T. Lindeberg, *Scale-space Theory in Computer Vision.* Netherlands: Kluwer Academic publisher, 1994.

[88] L. F. Costa and R. M. Cesar-Jr, *Shape Analysis and Classification: Theory and Practice.* Boca Raton, FL: CRC, 2001.

[89] R. Duda, P. Hart, and D. Stork, *Pattern Classification.* New York: John Wiley and Sons, 2nd ed., 2001.

[90] S. A. Salem, N. M. Salem, and A. K. Nandi, "Segmentation of retinal blood vessels using a novel clustering algorithm," in *the 14th European Signal Processing Conference - EUSIPCO '06*, (Florence, Italy), 4-8 September 2006.

[91] S. A. Salem and A. K. Nandi, "Parallel nearest neighbour clustering algorithm (PNNCA) for segmenting retinal blood vessels," in *the 25th IASTED International Multi-Conference: parallel and distributed computing and networks*, (Innsbruck, Austria), pp. 263–268, 2007.

[92] Y. Sato, S. Nakajima, N. Shiraga, H. Atsumi, S. Yoshida, T. Koller, G. Gerig, and R. Kikinis, "3D multi-scale line filter for segmentation and visualization of curvilinear structures in medical images," in *CVRMed-MRCAS '97, Lecture Notes in Computer Science* (J. Troccaz, E. Grimson, and R. Mösges, eds.), vol. 1205, pp. 213–222, Springer-Verlag, Berlin Heidelberg, 1997.

[93] J. A. Hanley and B. J. McNeil, "The meaning and use of the area under a receiver operating characteristic (ROC) curve," *Radiology*, vol. 143, pp. 29–36, April 1982.

[94] B. M. ter Haar Romeny, "Introduction to scale-space theory: Multiscale geometric image analysis," Tech. Rep. ICU-96-21, Utrecht University, the Netherlands, September 1996.